TUM School of Natural Sciences

Technische Universität München

Tricalbins maintain plasma membrane integrity by modulating endoplasmic reticulum membrane curvature at ER-PM contact sites

Javier Fernández Collado

Vollständiger Abdruck der von der TUM School of Natural Sciences der Technischen Universität München zur Erlangung des akademischen Grades eines

Doktors der Naturwissenschaften (Dr. rer. nat.)

genehmigten Dissertation.

Vorsitz: Prof. Dr. Matthias Feige

Prüfer*innen der Dissertation:

1. Hon.-Prof. Dr. Wolfgang Baumeister
2. Prof. Dr. Rubén Fernández-Busnadiego

Die Dissertation wurde am 06.03.2023 bei der Technischen Universität München eingereicht und durch die TUM School of Natural Sciences am 14.06.2023 angenommen.

Contents

List of Figures

1 Summary

Eukaryotic cells make use of different mechanisms to establish communication between organelles. One such mechanism is membrane contact sites (MCSs) at places of close proximity between organelles. The interorganellar distance at these contacts is usually maintained below 30 nm, which allows for direct communication and metabolite exchange between different organelles. These microenvironments serve different functions depending on the organelles involved, and the protein populations at the cleft are specific for each contact.

MCSs between the cortical endoplasmic reticulum (cER) and the plasma membrane (PM) serve many important functions in the cell, and in *Saccharomyces cerevisiae* they account for almost half of the inner surface of the PM. The main tether proteins that form this type of contact in yeast have been previously identified as Tcb1/2/3, Scs2/22, and Ist2. Many of these proteins are highly conserved among eukaryotes, but their functions beyond membrane tethering have not yet been studied in depth.

Using cryo-electron tomography we characterize how these proteins affect cER morphology at the contact in vitrified, close-to-native conditions. In particular, we describe the presence of high curvature cER membrane peaks at the ER-PM interface in Tcb1/2/3 - expressing strains. Using flow cytometry, we correlate the absence of these peaks with a defect in PM repair in response to heat shock. Additionally, we assign Tcb3 an essential role in this process, in which it is likely assisted by Tcb1 or Tcb2.

We use mathematical modelling to propose a mechanism in which Tcb1/2/3 induce curvature in the cER as a way to reduce the energy barrier for lipid extraction. This would facilitate direct lipid transport to the PM by Tcb1/2/3 in conditions of fast and aggressive structural damage caused by heat shock. Taken together, these findings suggest a new role for cER-PM contact sites as checkpoints of PM integrity and regulators of local lipid homeostasis.

Zusammenfassung

Eukaryotische Zellen haben verschiedene Mechanismen entwickelt, um die Kommunikation zwischen Zellorganellen zu ermöglichen. Einer dieser Mechanismen sind Membrankontaktstellen, welche dort ausgebildet werden, wo Organellen nah beieinander liegen. Der Abstand dieser Kontakte zwischen den Organellen beträgt in der Regel unter 30 nm, was sowohl die direkte Kommunikation als auch den Austausch von Metaboliten zwischen unterschiedlichen Organellen ermöglicht. Diese Mirkoumgebungen haben, abhängig von den involvierten Organellen, verschiedene Funktionen. Außerdem sind die Proteinpopulationen im Spalt zwischen den Organellen spezifisch für die jeweilige Kontaktstelle.

Membrankontaktstellen zwischen dem kortikalen Endoplasmatischen Retikulum (kER) und er Plasmamembran (PM) erfüllen viele wichtige Funktionen in der Zelle und umfassen in *Saccharomyces cerevisiae* fast die Hälfte der inneren Oberfläche der Plasmamembran. Die wichtigsten Tetherproteine, die diese Art der Kontaktstellen in Hefen ausbilden, sind Tcb1/2/3, Scs2/22 und Ist2. Viele dieser Proteine sind innerhalb der Eukaryoten hochkonserviert, wobei ihre Funktionen abseits der Membranverankerung noch nicht im Detail beschrieben wurden.

Mittels Kryo-Elektronentomographie charakterisieren wir unter vitrifizierten, nahezu nativen Bedingungen wie diese Proteine die kER Morphologie an der Kontaktstelle beeinflussen. Vor allem beschreiben wir das Vorhandensein von stark gekrümmten kER Membranpeaks in Tcb1/2/3-exprimierenden Hefestämmen. Mit Hilfe von Durchflusszytometrie korrelieren wir die Abwesenheit dieser Membranpeaks mit einer defekten PM Reparatur nach Hitzeschock. Außerdem sprechen wir Tcb3 eine essenzielle Rolle in diesem Prozess zu, in welchem es vermutlich von Tcb1 oder Tcb2 unterstützt wird.

Basierend auf mathematischem Modelling schlagen wir einen Mechanismus vor, in dem Tcb1/2/3 die Krümmung im kER induzieren, um die für die Lipidextraktion benötigte Energiebarriere zu senken. Dies würde den durch Tcb1/2/3 ausgeübten direkten Lipidtransport zur Plasmamembran bei durch Hitzeschock verursachten schnellen und aggressiven strukturellen Schäden erleichtern. Insgesamt deuten unsere Ergebnisse darauf hin, dass kER-PM Kontaktstellen eine Rolle als Checkpoints der PM Integrität sowie als Regulatoren der lokalen Lipidhomöostase zukommt.

2 Introduction

2.1 Membrane Contact Sites

The compartmentalization of cellular processes in organelles is the defining feature of eukaryotic cells. The physical separation of the cellular space creates distinct microenvironments in which conditions are optimal for the enzymatic processes taking place in them. However, the partition of the cellular space makes it necessary to restore the communication between these processes by connecting the organelles that host them (Gatta and Levine 2017). The cell employs a vast array of mechanisms to ensure efficient molecular transport and signaling between organelles. One such mechanism is the network of membrane contact sites (MCSs) (Figure 1).

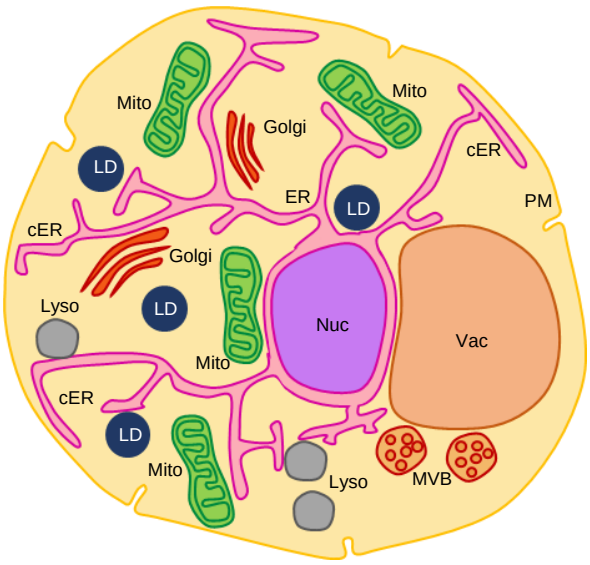

Figure 1 . Graphical MCS summary.

Simplified diagram of the MCS network in yeast. cER: cortical ER; Golgi: Golgi apparatus; PM: plasma membrane; Mito: mitochondrion; LD: lipid droplet; Vac: vacuole; Nuc: nucleus; Lyso: lysosome; MVB: Multivesicular body.

Found in all eukaryotes, MCSs are places of very close apposition (10~30 nm) between the membranes of two organelles (Levine and Loewen 2006; Lebiedzinska et al. 2009). The term *contact* is a misnomer inherited from the early days of the field, as the membranes involved do not fuse at any point. They are formed and maintained by dynamic tether proteins capable of bridging both membranes either directly or with the help of other proteins (Helle et al. 2013). The close proximity of the organelles creates a microenvironment at the MCS where certain proteins and/or lipids are enriched and where small molecules and lipids can be exchanged without the need of vesicular transport (Levine and Loewen 2006; Toulmay and Prinz 2012; Helle et al. 2013; Prinz 2014).

Direct transport is especially important for organelles like mitochondria or the plasma membrane (PM), which rely on MCSs with the endoplasmic reticulum (ER) to satisfy their need for certain lipids (Tatsuta et al. 2014; Lahiri et al. 2015). Mitochondria rely on MCSs with the ER for calcium homeostasis, and their lipid metabolism is particularly dependent on MCSs because they do not participate in the vesicular transport network. Defects in MCSs can often lead to disease when their function is compromised (Paillusson et al. 2016; Castro et al. 2018), and understanding their role in the cell and their components can provide valuable insights.

2.2 ER-PM MCSs

The part of the ER that forms contacts with the PM has received many names, but in this work it will be referred to as cortical endoplasmic reticulum (cER). It takes the form of a non-continuous meshwork of sheet-like cisternae and tubules that approach the PM at a distance ranging from 10 to 40 nm. These contacts were first described in muscle cells in 1957 (Porter and Palade 1957) and since then they have been found in every eukaryotic cell, from neurons to yeast.

The ER acts as one of the major Ca^{2+} reservoirs and ER-PM contacts are essential contributors to Ca^{2+} homeostasis. From an early evolutionary point, cells have needed to keep cytosolic calcium at lower concentrations than in the extracellular medium, which they accomplished by keeping Ca^{2+} out or in internal stores (Collins and Meyer 2011). As a consequence of these steep gradients, calcium became a common second messenger in a myriad of cellular processes, regulating cell proliferation and apoptosis and the responses of excitable cells.

Muscle excitation-contraction is a clear example of modulation by calcium at ER-PM MCSs. Ryanodine receptors on the sarcoplasmic reticulum (SC) release calcium from the SC lumen in response to cytosolic calcium, brought by interaction with PM-localized protein DHPR in the case of skeletal muscle and Ca^{2+} induced Ca^{2+} release in cardiac muscle. The increase in cytosolic calcium establishes a positive feedback loop that increases the release of SC calcium, triggering muscle contraction. Relaxation is achieved by pumping cytosolic calcium into the SR by Ca^{2+} ATPase SERCA (Lanner et al. 2010).

In metazoans, depletion of luminal ER calcium triggers the store operated calcium entry (SOCE), wherein ER-bound STIM proteins oligomerize and localize to the ER-PM contacts. There they interact with PM-embedded Orai calcium channels to allow the entry of extracellular calcium to replenish ER deposits (Carrasco and Meyer 2011). By regulating the intracellular calcium gradients ER-PM contacts play an important role in signal regulation (Giordano et al. 2013; Chang et al. 2017; Chung et al. 2017; Saheki and de Camilli 2017a).

Beyond Ca2+ signaling, ER-PM MCS are also important regulators of lipid homeostasis. The hundreds of different lipid species available to the cell serve a variety of functions, including as energy sources, structural components, and signaling molecules (Harayama and Riezman 2018; Casares et al. 2019).

The three main groups of biolipids are sterols, glycerophospholipids (GPLs), and sphingolipids (SLs). Sterols, mainly cholesterol in mammals and ergosterol in fungi, act primarily as membrane reinforcers but also have a crucial role in signaling. GPLs are frequently the main membrane components in cells (Casares et al. 2019). Phosphatidic acid (PA) serves as the precursor of the other main GPLs, of which phosphatidylcholine (PC) and phosphatidylethanolamine (PE) are zwitterionic, and phosphatidylserine (PS) and phosphatidylinositol (PI) are anionic. SLs derive from a sphingoid base, which can vary in length and composition. In mammals, sphingosine is the main sphingoid base, while dihydrosphingosine and phytosphingosine are preferred in yeast. This base can be N-acylated with a fatty acid chain to give raise to ceramides, and then be further modified with a selection of head groups to produce derivatives such as sphingomyelin and cerebrosides among many others (Harayama and Riezman 2018; Casares et al. 2019). Other phospholipids can be found in places where they serve a specific purpose. Such is the case of cardiolipin (CL), a structurally unique phospholipid found in the inner mitochondrial membrane. CL is necessary for mitochondrial functions, including the respiratory pathway, cristae formation, and mitochondrial fusion and fission (Paradies et al. 2019).

The lipidic environment of the cell must be tightly controlled to maintain transmembrane protein function (Contreras et al. 2011), and at the same time it must be adapted in response to changing conditions, such as temperature, osmosis, and metabolic changes (Klose et al. 2012). The cell takes advantage of the variety of GPLs and SLs to fulfill different roles in organellar membranes. This variety is accomplished through changes in the length and saturation of the acyl tails or the nature of the head group produces a phospholipid species with specific chemical characteristics that make it suitable for a certain role.

The properties of a membrane are further tailored by the ratios of lipid species that make them, as evidenced by the different lipid proportions found in different organelles (Ejsing et al. 2009; Klug and Daum 2014; Casares et al. 2019). The regulation of a membrane's properties through lipid species ratios can be taken one step further by the formation of lipidic microdomains, which provide the right environment for specific cell functions. One example is the inner leaflet of the PM, which in eukaryotes contains significant amounts of anionic PS and PI, while the outer leaflet is rich in PC and SLs (Ingólfsson et al. 2014).

The reason for the PI asymmetry is that they serve as spatiotemporal regulators of cell function by interacting with proteins in the membrane. Multiple domains such as Pleckstrin

domains and its homologs selectively interact with specific PI species to regulate protein function. This regulation involves protein recruitment to specific organelles, which can also be mediated by less specific domains such as polybasic surface patches. Other regulatory mechanisms include allosteric conformational changes in the target protein, and direct regulation of membrane proteins such as ion channels among others (Balla 2013; Hammond and Burke 2020). Additionally, PI gradients across two membranes in a MCS can be used as a counter-transport to facilitate the transport of other lipid species such as cholesterol (Mesmin et al. 2013; Hammond and Burke 2020).

Cells employ a wide array of enzymes such as phospholipases, lipid phosphatases, and acyl transferases to maintain availability of necessary lipid species, in addition to vesicular and non-vesicular transport to maintain the appropriate lipidic makeover in each organelle (Harayama and Riezman 2018).

The ER is the main lipid synthesizer in the cell, and lipid-transfer proteins (LTPs) at ER-PM contacts provide the PM with the phospholipids, sphingolipids, and sterols it cannot synthesize (Pichler et al. 2001; Toulmay and Prinz 2011; Stefan 2018), while also contributing to the PM's lipid compositional asymmetry (Lev 2010).

Saccharomyces cerevisiae offers a great opportunity to study ER-PM contacts because ~40% of its PM inner surface is covered in cER, by far the most abundant contact in the cell (Pichler et al. 2001; Manford et al. 2012). The six major tethers (Ist2, Scs2/22, and Tcb1/2/3) (Figure 2) responsible for the formation of these contacts are also known, and their deletion produces a "Δtether" phenotype in which virtually all the cER collapses to the cytoplasm (Manford et al. 2012) (Figure 3). Other proteins with a weaker tether function such as Ice2 (Quon et al. 2018) exist at these contacts and more might lay awaiting discovery, but their contribution to the formation of cER is minor in comparison to that of Ist2, Scs2/22, and Tcb1/2/3.

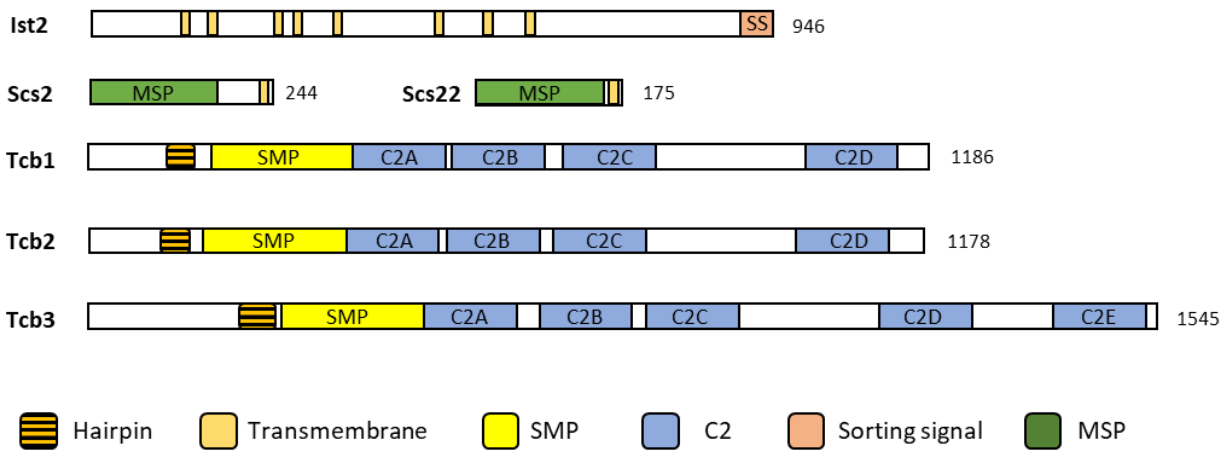

Figure 2. Domain structure of the six main ER-PM tethers, Ist2, Scs2/22, Tcb1/2/3.

The N-terminus is on the left side by convention. The numbers on the right side of the diagrams represent the total protein aminoacids.

2.2.1 IST2

From the six major tethers studied in this work, Ist2 is the only one without a clear orthologue in higher organisms. There are, however, proteins that structurally resemble the predicted domains of Ist2. The transmembrane protein 16 family (TMEM16), also known as anoctamins (ANO) comprises ten family members with eight transmembrane domains just like Ist2 is predicted to have with both N- and C-termini exposed to the cytosol (Pedemonte and Galietta 2014).

The first function associated with Ist2 was sodium resistance (Entian et al. 1999), which hinted to a possible shared role with TMEM16A/B in ion homeostasis. Nonetheless it has since been proven that this phenotype only appears in the double mutant *Δist2 Δbtn2* (Kim et al. 2005), and the only effect of Ist2 deletion on cell growth is a slight delay in the shift to exponential growth (Wolf et al. 2012).

The functions of most TMEM16 proteins remain obscure, but it is known that TMEM16A/B are calcium activated chlorine channels (Hartzell et al. 2009; Oh and Jung 2016) and TMEM16F/K are calcium activated phospholipid scramblases (Suzuki et al. 2013; Tsuji et al. 2019), which suggests a common calcium sensing function they could perhaps share with Ist2.

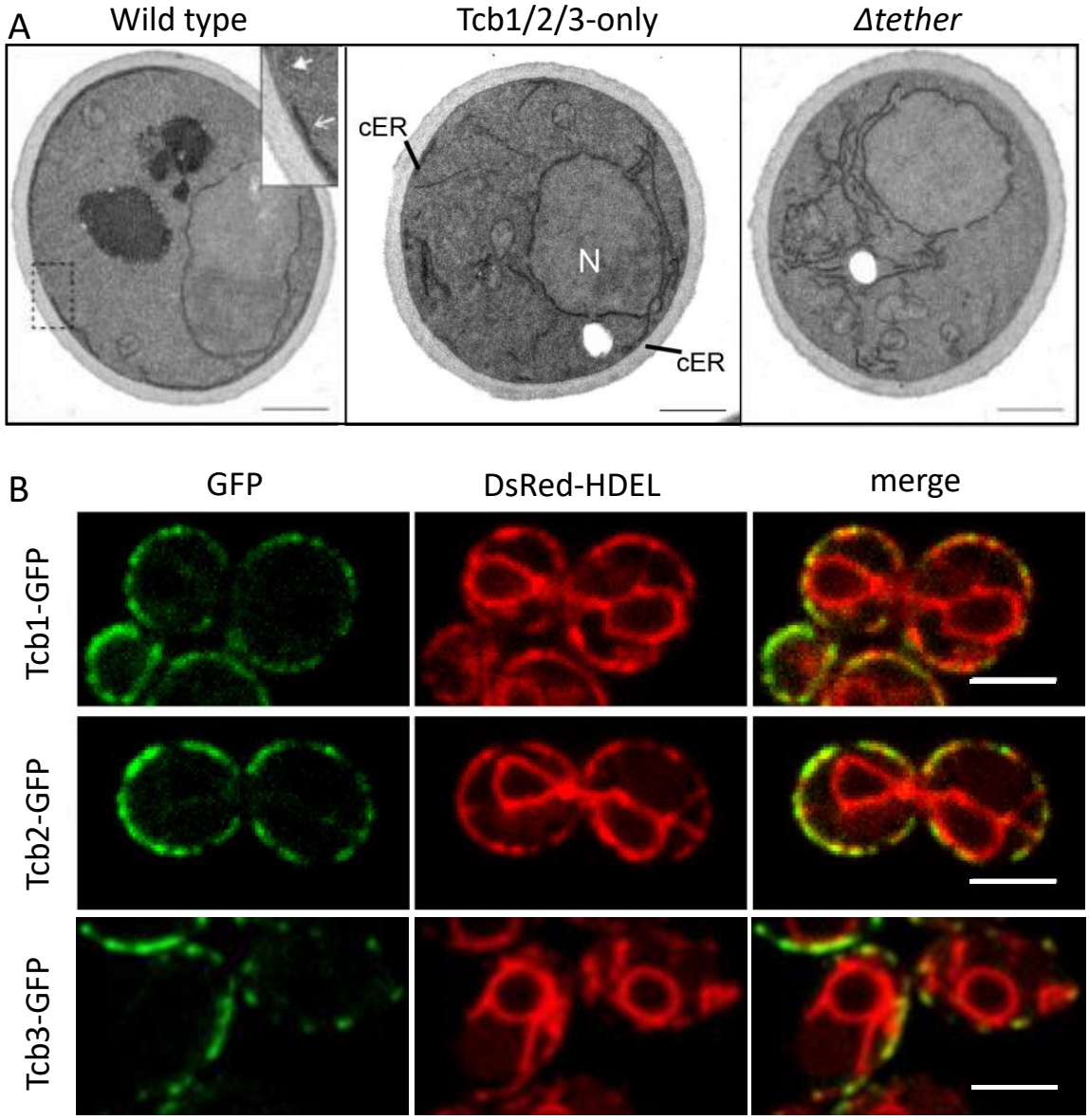

Figure 3. ER-PM tether localization.

(A) Electron microscopy of wild type, Tcb1/2/3-only, and *Δtether* cells. cER remaining in these mutants is indicated. Inset of wild type cell depicts regions of PM with (open arrow) and without ER (closed arrow). cER: cortical ER; N: Nucleus.

(B) Tcb1-GFP, Tcb2-GFP, and Tcb3-GFP localization in wild type cells expressing the ER marker DsRed-HDEL.

Scale bars: 500 nm (A), 3μm (B).

All images in Figure 3 are sourced from Manford et. al. 2012 with permission from Elsevier.

Another difference that sets Ist2 further apart from the TMEM16 family is cellular localization. TMEM16A/B/F localize to the PM, and TMEM16K localizes to ER-Lysosome MCSs (Suzuki et al. 2013; Petkovic et al. 2020). Ist2 on the other hand accumulates in the cER where it acts as tether between the cER and the PM (Manford et al. 2012; Wolf et al. 2012; Kralt et al. 2015; Petkovic et al. 2020). This is made possible because unlike TMEM16, Ist2 has a C-terminal sorting signal (SS) that binds the acidic phospholipid $PI(4,5)P_2$ at the PM through an amphipathic α-helix and basic aminoacids. It has been suggested that Ist2 oligomerization is also required for proper binding (Fischer et al. 2009).

Currently, Ist2 has been shown to be both a powerful tether capable of forming ~50% of wild type ER-PM contacts by itself (Manford et al. 2012), and the binding partner of Osh6/7 (Tong et al. 2013). A region in the middle of the Ist2 linker has been identified as the binding site for Osh6/7, and the corresponding binding site in Osh6 has also been determined. This interaction with Ist2 is essential to localize Osh6/7 to ER-PM contacts and for PS transport from the ER to the PM, which is required for Psd2-dependent PE synthesis (D'Ambrosio et al. 2020; Wong et al. 2021). Despite recent research, Ist2 remains a poorly studied protein with a long span of 340 aa that could be involved in other functions.

2.2.2 SCS2/22

Scs2/22 are a pair of protein orthologues of mammalian VAP proteins. It has been difficult to list all the functions of these proteins due to how they operate. VAPs are expressed in different tissues, in different organelles, and interact with a wide array of different proteins with equally varied proposed roles such as regulation of lipid transport and homeostasis, the unfolded protein response, and linking membranes and microtubules (Kagiwada et al. 1998; Lev et al. 2008). VAPs are also an important component of membrane trafficking, and mutations in the human VAP-B gene cause familial amyotrophic lateral sclerosis (ALS8) and late-onset spinal muscular atrophy (SMA) probably related to an impairment of this function (Nishimura et al. 2004).

Structurally, VAPs and Scs2/22 are type II, tail-anchored, integral ER proteins. They all possess a cytosolic MSP (major sperm protein) homology domain and a C-terminal transmembrane domain. In the case of VAPs these tails are longer and can mediate dimerization, while in Scs2/22 the tails are shorter and likely unsuitable to mediate oligomerization. This difference has been presented as a possible reason for the incomplete rescue of *Δscs2Δscs22* mutant by VAP-A. (Kaiser et al. 2005; Loewen and Levine 2005).

2.2.2.1 MSP-FFAT interactions and phospholipid metabolism at ER-PM contacts

MSP homology domains have the ability to bind proteins with an FFAT motif (FF in acidic tract) (Loewen and Levine 2005). In yeast, at least three proteins containing FFAT motifs localize to the ER-PM contacts, Opi1, Osh2, and Osh3 (Loewen et al. 2003), and it is important to understand their interactions with Scs2/22 to better comprehend their role in ER-PM tethering.

The primary phenotype for *Δscs2Δscs22* mutant is inositol auxotrophy through the silencing of the INO1 gene, which encodes Inositol-3-phosphate synthase, a necessary protein in inositol metabolism (Kagiwada et al. 1998; Kagiwada and Zen 2003). Opi1 is a transcriptional repressor of gene INO1, and it binds to Scs2 at the ER-PM contacts through the FFAT-MSP interaction (Kaiser et al. 2005). When Scs2 is not present, Opi1 localizes to the nucleus and represses INO1 causing inositol auxotrophy (Lev et al. 2008). Although deletion of Scs22 fails to cause inositol auxotrophy, the phenotype of *Δscs2* strains is exacerbated in the double mutants, which suggests a minor but parallel role for the more primitive Scs22 (Loewen et al. 2003; Loewen and Levine 2005).

Osh2/3 are part of the Osh family and they (Tong et al. 2013) contain in addition to ORD a PH (Pleckstrin homology) domain, and an FFAT domain. They localize to the ER-PM contacts by binding phosphoinositides in the PM with their PH domain and the MSP domain of Scs2 with their FFAT domain, effectively bridging the ER-PM gap (Schulz et al. 2009; Stefan et al. 2011; Weber-Boyvat et al. 2015). Unlike their homologs Osh6/7 which also localize to the ER-PM contacts, Osh2/3 contribute to sterol transport at endocytic sites (Encinar del Dedo et al. 2017). Once at the contact, they use their ORD to present ER-resident proteins like Sac1 and Opi3 with their substrates PI4P and PME/PE, both lipid species located in the PM, allowing them to act in *trans* (Stefan et al. 2011; Tavassoli et al. 2013).

2.2.2.2 Scs2/22 as tethers

Deletion of Scs2/22 causes a drastic reduction (~50%) in cER (Manford et al. 2012). Since the discovery that the MSP domain of Scs2 could bind phosphoinositides in vitro (Kagiwada and Hashimoto 2007) and that this was necessary for its activity, it has been hypothesized that Scs2/22 could bridge the ER and the PM on their own.

However, the binding of phosphoinositides to Scs2 MSP was found to influence its ability to bind FFAT domains (Lev et al. 2008), suggesting that instead of tethering directly, it could

perform this function by interacting with FFAT containing proteins Osh2 or Osh3. It is worth noting that neither of these proteins seem to interact with Scs22 (Weber-Boyvat et al. 2015) and therefore they might not actually act as a tether. This would agree with the fact that deletion of Scs22 alone does not appear to decrease the amount of cER (Loewen et al. 2007).

There is still much to learn about the role of Scs2/22 in ER-PM contacts, and the possibility of unknown interactions with either lipid species or non-consensus FFAT domains cannot be dismissed.

2.2.3 TCB1/2/3

Tcb1/2/3 (tricalbins) are orthologues of mammalian extended synaptotagmins (E-Syts) which are also present in plants and other fungi (Saheki and de Camilli 2017a). The structure of tricalbins is comprised of three different domains, an N-terminal transmembrane domain anchored in the cER, followed by a cytosolic SMP domain and a variable number of C2 domains. E-Syts share this same domain architecture and show important parallelisms in the distribution of their C2 domains.

E-Syt1 has five C2 domains like Tcb3, and even though E-Syt2/3 have three C2 domains while like Tcb2/3 contain four, both groups have a C-terminal C2 domain separated from the others which cluster near the SMP (Lee and Hong 2006; Saheki and de Camilli 2017b). It is worth mentioning that AlphaFold (Jumper et al. 2021) predicts an additional C2 domain between C2C and C2D for all tricalbins. However, their existence has yet to be proven.

Tricalbins likely tether the PM in the same way as E-Syts do, forming homo and heterodimeric complexes that bind $PI(4,5)P_2$ in the PM through their C2 domains (Toulmay and Prinz 2012; Reinisch and De Camilli 2016). Despite being true tethers, tricalbins have a smaller contribution to ER-PM contact formation compared to the other tethers (Manford et al. 2012) and likely have other functions. E-Syts have been proven to have calcium dependent lipid shuttling capabilities in vitro (Toulmay and Prinz 2012; Burgoyne et al. 2014; Lahiri et al. 2015) and this function might be shared by tricalbins and other E-Syts.

2.2.3.1 N-terminal membrane-anchoring domain

Both E-Syts and tricalbins have an N-terminal hydrophobic transmembrane domain to anchor them to the ER membrane. The hydrophobic stretch (30 amino acids in E-Syts and 40 in

tricalbins) is longer than most membrane anchors in other proteins, and folds to form a wedge or hairpin-like structure. For E-Syts this hairpin enters only the external layer of the membrane, while the greater length and presence of a hydrophilic amino acid in tricalbins' hairpins seem to suggest a full insertion in the bilayer (Giordano et al. 2013).

Other ER resident proteins contain similar structures, like the reticulon homology domain (RHD) of reticulons, which are ubiquitously distributed in all eukaryotes. The forces created in the membrane by the hairpin insertion help localize the reticulons to tubular ER, where the membrane curvature offers a more energetically favorable environment for the hairpin. When overexpressed, the forces created by the reticulons' hairpins are enough to induce the formation of tubular ER (Oertle et al. 2003; Voeltz et al. 2006; Nziengui and Schoefs 2009). It is sensible to hypothesize that the hairpins of tricalbins and E-Syts share a similar function and mediate their localization to curved ER membranes (Hoffmann et al. 2019).

2.2.3.2 SMP

SMP-containing proteins are members of the tubular lipid-binding (TULIP) superfamily and share a similar fold with the other two groups that comprise the superfamily, BPI-like and Takeout-like proteins. Unlike the other two groups, proteins with SMP also contain additional domains including putative transmembrane domains (Lee and Hong 2006; Kopec et al. 2010; Kopec et al. 2011).

The structure of an SMP domain consist of a beta barrel made of a beta sheet and two alpha helices (H1 and H3), with a third helix (H2) acting as a partial lid to one end of the barrel (Schauder et al. 2014). SMP domains can dimerize through the uncapped end of the barrel, and in the case of E-Syts this dimerization is necessary for lipid transport in vitro (Schauder et al. 2014; Reinisch and De Camilli 2016). Along the length of the dimer there is a hydrophobic groove that can accommodate the chains of two glycerophospholipids per monomer at the same time. The head groups remain outside the barrel, allowing the SMP domain to bind a wide variety of lipid species (Toulmay and Prinz 2012; Schauder et al. 2014).

Yeast expresses seven SMP-containing proteins: Mmm1, Mdm12, and Mdm34 in the ERMES complex at ER-mitochondria MCSs, Tcb1, Tcb2, and Tcb3 at ER-PM contacts, and Nvj2 at the nucleus-vacuole junction (Toulmay and Prinz 2012; Schauder et al. 2014; Reinisch and De Camilli 2016). All seven SMP-like proteins in yeast target MCSs, and mammalian SMP-containing proteins localize to MCSs too when expressed in yeast. The SMP domain is necessary for localization to the MCSs, but for some proteins like Nvj2 and tricalbins other domains (PH and C2

respectively) are also needed for localization. The ability of SMP-containing proteins to bind lipids at places of close proximity between membranes indicates a role in lipid shuttling (Kopec et al. 2010).

2.2.3.3 C2 domains

C2 domains are widespread calcium binding domains made of eight strands arranged in a beta sandwich. Proteins containing only one C2 domain tend to be involved in calcium dependent signaling, while proteins containing tandems of them usually have a role in membrane trafficking (Martens and McMahon 2008). The calcium binding pocket is made up of two to three loops on one end of the beta sandwich that in most cases contain up to five acidic residues (Schulz and Creutz 2004; Min et al. 2007).

These domains exist in two topologies, I and II, and they differ from each other in the shift of one strand. It has been hypothesized that the existence of two topologies could determine the relative position of the C2 domain with respect to neighboring domains (Sutton et al. 1995; Rizo and Sudhof 1998). All C2 domains in both E-Syts and tricalbins have topology II (Creutz et al. 2004; Min et al. 2007).

C2 domains can bind acidic phospholipids through electrostatic interactions, and it can be done either dependently or independently of calcium binding. In some cases, the binding of calcium neutralizes the negative charge of the acidic residues in the pocket allowing a basic patch in the C2 domain's surface to bind the negatively charged phospholipids. C2 domains lacking the acidic residues at the pocket could bind acidic phospholipids constitutively, and those that lack a basic patch could still bind phospholipids through the imperfect coordination sphere of bound calcium (Rizo and Sudhof 1998; Giordano et al. 2013; Xu et al. 2014). The C2 domain tandem of E-Syts and tricalbins does not participate directly in membrane trafficking but they bind the negatively charged $PI(4,5)P_2$ at the PM and localize the protein to the ER-PM contacts (Toulmay and Prinz 2012; Giordano et al. 2013; Idevall-Hagren et al. 2015).

The calcium binding ability of individual C2 domains is difficult to discern through sequence analysis alone. C2 domains bind calcium with varying degrees of affinity and some do not bind calcium despite having the required acidic residues (Min et al. 2007; Martens and McMahon 2008). Likewise, their lipid binding capabilities are very difficult to address without molecular and cell-biological data.

2.2.3.4 The cellular functions of the E-Syt protein family

Across different organisms, E-Syts share the same basic domain structure comprising an ER membrane anchor, SMP, and C2 domains in variable number. However, the number of E-Syts an organism maintains varies greatly, with mammals and yeast having three while *Caenorhabditis elegans* and fruit flies only have one (Kikuma et al. 2017; Saheki and de Camilli 2017b; Nath et al. 2020). It is worth mentioning however that E-Syt in flies has four isoforms that could provide some variability in function. Remarkably, plants have as many as seven E-Syt orthologs, with several of them being tissue specific (Pérez-Sancho et al. 2016; Ishikawa et al. 2020). Organisms with multiple E-Syts could potentially use this variability to fulfill specific roles.

E-Syts are also highly variable in their number of C2 domains. Plant Syt1-5 and *Trypanosoma brucei* TbE-Syt1 have only two C2 domains, while fruit fly E-Syt has three, and mammalian E-Syt1 and yeast Tcb3 have as many as five (Manford et al. 2012; Kikuma et al. 2017; Saheki and de Camilli 2017b; Nath et al. 2020; Stepinac et al. 2021). E-Syts have at least one C2 domain that constitutively binds negatively charged phospholipids in the inner leaflet of the PM, effectively localizing them to the ER-PM contacts (Manford et al. 2012; Pérez-Sancho et al. 2015; Kikuma et al. 2017; Saheki and de Camilli 2017b). The presence of a calcium binding pocket in some C2 domains suggests a mechanism in which calcium binding strengthens the binding to the PM (Idevall-Hagren et al. 2015; Benavente et al. 2021).

Possessing a lipid binding SMP domain and localizing to the ER-PM contacts, E-Syts are in a privileged position to shuttle lipids between these organelles, which seems to be the underlying function of their protein family. The hydrophobic groove that runs the length of the SMP domain can accommodate the acyl chains of a variety of lipids, and it has been suggested that this indicates a lack of specificity (Schauder et al. 2014). However, studies on *Arabidopsis thaliana* Syt1 reveal a preference for long chained diacylglycerols (DAG), although the selection mechanism for these particular lipids is not fully understood (Ruiz-Lopez et al. 2021).

Beyond a role in lipid transport at MCSs, determining the exact, purportedly conserved role of E-Syts has proven challenging. In metazoans, the specific role of mammalian E-Syts in ER-PM lipid transport remains elusive due to the absence of an overt phenotype after E-Syt deletion (Sclip et al. 2016). In flies, E-Syt has been found to have a role modulating lipid metabolism at synapses, as well as facilitating neurotransmitter release in response to calcium and helping retinal degeneration protein B (RDGB) localize to ER-PM contacts (Kikuma et al. 2017; Nath et al. 2020). However, deletion of fly E-Syt does not affect lipidic balance at the synapse neither impedes photoreception.

It has been suggested that one of the causes for the mild to non-existing phenotypes in metazoan E-Syt deletion mutants could be the importance of the processes they are involved in. Redundant regulatory mechanisms could be compensating for the effects of E-Syt deletion in essential tasks, such as lipid homeostasis at the synapse. In addition, despite being expressed in all cells, the effects of their deletion remain unstudied in a majority of tissues (Saheki and de Camilli 2017b).

In plants, Syt1 has emerged as a key component of PM homeostasis maintenance in response to abiotic stress (Pérez-Sancho et al. 2015). Syt1 is thought to maintain the lipidic balance at the PM by removing excess DAG generated by lipid signaling at the PM. The other plant E-Syts have yet to be studied in detail, but it has been hypothesized that they could respond to different types of stresses and complement the function of the ubiquitous Syt1(Ruiz-Lopez et al. 2021). A similar role in PM homeostasis has been found in yeast tricalbins, as they contribute to maintaining PM integrity under heat stress (Omnus et al. 2016). This suggests a function that could be common to all E-Syts, protecting the PM from different stresses by shutting lipids from the ER to the PM.

2.3 Electron tomography

MCSs can sometimes be extensive structures large enough to be visualized by light microscopy, such as ER-PM contacts in yeast. However, the main focus when studying MCSs is in the events that take place at the cleft between the membranes of the contacting organelles.

The dimensions of the cleft are smaller than the maximum resolution achievable by light microscopy, which is limited by the light wavelength of 4 - 7 x 10^{-7} m, and reliance on fluorescent tags limits the data obtained to a handful of tagged proteins at the contact. Using electron microscopy (EM) solves both problems. The shorter wavelength of electrons (1.96 x 10^{-12} m at 300kV) allows for much higher resolution, and electron tomography captures the contact in its whole biological context.

However, despite its many advantages this technique comes with its own shortcomings. Unlike photons, electrons interact with matter, hence the need to keep the sample under high vacuum to prevent interactions between the electron beam and air. This ultimately makes it incompatible with live-cell imaging and limits its use to fixed samples.

2.3.1 The transmission electron microscope

A transmission electron microscope (TEM) usually consists of nine different elements kept in high vacuum (Figure 4). The electron gun (1) is the source of the electron beam. In modern microscopes it is usually a field emission gun (FEG) that uses high voltages, in the range of 300 kV to accelerate electrons. Currently, FEGs provide the best beam coherence and energy distribution of all electron guns. Below it, a series of condenser lenses and apertures (2) allow for manipulation of the beam to, like their name implies, condense the beam to a small area of the specimen and regulate its intensity.

The specimen is positioned on a grid, supported by a computerized stage (3) that can adjust the specimen's position in three axes, while also being able to rotate along a predetermined axis for tomography. The objective lens (4) is responsible for forming the image of the specimen. After this point, greatly scattered electrons are filtered out by the objective aperture (5), increasing signal-to-noise ratio (SNR). The image is later magnified and rotated by the intermediate lenses (6), and then projected into the detector by the projector lens (7). Modern microscopes may also be equipped with an energy filter (8) before the detector to filter out inelastically scattered electrons that have passed the objective aperture, reducing chromatic aberrations (Lučić et al. 2005; Egerton 2016).

Traditionally, detectors (9) where coupled charged detectors (CCD), and they used a scintillator to transform the electron signal to light, which would then be detected by the CCD chip. The series of intermediate steps before detection introduced noise and affected the contrast of the image, which was greatly improved by the introduction of direct electron detectors (DED) (Li et al. 2013; Ruskin et al. 2013). These detectors rely on a Complementary Metal Oxide Semiconductor (CMOS) sensor to digitally record the electrons. They also improve quantum detection efficiency, allowing for higher resolution. Shifts in the cryo-stage caused by mechanical influence or temperature fluctuations can move the sample, and the incident electrons can also create both global and local motion in the specimen (Zheng et al. 2017). The faster readout of these detectors makes it possible to acquire several frames per image, which can later be aligned to reduce motion blur in a reconstructed mage (Ruskin et al. 2013).

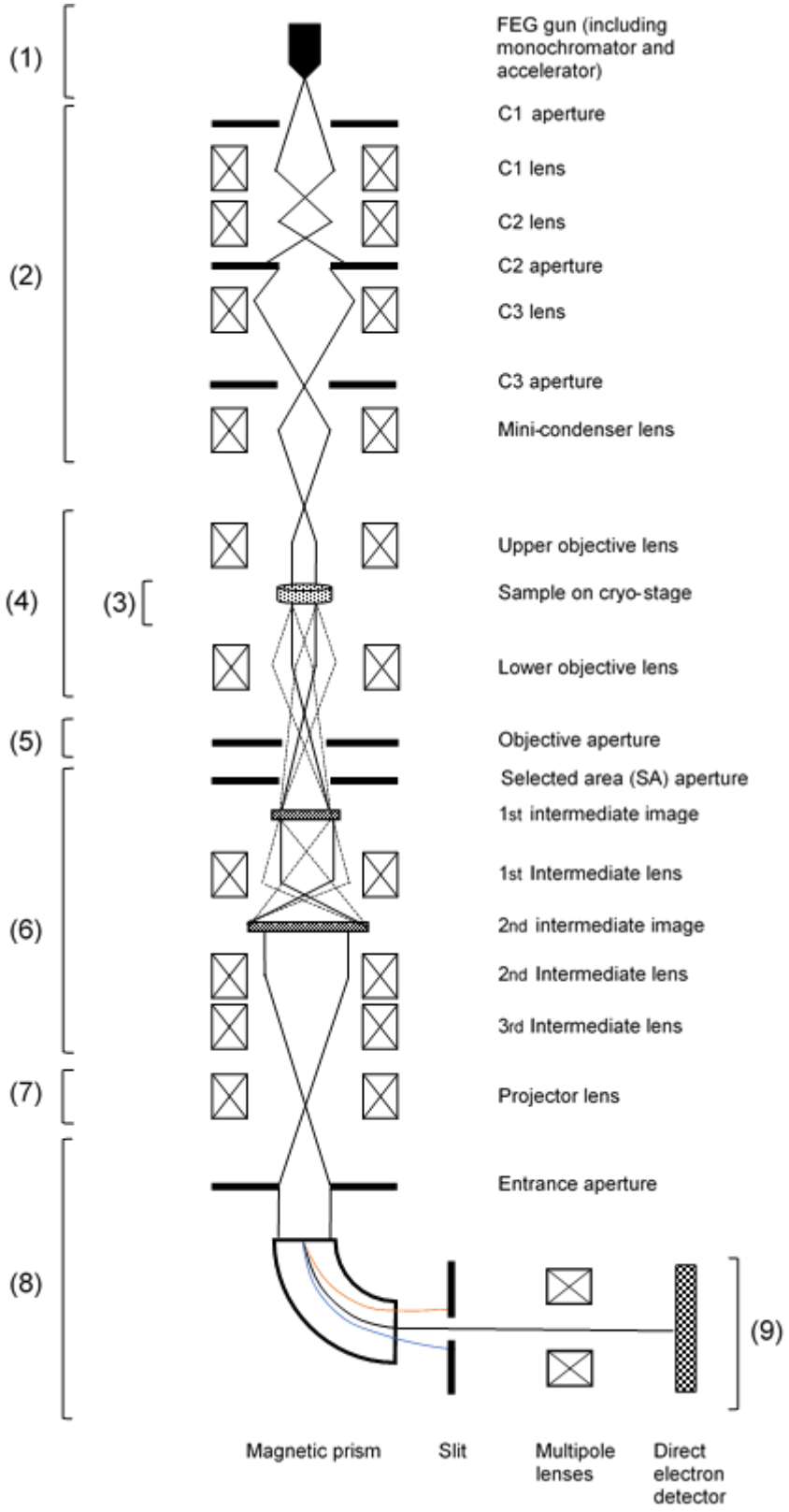

Figure 4. Schematic diagram of a modern transmission electron microscope like the one used for this work (FEI Titan Krios). It depicts the electron gun (1), condenser lens system (2), computerized cryo-stage (3), objective lens (4) and aperture (5), intermediate lens system (6), projector lens (7), post-column energy filter (8), and direct electron detector (9).

2.3.2 Electron interactions with biological matter

Interactions between the beam of electrons and the sample can take the form of elastic or inelastic scattering (Reimer and Kohl 2008; Williams and Carter 2009). In an elastic scattering event the electron interacts with the electrostatic potential of the atoms in the sample and is deflected from its original path with negligible loss of energy. By contrast, in an inelastic scattering event the electron transfers significant energy to the sample, which can potentially bring electrons in the sample to excited states. Most of these scattering events are caused by interactions between the beam electrons and the nucleus of atoms in the sample. As such, the deflection angle of the electron is higher the heavier the elements in the sample are. In the case of biological samples, most atoms belong to light elements and the scattering angles are relatively small.

The formation of free radicals and heat and X-ray emission can damage the sample, causing what is collectively referred to as "radiation damage" by the community. This includes hydrogen formation from water radiolysis, which can interact with proteins in the sample, resulting in bubbles that deform and distort the structure (Reimer and Kohl 2008; Williams and Carter 2009). The chance of an electron undergoing a scattering event is directly related to the thickness of the sample. The mean free path, the average distance traveled before losing energy, of an electron accelerated to 300 kV is approximately 350 nm in vitreous ice (Yan et al. 2015), which mandates samples to be as thin as possible to minimize radiation damage.

2.3.3 Image formation and contrast in EM

Contrast drives image formation. Scattering, both elastic and inelastic, contribute to contrast via two different mechanisms (Reimer and Kohl 2008).

Amplitude contrast is the most straightforward of the two. Electrons scattered at high angles are filtered out by the objective aperture and fail to reach the detector, which translates to lower intensities corresponding to the areas that caused the scattering events. The light atoms in a biological sample do not scatter enough electrons at high enough angles to be filtered out, therefore amplitude contrast has only a minimal contribution to contrast, unless heavy metal stains are used (Orlova and Saibil 2011).

The second contrast mechanism is phase contrast. When the planar wave of an electron scans the sample, its elastically scattered components undergo a wavelength phase shift. This phase shift is slight due to the light nature of atoms in the sample. All these components are brought together at the back-focal plane by the objective lens, where their phase shifts and

different path lengths cause them to interfere constructively and destructively in an oscillatory manner (Frank 2006). Defects in the objective lens such as spherical and chromatic aberration and axial astigmatism contribute to this interference, and ultimately influence phase contrast and limit the maximum resolution. Spherical aberration happens because the electron beams that are not perfectly parallel to the imaging axis have a longer focal length than parallel ones, causing a point to appear blurred. Chromatic aberration is caused by differences in the energy of image-forming electrons. Modern microscopes have compensatory systems to ensure uniformity of electron energy at the source. However, inelastic scattering with the sample can cause some electron to lose energy, hence the use of post-column energy filters. Finally, axial astigmatism is defined by the deformation of a circular beam into an ellipse due to an asymmetric objective lens (Williams and Carter 2009; Frank 2010).

The resulting electron interference is represented in Fourier space by the contrast transfer function (CTF) as a function of spatial frequency (u) (Eq. 1), and is affected by the defocus applied (Δf) and the acceleration voltage (λ), as well as defects in beam coherence and spherical aberration (C_s) (Lučić et al. 2005; Frank 2010).

$$CTF(u) = \pi \Delta f \lambda u^2 + \frac{1}{2}\pi C_s \lambda^3 u^4 \qquad Eq.(1)$$

The CTF depicts a loss of information at high spatial frequencies caused by the dampening of the amplitude and the presence of points of null amplitude or "zero crossings", which limit the maximum resolution achievable. The CTF can later be corrected to access this high-resolution information, mainly by inverting the negative amplitude regions and fitting the CTF to a predicted power spectrum (Figure 5) (Mindell and Grigorieff 2003; Fernández et al. 2006).

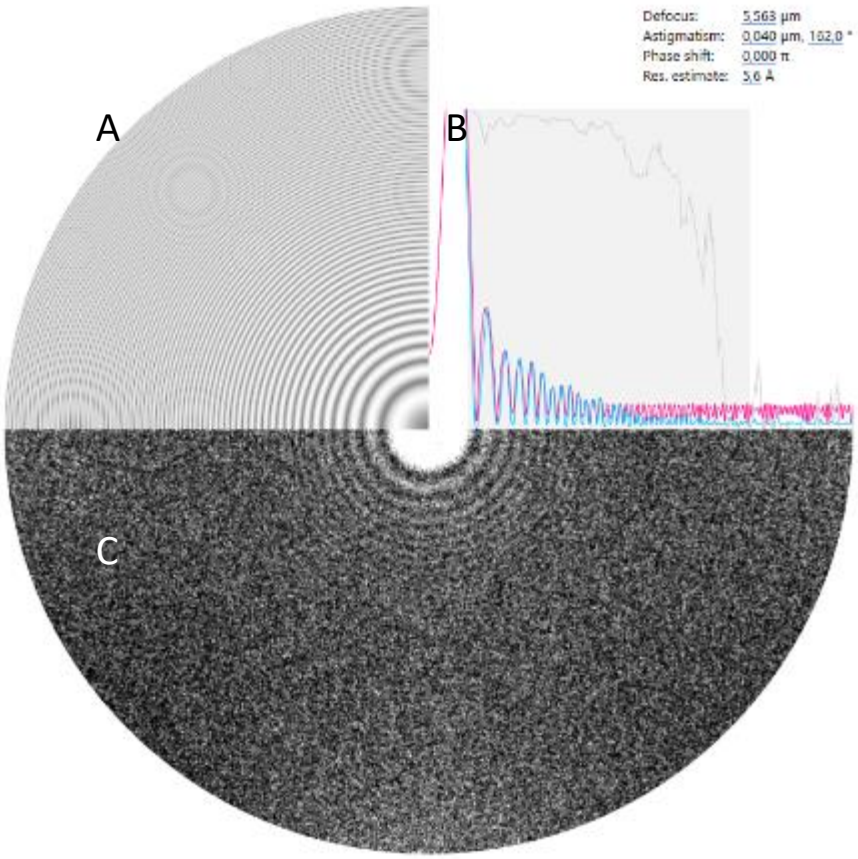

Figure 5. Example of CTF correction.

Predicted 2D CTF of micrograph (A), power spectrum of the image (blue) and fitted power spectrum (pink) (B), and Fourier transform of the real space micrograph (C).

Image obtained using Warp (Tegunov and Cramer 2020).

2.3.4 Cryo-electron microscopy and cell vitrification

As previously mentioned, the sample in an electron microscope needs to be fixed to prevent evaporation in the high vacuum of the microscope's column. Cells can be chemically fixed with glutaraldehyde or formaldehyde, or cryo-fixed by freezing. In room temperature EM, this is followed by dehydration with an organic solvent, usually acetone. In the case of cryo-fixed samples this process is called freeze-substitution. A contrast-enhancing dye such as osmium tetroxide (OsO_4) can be added to stain membranes at this point. Afterwards, the cells are embedded in resin and sliced thinly using different methods. These thin sections can be further stained with heavy metals such as uranyl acetate, which interacts with phosphate groups and stains membranes and nucleic acids (Watson 1958; Frank 2006).

Plastic sections have been a great aid in studying cellular structure and continue to be in use. However, chemical fixation and subsequent dehydration of the cell introduce artifacts in membrane morphology and cause protein aggregation (Dubochet and Sartori Blanc 2001). The use of heavy metal stains is also problematic, because the features observed correspond to the metal ions and not the actual biological material. These constraints limit the usefulness of plastic sections when studying MCSs, especially when focusing on membrane morphology. Cryo-electron microscopy (Cryo-EM) allows for the imaging of fully hydrated frozen samples, in which cellular contents remain in close-to-native conditions. To achieve this state, water in the sample needs to be vitrified, that is kept in an amorphous ice state. Otherwise, ice crystals would disrupt the cell's architecture (Dubochet et al. 1988).

The vitrification procedure in Cryo-EM relies on exposing the sample to a cryogen at fast enough speeds to ensure quick sample freezing. The cryogen needs to fulfill certain criteria to successfully freeze the sample in a short enough time. The first is that it needs to be at a temperature compatible with low-density vitreous ice, at least -150°C. Secondly, it needs to have good heat-transfer properties to quickly freeze the sample. Liquid ethane or a propane-ethane mixture are the cryogens commonly used for this task (Frank 2010).

Cells are grown or deposited on a grid and quickly plunged into the cryogen. The sample is only properly vitrified to a depth of just a few micrometers, limited by the heat transfer properties of the cryogen. Excess medium is blotted away from the grid before plunging to help the cells come in direct contact with the cryogen, maximizing its effectiveness (Frank 2010). Cryo-protectants such as glycerol can also be used to increase this range, but larger samples such as multicellular organisms or tissue need to be frozen through other means such as high-pressure freezing (Studer et al. 2008). In the case of yeast, its small size and relatively dense cytoplasm make it suitable for plunge freezing. With the notable exception of the vacuole lumen, the contents of yeast cells are usually satisfactorily vitrified using this method.

Having a frozen sample nonetheless prevents the use of certain techniques, such as immunostaining or heavy metal staining. Even though large macromolecular complexes such as ribosomes and even proteasomes can be recognized and provide valuable context, membrane morphology is the main guide for feature identification in the absence of labelling. Only recently the successful implementation of Cryo-light microscopy is allowing researchers to correlate fluorescent information and Cryo-EM imaging (Rigort et al. 2012; Arnold et al. 2016).

2.3.5 Cryo-electron tomography

The principle of Cryo-electron tomography (Cryo-ET) relies on the possibility of reconstructing a 3D volume with information from 2D projections. The central slice theorem specifies that the Fourier transform of a 2D projection of a 3D volume at a certain angle corresponds to a central section of the Fourier transform of the imaged volume at the same angle (Crowther RA et al. 1970). To obtain 2D projections of a sample, it is positioned in a stage that can rotate along an axis. The stage is rotated in steps, and allowed some time to settle its motion before an image is taken (Figure 6A-C). It is important that the area to be imaged is positioned at the eucentric height, the same height as the rotation axis. Otherwise, the image would move laterally after changing the tilt.

Small position shifts can still occur due to deviations from the eucentric height and sample movement and deformation. Changes in sample height affect its position with respect to the focal plane, as well as causing the region of interest to drift away as the sample tilts. In order to minimize this, a region in the lamella is defined to perform position and focus corrections after every tilt. It is important that this area is along the same rotation axis as the region of interest so that they maintain a similar height regardless of the tilt angle. It is also critical that this trial region and the record area are separate to avoid excessive radiation damage to the region of interest.

The recorded images can then be aligned and back-projected to obtain a 3D reconstruction of the sample (Figure 6D). Hypothetically, this could be done for the whole 180° rotation of the sample, which would result in a perfectly isotropic reconstruction. However, the grid the lamella rests on blocks the beam at very high tilts, limiting the maximum tilt angle. Additionally, as the lamella tilts the path the electron must travel through the sample increases, and so does the noise. These high tilts are therefore not as informative as low tilts and they require a higher electron dose that could be better employed at lower tilts, so images at tilts higher than 60° are usually not taken. However, this causes another problem, the missing wedge. This is a missing wedge-shaped area on the 2D Fourier transform of the tomogram corresponding to the missing projections of the tilt series. The loss of high tilt images causes a loss of information in the axis perpendicular to the lamella. This results in an elongated dimension along the electron path. Increasing the space between tilts to allocate more electron dose to higher tilts does not solve the problem, as it can lead to loss of information at higher resolutions if the Fourier slices are not thick enough to fill Fourier space. The maximum resolution achievable without loss of information is determined by the Crowther criterion $m=\pi*D/d$, where the resolution (d) is limited by the diameter of the particle (D) and number of evenly distributed tilt images (m) (Crowther RA et al. 1970). In

summary, a balance must be found between oversampling to reduce missing wedge at the expense of dose per tilt and decreasing the total dose by acquiring fewer tilts (Frank 2006).

Several different schemes exist to acquire a tilt series. The unidirectional scheme is the most intuitive, as it starts at a high tilt and continues until its opposite angle, covering the whole tilt range without changing directions (Figure 6A). Its main advantage is speed, but it wastes too much dose at the start on high tilts that could be better spent at lower tilts, where the effective thickness of the sample is lower.

To fix this, a bidirectional tilt scheme starts acquisition at a low tilt angle and moves through the 0° tilt before ending at an opposite high tilt. A second tilt series is acquired in the opposite direction. Both series are combined in a single tilt series, with lower tilts having received significantly more dose than high tilts (Figure 6B). However, acquiring a second tilt series on a sample that has already been exposed complicates reconstruction due to radiation damage. This complicates the alignment and combination of the two-tilt series, hence why the bidirectional acquisition scheme is seldom used (Baker and Rubinstein 2010).

The most modern scheme, the dose-symmetric series (Hagen et al. 2017), starts at 0° tilt and acquires first at low tilts on both directions, switching back and forth between directions as the tilt angle increases (Figure 6C). The result is a tilt series where low tilts are imaged first, avoiding damage to the areas with the most information. The downside to this scheme is that frequent direction shifts require constant realignment of the stage to keep the image centered on the same area, increasing acquisition times. Taking all this into account, the dose-symmetric scheme is currently regarded as the most suitable for Cryo-ET.

2.3.6 Focused ion beam milling

In Cryo-EM the electron dose is the fundamental limit to resolution because of radiation damage. Vitrified samples are damaged directly by inelastic electron interactions, and later by emitted secondary electrons and hydrogen gas formation within the sample, which causes an easily identifiable "bubbling". For this reason, the total electron dose at a single spot is kept roughly at 100 $e^-/Å^2$ for tomography (Baker and Rubinstein 2010).

With such a modest dose, signal-to-noise ratio drops rapidly in thick samples. The solution lies on thinning down the sample to thicknesses lower than 300 nm, for which several methods exist (Thompson et al. 2016). Thin sections can be obtained out of a high-pressure frozen sample with the use of an ultra-cryomicrotome, which are then deposited on a grid for imaging. However,

the action of the blade on the sample is prone to causing artifacts such as knife marks and sample compression (Al-Amoudi et al. 2004).

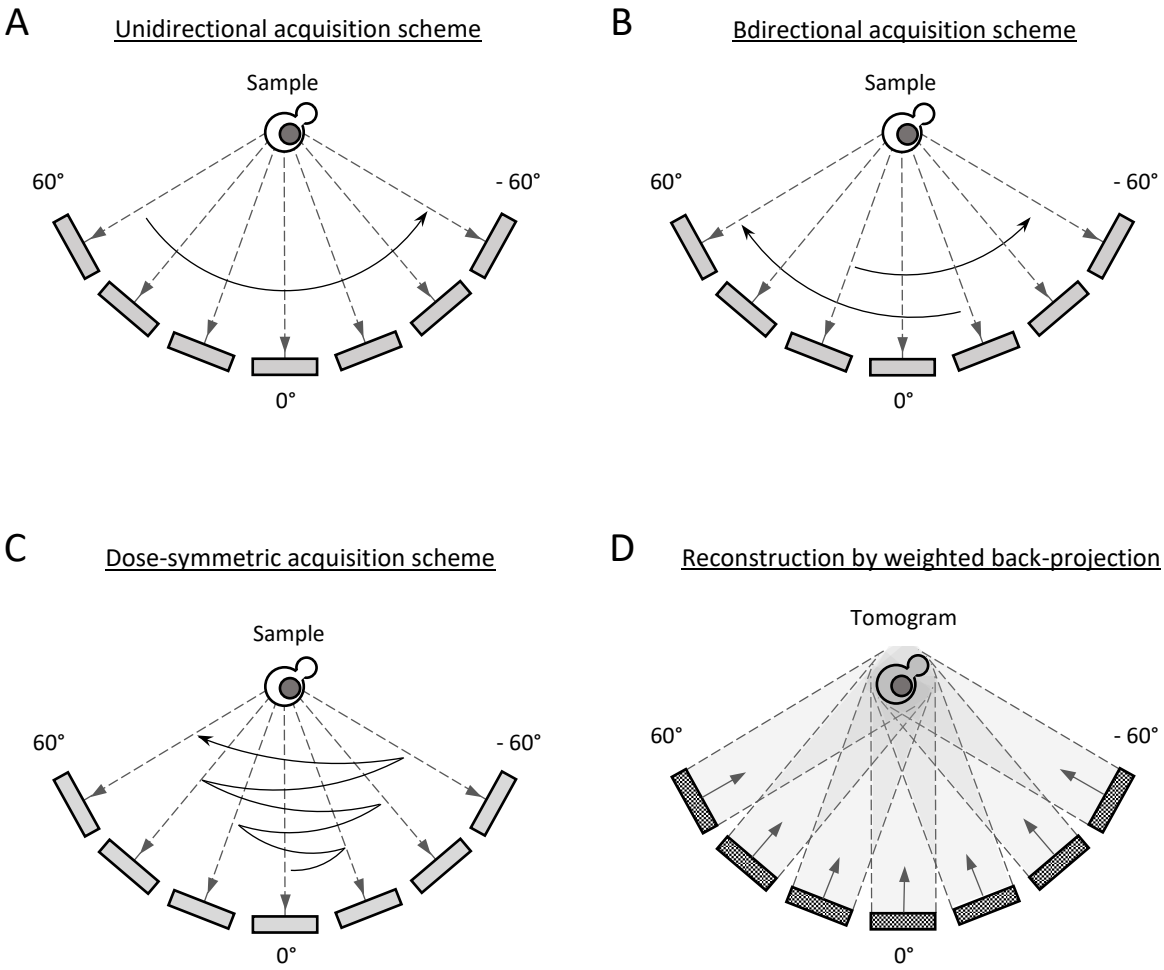

Figure 6. Cryo-electron tomography.

(A-C) Tomography acquisition schemes; unidirectional (A), bidirectional (B), and dose-symmetric (C). The direction of the electron beam relative to the stage at different tilt angles is represented by dashed grey arrows. The direction of stage movement during acquisition is represented by solid black arrows. Grey rectangles represent tilt views.

(D) Principle of back-projection reconstruction. The direction of the projections is indicated by solid grey arrows. Patterned rectangles represent aligned tilt views.

Cryo-focused ion beam (FIB) milling machines have become the norm for thinning down vitrified cellular samples. This method does not rely on mechanical sectioning; therefore, it does not suffer from the artifacts associated with it. Instead, it uses a focused gallium ion beam to remove material from the sample (Figure 7). Ions are extracted from the gallium source and

accelerated towards an area in the sample targeted for milling. The ion beam scans the designated milling area in a rastering fashion, and the high kinetic energy of the relatively heavy ions removes parts of the sample upon impact. Secondary electrons emitted by the sample can be detected by a surface scanning microscope (SEM) element to help monitor the process (Rigort et al. 2012; Schaffer et al. 2017). The milling areas are selected above and below the plane of interest in the sample, and they gradually approach this plane until the material between them achieves the desired thickness. The resulting thin section of the sample is called a lamella (Figure 7).

Despite its many advantages, Cryo-FIB milling poses challenges unique to it that complicate the production of lamellas suitable for Cryo-ET.

Vitrification of large multicellular samples has become possible through the use of high-pressure freezing (HPF), but the thicker sample dramatically increases the amount of time needed to remove the material above and below the lamella.

One solution was found in the form of “lift-out”, where a section of the sample is freed from the bulk using the FIB and then mounted on a support where it can be milled like a conventional lamella (Schaffer et al. 2019). More recently the “waffle method” has been used for samples up to tens of micrometers in size. It consists on milling the front and back of the lamella position on a high-pressure frozen sample at high angles, and later tilting the sample back and milling above and below the lamella in a conventional way (Kelley et al. 2021).

Another problem is surface contamination. For as long as the sample remains inside the FIB chamber, long milling times favor the deposition of material on the lamella and increase its thickness. This is the reason why milling is done sequentially, first removing most of the material from all selected positions in the grid (rough milling) before milling down the lamellas to their final thickness (fine milling). Otherwise, the first positions to be fine-milled would spend more time in the chamber accumulating surface contamination.

Additionally, the presence of dense elements such as lipid droplets can cause irregular milling and yield a lamella of uneven thickness. To further complicate matters, the inherent Gaussian profile of the ion beam can cause areas outside of the defined milling region to be damaged, especially at high milling intensities. Coating the sample with a thin layer of organometallic platinum prior to the start of the procedure helps mitigate these issues, and recent advances in milling automation have the potential to improve the reproducibility and reliability of the technique (Schaffer et al. 2017).

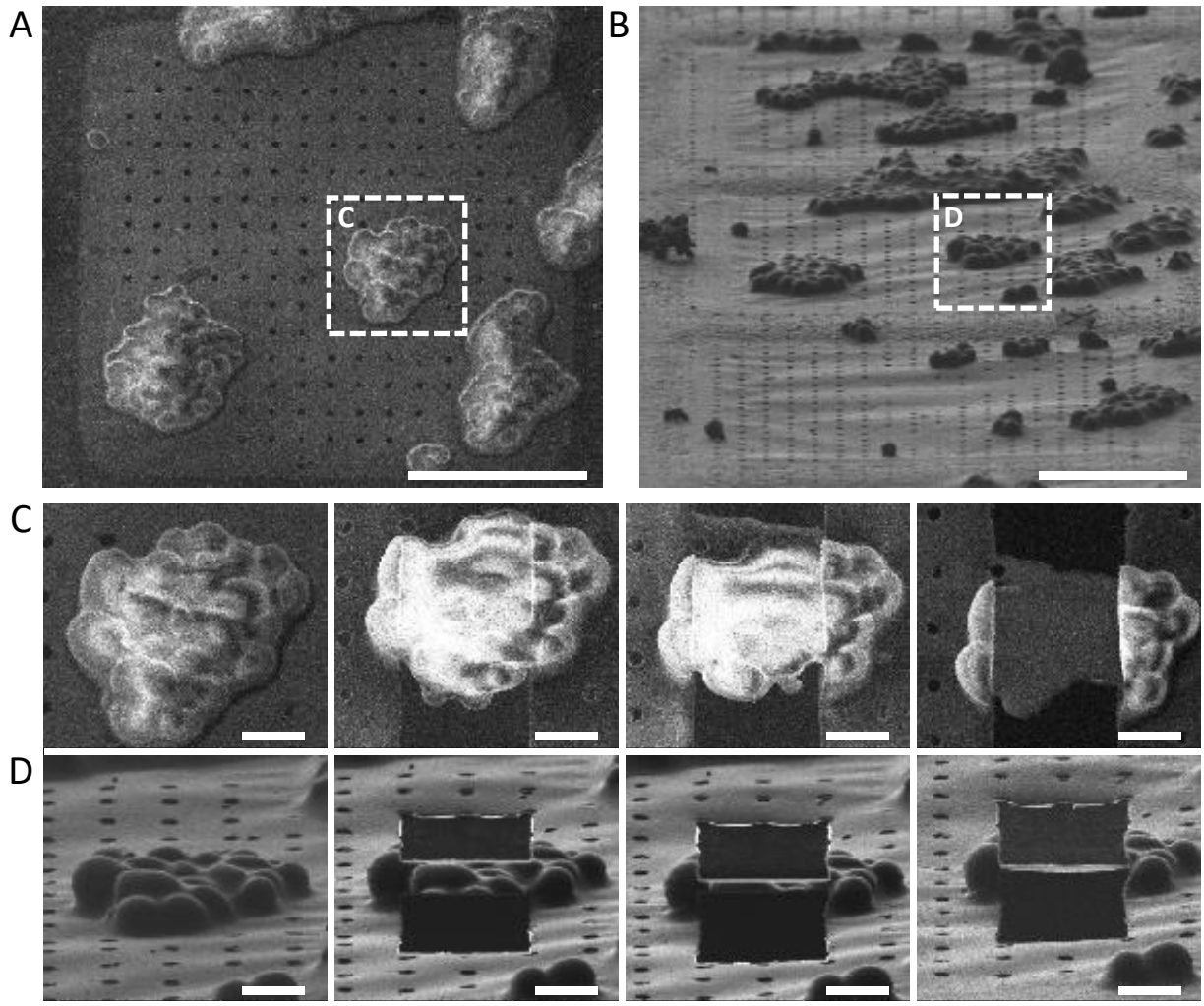

Figure 7. FIB milling.

(A-B) Grid square with yeast cell clusters in a plunge frozen Quantifoil® Cu R1/4 grid observed by SEM(A) and FIB (B) in a dual-beam Quanta 3D cryo-FIB. Insets: Cluster of cells chosen for lamella preparation.

(C-D) Milling progress on the yeast cluster (left to right) observed by SEM (C) and FIB (D). Lamella thickness progressed from unmilled (left) to 4µm (second from the left), 800nm (second from the right), and finally 200nm (right).

SEM images were acquired at beam settings 3kV and 10pA, FIB images were acquired at 30kV and 100pA.

Scale bars: (A-B) 30µm, (C-D) 5µm.

2.3.7 Reconstruction and interpretation

The reconstruction process begins by computationally aligning the multiple frames obtained for each tilt. This alignment can compensate for the image shifts and sample deformation caused by the electron beam, producing motion-corrected images (Zheng et al. 2017).

Once corrected, the different tilt images need to be aligned to a common reference system. In samples that do not require a thinning-down step as well as in chemically fixed samples, there is a possibility to add small gold beads to their surface to use as fiducials (Mastronarde 2006). The positions of these beads are tracked through the different tilts and manually refined to be used as reference to align the tilt images to each other. This approach is not possible with fibbed samples because once the sample is frozen, there is no current system that can reliably deposit fiducials on the surface at cryo-temperatures. Alternatively, introducing fiducials inside the cells in the sample in hopes that enough of them remain in the lamella after milling is pointless. Since most of the cell is milled away, the number of fiducials inside the cell required for this approach to work would be unrealistic.

Tilt series of fibbed samples are usually aligned using patch-tracking algorithms (Kremer et al. 1996; Mastronarde 1997). These split each tilt in smaller sections or "patches" and align each one with their corresponding patches across different tilts, effectively using them as fiducials.

After a tilt series has been aligned, reconstruction of the 3D volume can begin. Due to the limitations that come with the missing wedge in Cryo-ET, the most common method for reconstruction is weighted back-projection (WBP) (Radermacher 2006). The resulting tomogram can later be subjected to a variety of *in silico* manipulations.

Many of these manipulations are aimed at improving the visualization of the tomogram by increasing the SNR. These methods range from bandpass filters (Tegunov and Cramer 2020) and noise simulation algorithms (Fernández and Li 2003) to sophisticated deep-learning software (Buchholz et al. 2019; Bepler et al.). New advances can even digitally fill the missing wedge, minimizing the anisotropic distortions it causes (Liu et al., 2021).

Structural work related to cell membranes usually requires the membranes to be translated into 3D volumes, a process called segmentation. This task is greatly facilitated by the use of automatic segmentation algorithms (Martinez-Sanchez et al. 2014). Different programs can be used on these renderings to obtain morphological information (Salfer et al. 2020)or visualize membrane-bound molecular complexes (Wietrzynski et al. 2020).

3 Materials and methods

3.1 Materials

Table 3.1-1: Kits, consumables, and reagents.

Type	Name	Manufacturer	Reference
Reagent	Phusion® HF DNA Polymerase	NEB	Cat# M0530
Reagent	DpnI	NEB	Cat# R0176
Dye	Propidium Iodide	Invitrogen	Cat# P3566
Reagent Kit	QIAprep® Spin MiniPrep Kit	Qiagen	Cat# 27106
Consumable	Quantifoil grids 200 Mesh Copper R2/1	Quantifoil MicroTools	N/A
Consumable	Whatman Filter Paper 597	Sigma Aldrich	Cat# WHA10311814
Consumable	Cover Glasses	Carl Zeiss	Cat# 474030-9000-000
E. coli strain	Max Efficiency® DH5alpha	Invitrogen	Cat# 18258-012

Table 3.1-2: Software and algorithms.

Type	Name	Developer	Reference
Software	Amira	Thermo Fisher Scientific	https://www.fei.com/software/amira-3d-for-life-sciences/ RRID:SCR_014305
Software	BD FACSDiva	BD Biosciences	https://www.bdbiosciences.com/en-us RRID:SCR_001456
Software	Fiji/ImageJ	NIH	https://imagej.net/Fiji#Downloads RRID:SCR_002285
Software	Graph-Tool 2.2.44	Peixoto, 2017	https://graph-tool.skewed.de
Software	IMOD	Kremer et a.; 1996	http://bio3d.colorado.edu/imod/ RRID:SCR_003297
Software	K2Align	Dimitry Tegunov	https://github.com/dtegunov/k2align
Software	Mathematica 9.0	Wolfram Research, Inc.	https://www.wolfram.com/mathematica RRID:SCR_014448
Software	MATLAB	MathWorks	https://www.mathworks.com/ RRID:SCR_001622
Software	ParaView 5.5.2	Ahrens et al., 2005	https://www.paraview.org RRID:SCR_002516
Software	Pyto	Lučić et al., 2016	N/A
Software	Python 2.7.16 and 3.6.5	N/A	https://www.python.org RRID:SCR_008394
Software	Python 2.7 Packages Installed via Pip or Anaconda: matplotlib-1.5.1, networkx-1.11, nibabel-2.4.0,	N/A	https://pypi.org https://www.anaconda.com RRID:SCR_008624 RRID:SCR_002498 RRID:SCR_008633 RRID:SCR_008058

	numpy-1.11.3, skimage-0.12.3, scipy-0.18.1, pandas-0.19.2, pathlib2-2.2.0, pathos-0.2.2.1, pytest-4.6.2		
Software	Python 3 Packages Installed via Anaconda: matplotlib-3.0.2, numpy-1.15.2, pandas-0.23.0, scipy-1.1.0, seaborn-0.8.1, Statsmodels-0.9.0	N/A	https://www.anaconda.com RRID:SCR_016074
Software	Python Software to Estimate Membrane Curvature and Calculate Distances between Membranes	This study and Salfer et al., 2020	https://github.com/kalemaria/pycurv
Software	SerialEM	Mastronarde, 2005	http://bio3d.colorado.edu/SerialEM RRID:SCR_017293
Software	TOM Toolbox	Nickell et al., 2005	https://www.biochem.mpg.de/tom
Software	tom_deconv	Tegunov and Cramer, 2020	https://github.com/dtegunov/tom_deconv
Software	TomSegMemTV	Martinez-Sanchez et al., 2014	https://sites.google.com/site/3demimageprocessing/tomosegmemtv
Software	TOMOAND	Fernández and Li, 2003	https://sites.google.com/site/3demimageprocessing/tomoand
Software	VTK 6.3.0	Schroeder et al., 2006	http://www.vtk.org RRID: SCR_015013
Software	MODELLER 10.2	Webb et al., 2016	https://salilab.org/modeller/
Software	UCSF Chimera	Pettersen et al., 2004	https://www.cgl.ucsf.edu/chimera/
Software	Clustal Omega 1.2.4	Sievers et al., 2011	https://www.ebi.ac.uk/Tools/msa/clustalo/

3.1.1 Yeast strains and cell culture

All strains used in this study are listed in Table 3.1-3. The strains YCS2359 (*tcb3Δ*) and YCS2429 (*tcb1Δ tcb2Δ*) were introduced in this study. Both strains were created in the lab of Christopher J. Stefan (MRC Laboratory for Molecular Cell Biology, University College London). YCS2359 was created by chromosomal deletion of the TCB3 gene. YCS2429 was isolated as a

segregant of the genetic crossing of ANDY117 (*tcb1Δ*) and ANDY120 (*tcb2Δ*). Unless specified otherwise, all yeast strains were grown in YPD and incubated at 30°C until mid-log phase.

Table 3.1-3: Yeast strains.

Name	Reference	Identifier
SEY6210: *MAT**α** leu2-3,112 ura3-52 his3-Δ200 trp1-Δ901 lys2-801 suc2-Δ9*	Robinson et al., 1988	ATCC: 96099
SEY6210.1: *MAT**a** leu2-3,112 ura3-52 his3-Δ200 trp1 Δ901 lys2 801 suc2-Δ9*	Robinson et al., 1988	SEY6210.1
ANDY117: SEY6210 *tcb1*Δ::KANMX6	Manford et al., 2012	ANDY117
ANDY118: SEY6210.1 *tcb1*Δ::*KANMX6*	Manford et al., 2012	ANDY118
ANDY120: SEY6210.1 *tcb2*Δ::KANMX6	Manford et al., 2012	ANDY120
YCS2359: SEY6210.1 *tcb3*Δ::HISMX6	This study	YCS2359
YCS2430: SEY6210.1 *tcb1*Δ::KANMX6 *tcb2*Δ::KANMX6	This study	YCS2429
ANDY214: SEY6210.1 *tcb1*Δ::KANMX6 *tcb2*Δ::KANMX6 *tcb3*Δ::HISMX6	Manford et al., 2012	ANDY214
DBY356: SEY6210.1 *scs2*Δ::*TRP1 scs22*Δ::*HISMX6*	Stefan et al., 2011	DBY356
ANDY113 SEY6210.1 *ist2*Δ::*HISMX6*	Manford et al., 2012	ANDY113
ANDY129: SEY6210.1 *ist2*Δ::HISMX6 *scs2*Δ::TRP1 *scs22*Δ::HISMX6	Manford et al., 2012	ANDY129
ANDY176: SEY6210.1 *ist2*Δ::HISMX6 *tcb1*Δ::KANMX6 *tcb2*Δ::KANMX6 *tcb3*Δ::HISMX6	Manford et al., 2012	ANDY176
ANDY196: SEY6210.1 *scs2*Δ::TRP1 *scs22*Δ::HISMX6 *tcb1*Δ::KANMX6 *tcb2*Δ::KANMX6 *tcb3*Δ::HISMX6	Manford et al., 2012	ANDY196
ANDY198: SEY6210.1 *ist2*Δ::HISMX6 *scs2*Δ::TRP1 *scs22*Δ::HISMX6 *tcb1*Δ::KANMX6 *tcb2*Δ::KANMX6 *tcb3*Δ::HISMX6	Manford et al., 2012	ANDY198

3.1.2 Plasmids and oligonucleotides

The constructs used in this study are listed in Table 3.1-4. Plasmid construction was performed by Dr. Clélia Bourgoint (University of Geneva).

The plasmid pCB2 containing a version of TCB3 that lacked the SMP domain (272-479 aa deletion) was created from the vector pAM43 (Manford et al. 2012). pAM43 was linearized using Phusion® HF DNA polymerase (NEB) with custom made oligos 5′-AAGAAACCTTGTCGGATCGCGACATTATGGCTGCTCAATCAAAAGAAG - 3′ and 5′-GCGATCCGACAAGGTTTCTT -3′ (metabion). The PCR product was later treated with restriction enzyme DpnI (NEB) and further purified with phenol-chloroform before being recircularized with

Gibson Assembly (Gibson et al. 2009). The reaction was cloned in Max Efficiency® DH5alpha (Invitrogen) and plated in LB-Ampicillin (100µg/mL) for selection. The plasmid was extracted from the DH5alpha cells using the QIAprep® Spin Miniprep Kit (Qiagen). Sequence confirmation was performed by Microsynth using the oligo 5′- ATGACTGGCATCAAAGCTCAAGT- 3′ (metabion) as the template. pCB2was transformed into the corresponding yeast strains using the LiAc-SS-PEG method. Transformed cells were grown in synthetic medium with 2% glucose and pH 6.25 PBS buffer and lacking leucine for selection.

Table 3.1-4: Plasmids and oligonucleotides.

Type	Name	Manufacturer	Reference
Plasmid	pRS415-TCB3-GFP-TADH1	Manford et al., 2012	pAM43
Plasmid	pRS415-Tcb3 (1–491)-GFP-TADH1	Manford et al., 2012	pAM44
Plasmid	pRS415-TCB3 SMPΔ-GFP-TADH1	This study	pCB2
Oligonucleotide	Fwd deltaTCB3_SMP: AAGAAACCTTGTCG GATCGCGACATTATGGCTGCTCAA TCAAAAGAAG	metabion	Custom
Oligonucleotide	Rv deltaTCB3_SMP: GCGATCCGACAAGGTTTCTT	metabion	Custom
Oligonucleotide	Fwd TCB3-1: ATGACTGGCATCAAAGCTCAAGT	metabion	Custom

3.2 Methods

3.2.1 PM Integrity Assays

PM integrity assays were performed in the lab of Christopher J. Stefan by Ffion Thomas (MRC Laboratory for Molecular Cell Biology, University College London)

Cells were grown at 26°C in YPD or selective drop out medium (YNP) in the case of plasmid-containing strains until mid-log phase. Afterwards, volumes containing a number of cells equivalent to 1 OD_{600} were collected and transferred to a water bath at 42°C without exchanging the medium. After 10 min incubation the cells were centrifuged and resuspended in PBS. Propidium iodide was added to a final concentration of 1 µg/mL for an incubation period of 10 min. Cells were washed twice in ddH2O before analysis by flow-cytometry (BD LSR II). The background was determined by measuring the cells prior to staining. Four independent biological replicates were done per condition, and each measurement counted 10.000 cells.

3.2.2 Light microscopy

Cells were grown overnight in the corresponding culture medium. After being diluted the next day, they were allowed to grow into the exponential phase (OD_{600} = 0.6 - 0.8). After being briefly centrifuged to increase the concentration of the culture they were imaged at a LSM780 microscope (Zeiss) with a 63x magnification oil objective and Z-stacks were acquired. Image processing was done with Fiji software (NIH).

3.2.3 Cryo-electron microscopy

3.2.3.1 Cell vitrification

Cryo-EM grids (R2/1, Cu 200 mesh grid, Quantifoil microtools) were glow discharged using a plasma cleaner (PDC-3XG, Harrick) for 30 seconds on the "high" setting before being mounted on a Vitrobot Mark IV (FEI). A 3.5 µl droplet of exponential phase yeast culture (OD600 = 0.6 - 0.8) was pipetted onto the carbon side of the grid. Afterwards, the grid was blotted from the back with filter paper (Whattman 597) to remove excess medium. The blotting force was set at 9 for a duration of 10 seconds before plunging the grid into liquid ethane/propane mixture cooled by liquid nitrogen. Adequate blotting conditions produce grids with enough ice to give yeast cell groups a sloped border while leaving most holes in the carbon film empty (Figure 7). The grids were stored in grid boxes submerged in liquid nitrogen until required.

3.2.3.2 Cryo-focused ion beam milling

The grids were secured to Autogrid carriers (FEI) under liquid nitrogen with a C-ring. They were then mounted on a transfer shuttle and inserted in a dual-beam Quanta 3D cryo-FIB / scanning electron microscope (SEM) (FEI) using a cryo-transfer system (PP3000T, Quorum) to keep the sample under vacuum during transfer. After insertion, the cryo-stage keeps the temperature of the sample at -180°C.

The quality of the grid was assessed by checking for an even distribution of cells across the grid and the presence of cell clusters roughly centered on the grid squares (Figure 7A, 7B). If the quality of the sample was satisfactory, the grid was coated with a layer of organometallic

platinum using a gas injection system for 9 seconds to protect it from indirect ion beam damage. Suitable milling positions were chosen where small clusters of cells presented a thin ice coating and were close to the center of a grid square with unbroken carbon film. The milling angle was 20° and the selected width of the lamellas was around 14 µm.

The milling was done sequentially, first milling all selected positions to a final thickness of 800 nm with the Ga^{2+} ion beam at 30 kV and 500 pA beam current at the beginning and lowering it to 30 kV and 50 pA at the end. These rough-milled lamellas were then further thinned down to ~200 nm with the beam at 30 kV and 30 pA. The final thickness was considered adequate for tomography when the lamella lacked charging under the SEM at 3 kV and 10 pA (Figure 7D right), which roughly translated to a thickness of less than 250 nm.

3.2.3.3 Cryo-electron tomography

Lamellas were imaged in a Titan Krios microscope (FEI) with the exception of *tcb3Δ* + Tcb3 SMPΔ-GFP, *tcb3Δ* + Tcb3 C2Δ-GFP, *tcb3Δ* + Tcb3-GFP cells, and one experiment of *tcb1/2/3Δ*, *tcb3Δ* and *tcb1Δ* cells, which were imaged in a Polara microscope (FEI). Both microscopes were equipped with 300 kV field emission guns and K2 Summit direct electron detectors (Gatan) as well as post-column energy filters (Gatan).

The regions of interest were identified in low magnification, high defocus images of the lamella (4500 ×, 27 Å pixel size in Polara; 3600 ×, 40 Å pixel size in Titan Krios; -100 µm defocus). Tilt-series were acquired at these positions using SerialEM software (Mastronarde 2005) at high magnification and low defocus (34,000 ×, 3.509-Å pixel size in Polara except for one experiment of the *tcb1/2/3Δ*, *tcb3Δ* and *tcb1Δ* conditions where settings were 22,500 x 5.22-Å pixel size; 42,000 ×, 3.42-Å pixel size in Titan Krios; -5 µm defocus). For tilt series acquired in Titan Krios for the *tcb1/2/3Δ*, *Δtether*, WT heat shock and *tcb1/2/3Δ* heat shock conditions the acquisition scheme was dose symmetric, while for all other tilt series acquired it was unidirectional. In both cases the tilt range was from 60° to -46 ° with 2° intervals between images. The camera acquisition was set to dose-fractionation mode with frames being acquired every 0.2 seconds. The 1/cos scheme for dose adjustment was used to increase the dose at high tilts, resulting in exposure times of 1 to 2 seconds per tilt image depending on the angle. In total, the dose for each series was ~120 e-/Å2.

3.2.3.4 Tomogram reconstruction and post-processing

The alignment of the subframes composing each tilt image was done with the software K2Align (Li et al. 2013). Afterwards, the tilt images were aligned to each other using a patch-tracking algorithm and reconstructed as a tomogram using weighted back-projection in the software IMOD (Kremer et al. 1996).

The tomograms were binned to a final voxel size of ~2.1 nm for tomograms acquired at 22,500x magnification and ~1.4 nm for all others. A deconvolution filter (Tegunov and Cramer 2020) was used to improve contrast of the membranes in the tomograms and executed in Matlab (MathWorks) using the functionality of the TOM Toolbox (Nickell et al. 2005). Additionally, a different anisotropic denoising filter (TOMOAND) was used where specified on some figures to improve visualization (Fernández and Li 2003).

3.2.4 Membrane morphology analysis

Membrane curvature, intermembrane distance measurements, and cER peak morphological characterization were performed with the help of Maria Salfer with the assistance of Dr. Antonio Martínez-Sánchez (Department of Molecular Structural Biology, Max Planck Institute of Biochemistry).

3.2.4.1 Membrane segmentation and surface generation

Membranes were automatically segmented using the algorithm TomoSegMemTV (Martinez-Sanchez et al. 2014) and refined to compensate for noise and missing wedge-derived aberrations using the software Amira (FEI). The membranes of different organelles were assigned to different materials as well as the ER lumen and the inter-organellar space, which were manually segmented.

Segmentations composed of voxels had to be converted to smooth surfaces prior to any morphological analysis to ensure accuracy. Firstly, they were smoothed using a Gaussian kernel with a σ of 1 voxel, and isosurfaces were generated from them using the Marching Cubes algorithm (Newman and Yi 2006) with a 0.7 isosurface level. Afterwards, a triangle-mesh surface delimiting

the isosurface was generated and all analysis were conducted on it. Surface triangles had an average area of 0.6 ± 0. 4 nm^2 (mean ± SD) for the PM and 0.7 ± 0. 4 nm^2 (mean ± SD) for the cER membrane.

3.2.4.2 Membrane curvature analysis

The PyCurv algorithm described in Salfer et al. was used to estimate the local curvatures in the surface. The neighboring triangles of any given triangle up and until a certain radius are used to denoise the normal vector of said triangle using tensor voting. Both the maximal (κ1) and minimal (κ2) principal curvatures (Figure 8A) are combined in a single scalar value that defines the curvedness (Eq. 2) (Koenderink and van Doorn 1992). The partial neighborhood of triangles at the edge of the membrane surface causes their values to be poorly calculated, and they are hence removed from the analysis. The visualization of curvatures was done in software Paraview (Ahrens et al. 2005).

$$Curvedness = \frac{\sqrt{\kappa 1^2 + \kappa 2^2}}{2} \qquad Eq.(2)$$

The range of triangles in the geodesic neighborhood used to denoise the normal vectors is defined by the maximum geodesic distance g_{max}, which depends on a radius_hit (rh) value according to Eq. 3.

$$g_{max} = \frac{\pi \cdot rh}{2} \qquad Eq.(3)$$

For our analysis it was decided to use a *rh* value of 10 nm, which was sufficiently small to measure the curvature at the cER regions of high curvature while at the same time limiting the noise on the membrane surface. Table 3.2-1 contains the number of triangles in the cER surfaces for each condition.

3.2.4.3 Intermembrane distance measurements

The interorganellar distance for all conditions was defined as the distance between the organelle leaflets that face each other at the MCS, and organelle thickness was defined as the distance between the luminal leaflets of the target organelle.

The distances between the cER and the PM and between the leaflets of the cER were obtained from the same surfaces described in the curvature determination section. Due to the triangular mesh surface generating along the middle line of the membrane segmentation, an offset of 1 voxel was employed to account for the added thickness of a lipidic leaflet in all measurements.

Denoised normal vectors emanating from the geodesic center of every triangle in the PM surface traversed the ER-PM interorganellar space for up to 50 nm until encountering the surface of the cER. The Euclidean distance of the vectors that connected to the cER surface are registered as inter-organellar distances (Figure 8B). The PM was chosen as the starting surface due to its surface being more homogenous than the cER, which is the same factor that decided the starting surface in other MCS measurements (mitochondria in ER-Mitochondria contacts, and vacuole in nucleus-vacuole contacts). Table 3.2-1 contains the distance measurements for each condition.

The denoised normal vectors from the starting surface continued up to another 80 nm or until they intersect the second surface a second time (Figure 8B). The Euclidian distance difference between the first and second intersection of the target surface is registered as thickness. Table 3.2-1 contains the thickness measurements for each condition.

3.2.4.4 cER peak morphology and quantification

The maximum cER peak height and width, as well as the minimum distance to the PM were measured for each peak directly on tomographic slices using IMODs in-built measuring tool. The number of peaks was counted manually for each condition, and peak density was defined as the ratio between the number of peaks and half the cER surface area to consider only the cER contact surface. The cER surface area was defined as the sum of all triangle surfaces in the cER mesh and can be found in Table 3.2-1 for each condition.

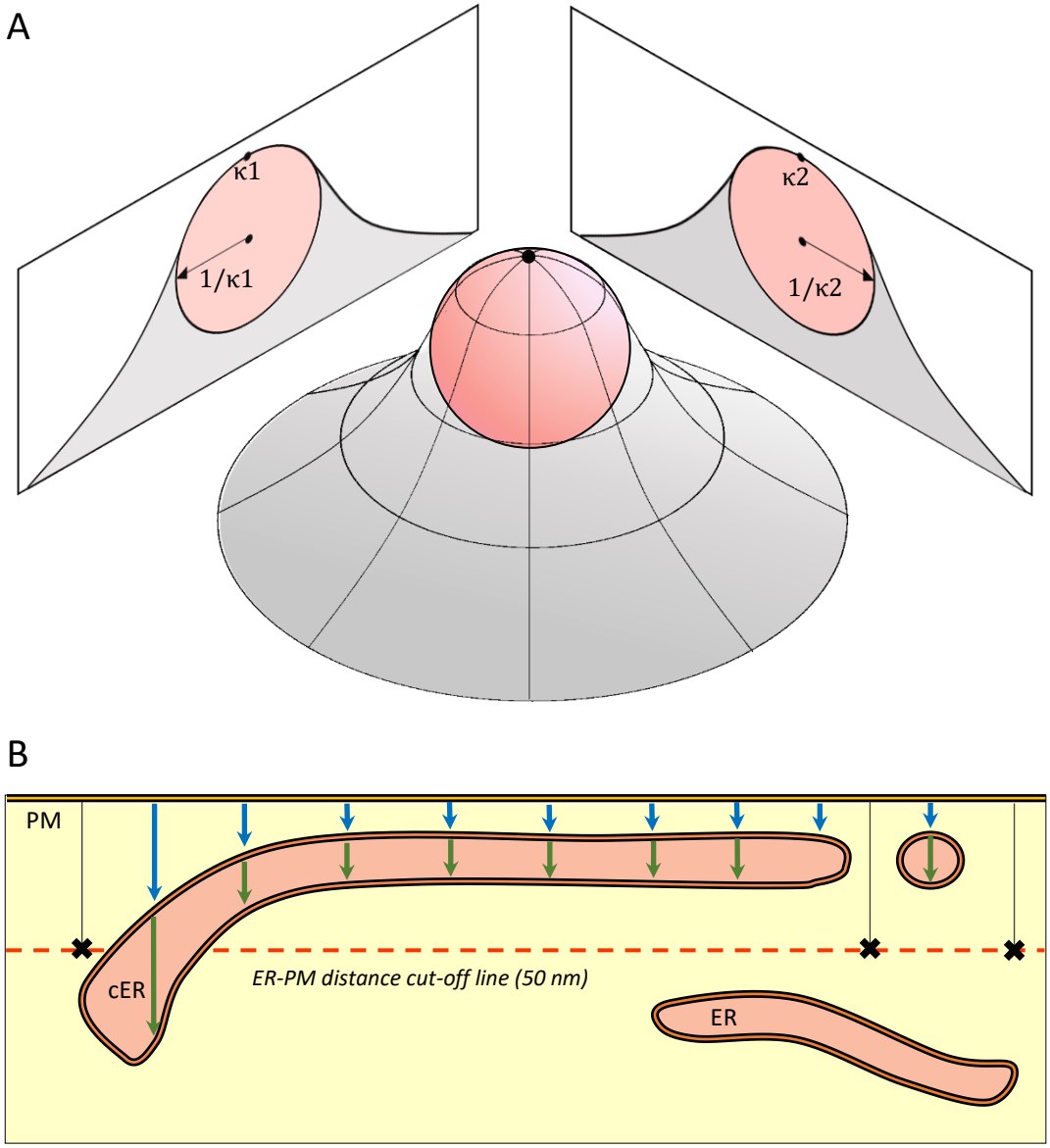

Figure 8. Membrane geometry.

(A) Principal curvatures of a membrane peak with local spherical curvature at the tip, with the two principal curvatures (κ1, κ2) and their relation to curvature radius represented on 2D projections of the peak.

(B) Distance measuring algorithm. Arrows represent normal vectors emanating from the PM (blue), those continuing until intersecting the cER a second time (green), and those that fail to find the cER before the set distance of 50 nm (black cross-heed). ER: endoplasmic reticulum; cER: cortical ER; PM: plasma membrane.

Table 3.2-1: Membrane analysis statistics.

Condition	Number of biological replicates	Number of MCSs	Intermembrane distance measurements	cER thickness measurements	cER curvature measurements	Total cER area analyzed (μm^2)
WT	2	6	685,160	531,487	2,612,817	1.7
WT HS	2	7	-	-	-	1.7
Ist2-only	2	5	663,763	525,115	2,327,393	1.5
Scs2/22-only	2	5	478,590	388,246	1,824,833	1.1
Tcb1/2/3-only	3	9	552,956	368,510	2,053,182	1.3
Δtether	1	4	-	-	-	0.16
*tcb1*Δ	2	5	-	-	-	0.9
*tcb2*Δ	2	5	-	-	-	0.7
*tcb3*Δ	2	5	-	-	-	0.8
*tcb1/2*Δ	2	5	-	-	-	0.8
*tcb1/2/3*Δ	2	5	-	-	-	1.4
*tcb1/2/3*Δ HS	2	5	-	-	-	0.7
*tcb3*Δ + Tcb3-GFP HS	2	3	-	-	-	0.3
*tcb3*Δ + Tcb3-SMPΔ-GFP HS	2	3	-	-	-	0.4
tcb3Δ + Tcb3-C2Δ-GFP HS	2	3	-	-	-	0.4
ER-Mito	3	5	81,124	-	-	0.09
Nuc-Vac	2	5	362,899	-	-	0.35

3.2.5 Lipid extraction modeling

The mathematical modeling of lipid membranes and the calculation of lipid extraction energies were performed by Dr. Felix Campelo (Barcelona Institute of Science and Technology) at the Institut de Ciencies Fotoniques (ICFO).

3.2.6 Sequence homology modelling

Structure predictions of C2 domains were done using MODELLER. Three previously known structures were used to create a template, namely the C2A domain of plant Syt1 (PDB ID: 7atp), C2A and C2B of mammalian E-Syt2 (PDB ID: 4npk), and C2A of rat otoferlin (PDB ID: 3l9b).

UCSF Chimera was used to visualize the generated models and perform Coulombic coloring of the surfaces. The settings for the electrostatic calculations and coloring were left as default.

3.2.7 Statistical analysis

Individual distance measurements cannot be compared to each other because they are not independent after normal vector denoising, therefore we specify N as the number of MCSs analyzed instead. Normality was determined by Shapiro-Wilks test, and significance was calculated using t-test for normally distributed data and Mann-Whitney-U test for non-normal data.

The distances and curvatures obtained by applying the PyCurv algorithm are shown as violin plots (Figures 10E, 13A, and 13B) or histograms (Figure 15E).

For violin plots, the complete distribution of values is shown. The white dot represents the median, the black slab represents the interquartile range, and the thin black line 1.5x the interquartile range.

For the histogram in Figure 15E, the frequency of curvature values for each condition was weighted by their triangles' surface relative to the total surface area. The relative frequency of exceedance for these values (defined as 1 - cumulative relative frequency) is plotted for each bin (black line) ± SE (shaded area) with the width of each bin being 1 nm^{-1}.

Peak quantifications (Figures 14B, 18A, and 21E) are shown as mean peak density per μm^2 cER surface area for each condition ± SE. cER peak morphology measurements (Figure 9A) were displayed in a box plot.

For PM integrity assays (Figures 17A, 17B, and 21D), bar plots were used to show mean values for each condition ± SE. The average values from four independent experiments were analyzed.

4 Results

4.1 MCS architecture in *S. cerevisiae*

Cryo-ET is a technique that preserves cellular structures in a frozen-hydrated state (Dubochet et al. 1988). MCSs are delicate structures and maintaining them in close-to-native conditions is crucial for their study (Fernández-Busnadiego et al. 2015; Collado and Fernández-Busnadiego 2017). In addition, tomograms taken in intact cells provide a lot of information about the environment of the feature of interest and help put any observation in its biological context.

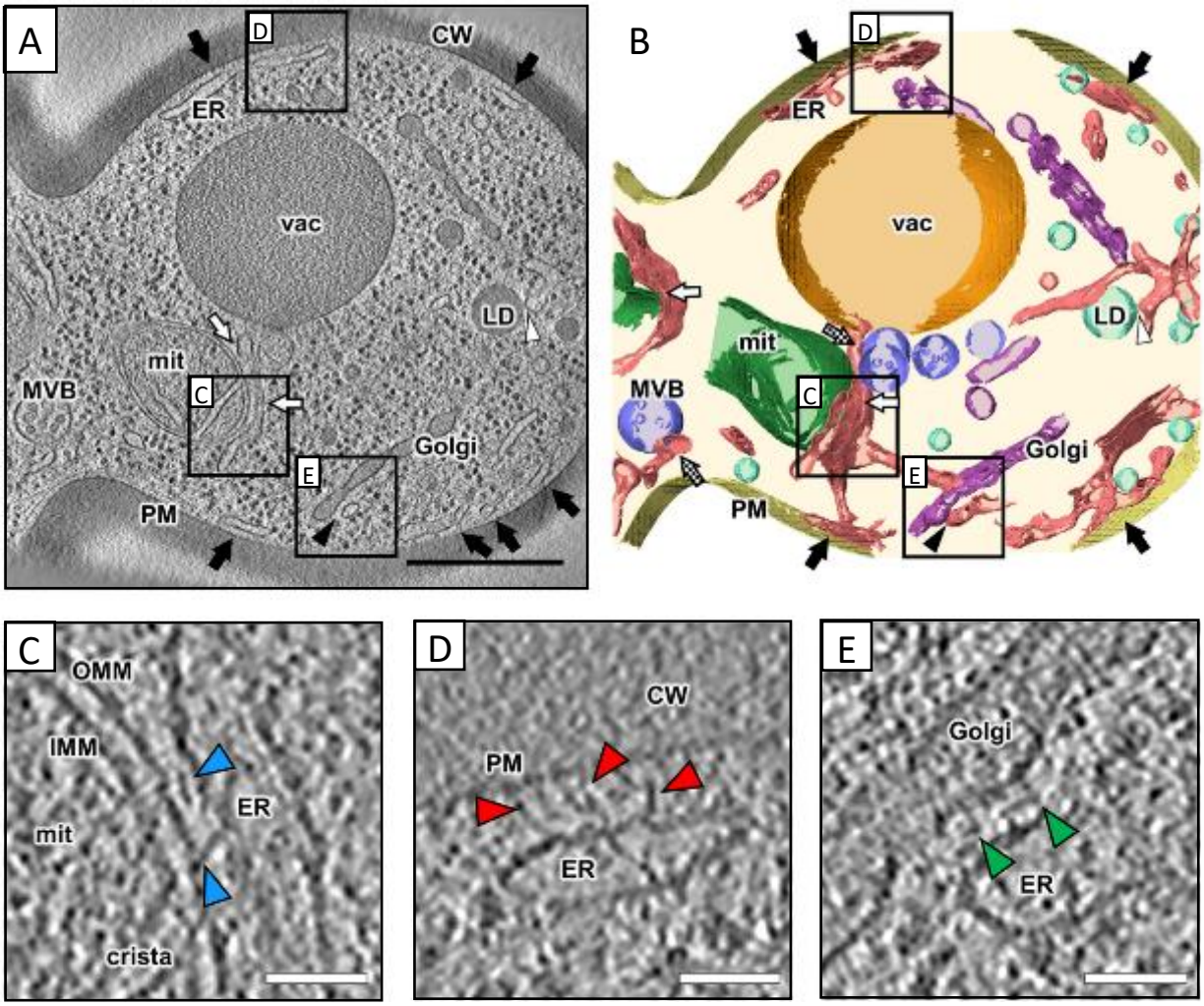

Figure 9. Graphical overview of MCSs.

(A) 2.0 nm-thick tomographic slice of a vitrified yeast bud. The boxed areas in (A) are magnified in (C-E). CW: cell wall, PM: plasma membrane, ER: endoplasmic reticulum, mit: mitochondrion, Golgi: Golgi apparatus, LD: lipid droplet , MVB: multivesicular body, vac: vacuole. Different arrows indicate different MCSs; ER-PM (black arrows), ER-mitochondria (white arrows), ER-Golgi (black arrowhead), ER-lipid droplet (white arrowhead).

(B) Three-dimensional reconstruction of the membranes in the tomogram shown in (A). The boxed areas correspond to the positions of (C-E). ER-MVB MCSs are marked by checkered arrows. Different colors are used to represent different organelles; ER (pink), Golgi (purple), lipid droplets (light green), mitochondria (dark green), MVBs (blue), plasma membrane (gold), vacuole (orange).

(C–E) Magnifications of the boxed areas in (A-B). Arrowheads: electron-dense intermembrane tethers in ER-mitochondria MCS (C; blue), ER-plasma membrane MCS (D; red), and ER-Golgi apparatus MCS (E; green). IMM: inner mitochondrial membrane, OMM: outer mitochondrial membrane.

Scale bars: 500 nm (A, B), 50 nm (C - E).

All images in Figure 9 are sourced from Collado et. al. 2017 with permission from Elsevier.

Tomograms of *S. cerevisiae* revealed the complex network of MCSs inside the cell (Figure9). As expected from previous observations (Loewen et al. 2007; Manford et al. 2012; Toulmay and Prinz 2012; Wolf et al. 2012), the most abundant were ER-PM contacts (Figure 10A,C), where the cER coats large areas of the PM. Nucleus-vacuole junctions were easily found in tomograms due to their great extension and were arguably the second most abundant contact in yeast (Figure 10B,D). Contacts between the ER and mitochondria were also ubiquitous (Figure 10A,C) and could often be seen at places of mitochondrial fission (Steffen and Koehler 2018). Other MCSs less frequently observed in tomograms include contacts between the vacuole and multivesicular bodies (MVB) (Figure 10B) involved in endocytosis, ER and Golgi apparatus (Figure 9E), lipid droplets and the ER, along with many others that will not be listed for being beyond the scope of this work.

These MCSs can extend for hundreds of square nanometers, even square micrometers in the case of cER-PM contacts. Despite being a low-throughput technique, cryo-ET of FIB-milled specimens yields high magnification and high-resolution data of these extensive areas. The vast amount of data points on the topology of the contacts allows us to use quantitative methods to study their architecture. Additionally, the abundance of these contacts makes the use of cryo-light correlation unnecessary, saving time and protecting the sample from contamination due to additional handling.

We used the method detailed in Salfer et al. to obtain the distributions of intermembrane distances of different MCSs. The quantitative analysis of the intermembrane distance at ER-PM, ER-mitochondria, and nucleus-vacuole contacts revealed the existence of different distance profiles that appeared to be signature of the organelles involved. The nucleus-vacuole average

distance was 21 ± 7 nm (mean ± STD, N = 5 nucleus-vacuole MCS; Figure 10E), while ER-Mitochondria distances were significantly shorter (16 ± 7 nm; mean ± STD, N = 5 ER-mitochondria MCS; $p < 0.05$ by unpaired t test; Figure 10E). cER-PM contacts were also wider than ER-mitochondria MCS (23 ± 5 nm; mean ± STD, N=6 cER-plasma membrane MCS; $p < 0.05$ by unpaired t test; Figure 10E), which proves that the same organelle, the ER in this case, can participate in various morphologically different contacts.

Distance between membranes is a defining feature of MCSs that depends on many factors, but primarily on the tether protein populations present at the site, which can be seen as electron dense linkers in the tomograms (Figure 9C-E, 10C, 10D). Therefore, the analysis of membrane distances at the MCS using quantitative methods reveals information about the tethers that contribute to them.

The contacts we focused on where those between cER and PM. Compared to others, they display the greatest morphological complexity.

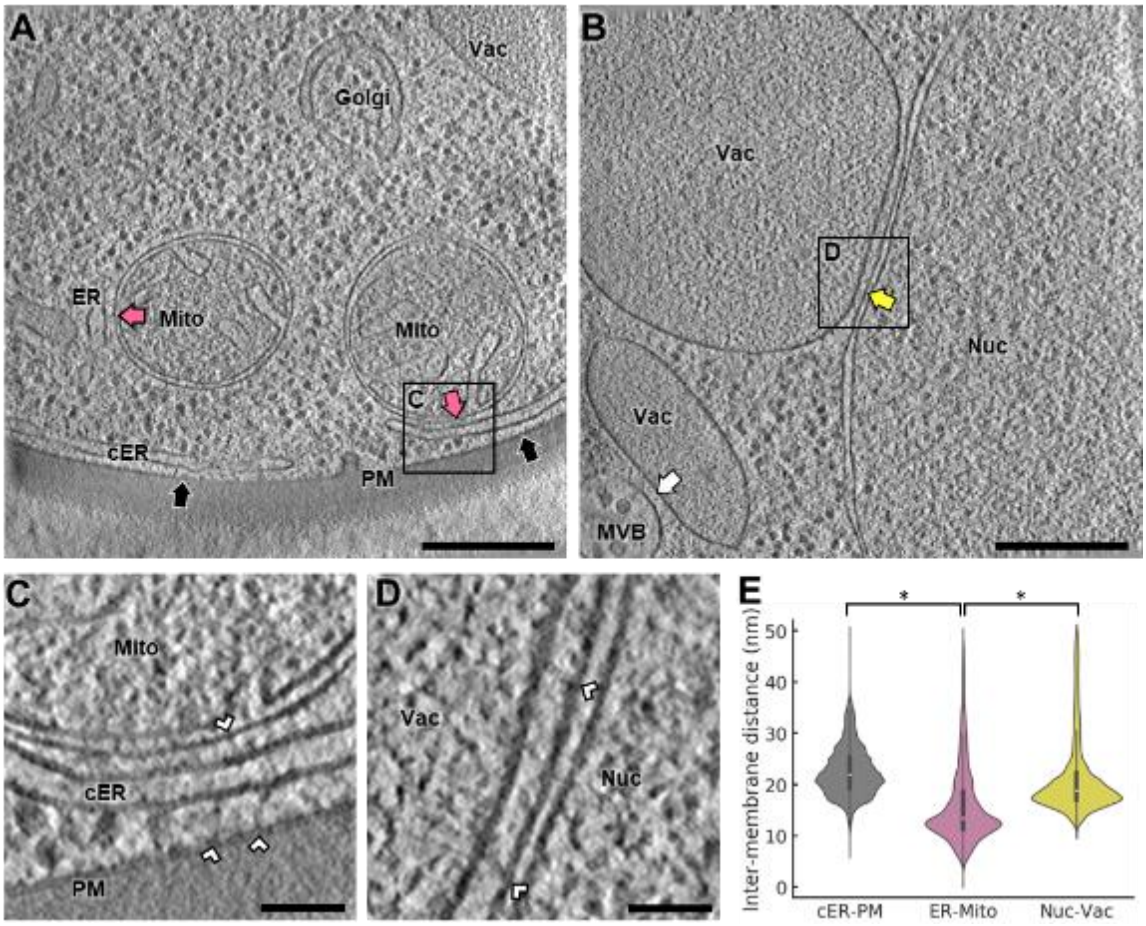

Figure 10. Cryo-ET Imaging of MCS in WT *S. cerevisiae*.

(A) 1.4 nm-thick tomographic slice showing cER-PM MCS (black arrows) and ER-mitochondria MCS (purple arrows). The boxed area is magnified in (C). ER: endoplasmic reticulum; cER: cortical ER; Golgi: Golgi apparatus; Mito: mitochondrion; PM: plasma membrane; Vac: vacuole.

(B) 1.4 nm-thick tomographic slice showing a nucleus-vacuole junction (yellow arrow) and a multivesicular body-vacuole MCS (white arrow). The boxed area is magnified in (D). MVB: multivesicular body; Nuc: nucleus.

(C) Magnification of the boxed area in (A). White arrowheads: electron-dense intermembrane tethers.

(D) Magnification of the boxed area in (B). White arrowheads: electron-dense intermembrane tethers.

(E) Violin plots showing the distribution of intermembrane distances of cER-PM, ER-mitochondrion, and nucleus-vacuole MCS. The plots show the complete distribution of values including all MCS analyzed. A white dot represents the median, a black slab the interquartile range, and a black line 1.5x the interquartile range. * indicates $p < 0.05$ by unpaired t test. N = 6 (cER-PM), 5 (ER-mitochondria) and 5 (nucleus-vacuole) MCS in WT cells.

Scale bars: 300 nm (A, B), 50 nm (C, D).

4.2 cER-PM morphology is affected by tethers

The most important contribution of tether proteins to cER-PM MCS morphology is controlling the amount of cER itself, which is tightly regulated by the cell through the Environmental Stress Response, High Osmolarity Glycerol, and Unfolded Protein Response stress pathways (Quon et al. 2018). The cER is partially visible in low magnification lamellae micrographs in the TEM and we took this opportunity to approximate the amount of cER across strains lacking specific cER-PM tethers.

Wild type (WT) yeast presented the largest contacts (Figure 11A), followed by the strains expressing only Ist2 (scs2/22Δ tcb1/2/3Δ) (Figure 2B) or Scs2/22 (ist2Δ tcb1/2/3Δ) (Figure 11C). Cells expressing only Tcb1/2/3 (ist2Δ scs2/22Δ) (Figure 11D) showed remarkably fewer contacts compared to the other strains, only surpassed by the virtually contact-less phenotype of the Δtether strain (Figure 11E). These results agree with previous, more exhaustive observations (Manford et al. 2012) and support the notion that tricalbins are an inefficient tether when compared to Ist2 and Scs2/22 and might have a different, undiscovered primary function.

Apart from the differences in cER abundance, there was little information about the individual contributions of these tether proteins to cER-PM contacts, their involvement in cER morphology, and their function. The next step of this study was therefore to determine the influence of each tether family on cER morphology.

To this end, the membranes of cER and PM at cER-PM contacts in our tomograms were rendered as 3D volumes, from which quantitative data about cER-PM distance, cER thickness, and cER membrane curvature could be obtained. Qualitative observation of these 3D volumes revealed morphological differences between the strains. We found that the cER in WT yeast (Figure 12A) is a meshwork of sheets and tubules, a diverse landscape of membrane topologies seemingly morphing into one another. cER in Ist2-only strain (Figure 12B) appeared to be qualitatively very similar to WT, while the greatest differences came from the extended sheets of Scs2/22-only cER (Figure 12C) and the highly tubular Tcb1/2/3-only cER (Figure 12D) (detailed in section 4.2.1).

The next step of our research was to use the method detailed in Salfer et al. to obtain the distributions of intermembrane distances at the contacts, luminal distances for the cER, and cER membrane curvature. Taken together, these measurements would allow us to describe cER morphology.

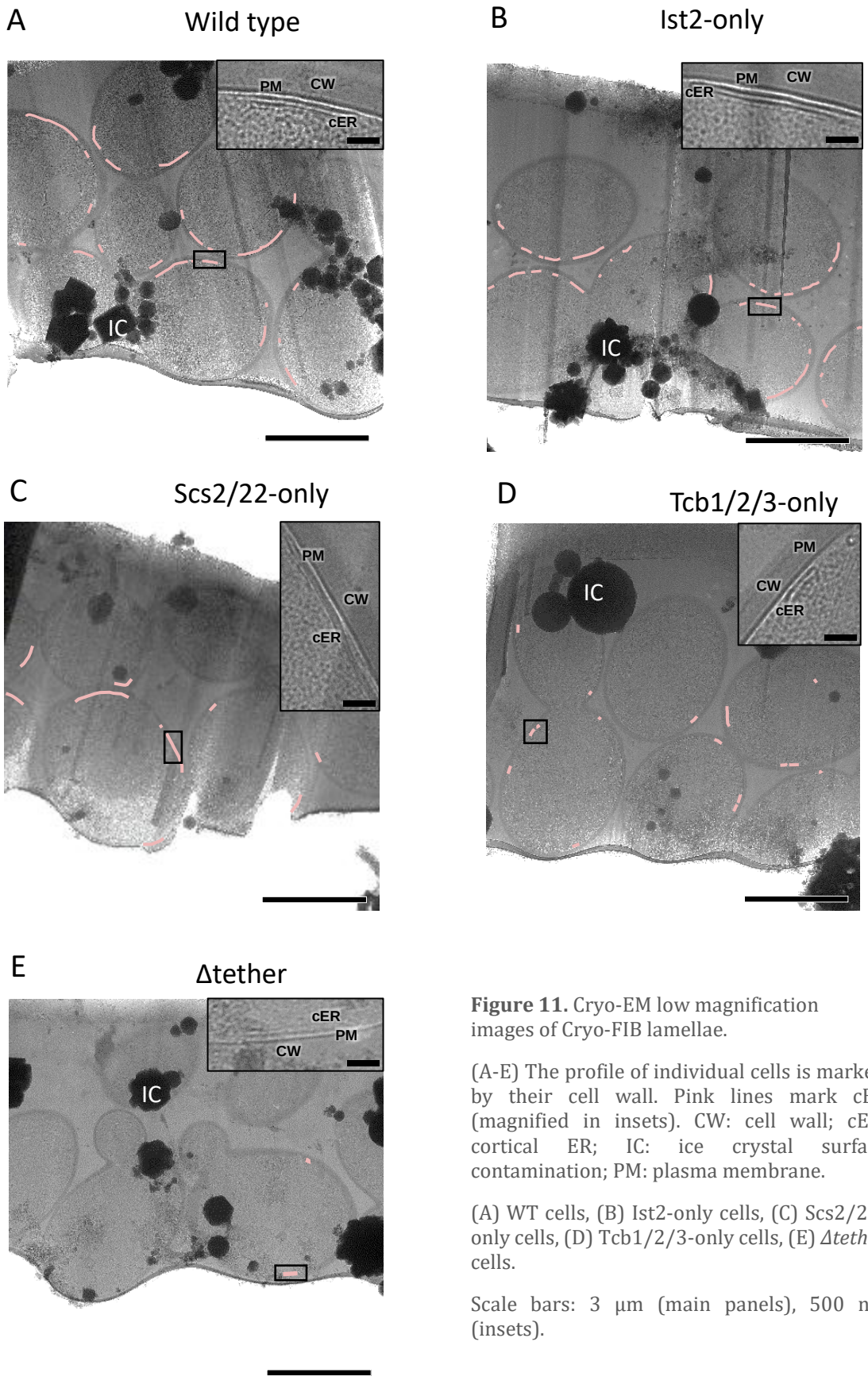

Figure 11. Cryo-EM low magnification images of Cryo-FIB lamellae.

(A-E) The profile of individual cells is marked by their cell wall. Pink lines mark cER (magnified in insets). CW: cell wall; cER: cortical ER; IC: ice crystal surface contamination; PM: plasma membrane.

(A) WT cells, (B) Ist2-only cells, (C) Scs2/22-only cells, (D) Tcb1/2/3-only cells, (E) *Δtether* cells.

Scale bars: 3 µm (main panels), 500 nm (insets).

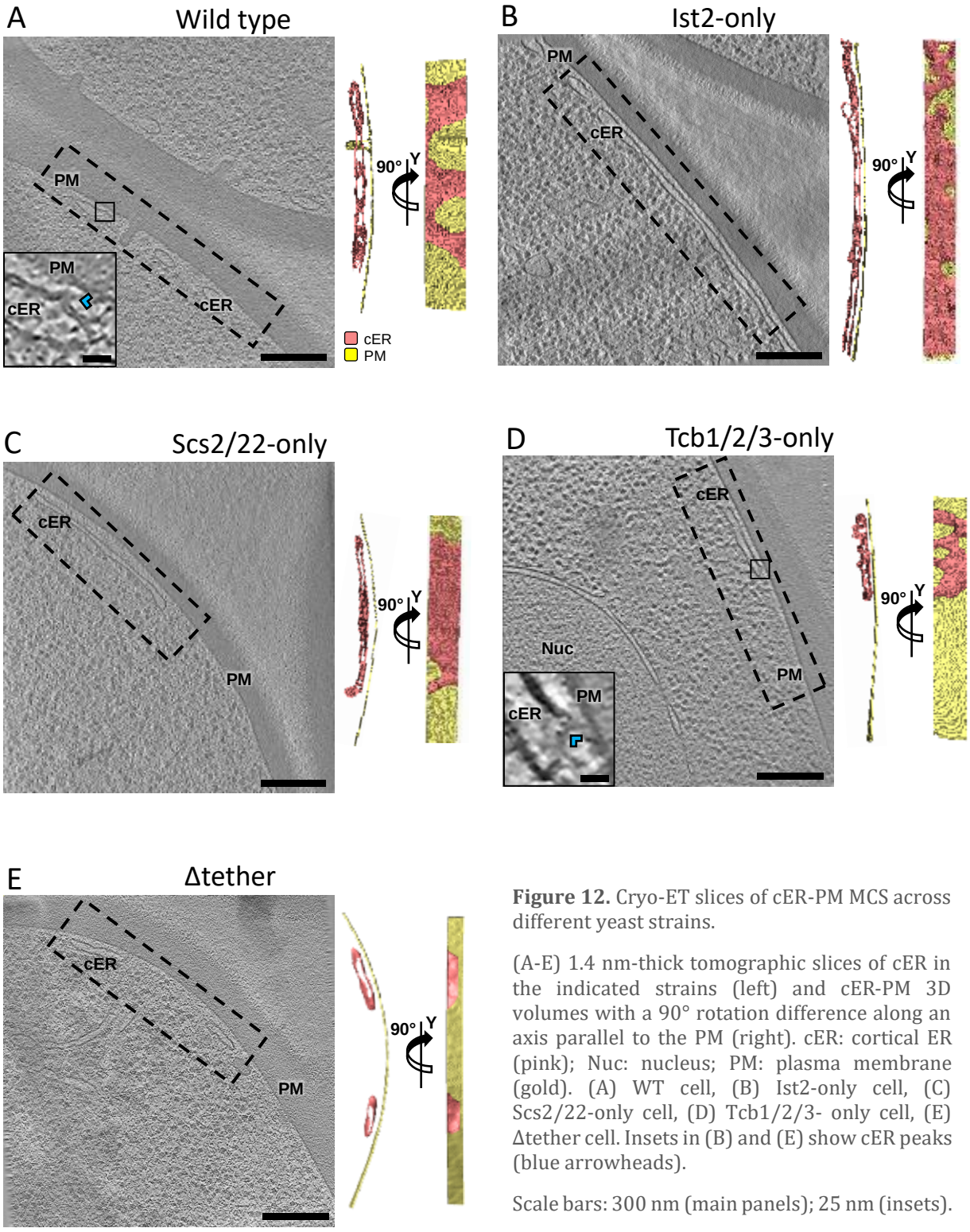

Figure 12. Cryo-ET slices of cER-PM MCS across different yeast strains.

(A-E) 1.4 nm-thick tomographic slices of cER in the indicated strains (left) and cER-PM 3D volumes with a 90° rotation difference along an axis parallel to the PM (right). cER: cortical ER (pink); Nuc: nucleus; PM: plasma membrane (gold). (A) WT cell, (B) Ist2-only cell, (C) Scs2/22-only cell, (D) Tcb1/2/3- only cell, (E) Δtether cell. Insets in (B) and (E) show cER peaks (blue arrowheads).

Scale bars: 300 nm (main panels); 25 nm (insets).

4.2.1 cER-PM distance varies depending on tether presence

To define the distances between cER and PM, the first step was to generate a triangular surface mesh from the 3D volumes of the membranes in the tomograms. To this end, every voxel in a tomogram was assigned a binary value, a 0 for background and a 1 for the membrane voxels that will form the volume. The surface of the membrane volume was then rendered as a triangular mesh, with a normal vector emanating from the centroid of each triangle.

These normals need to be further refined because of the quantization noise that arises from the discretization of the dataset. This denoising was done by using tensor voting with the geodesic neighborhood of each triangle, the size of which depends on a specified "radius hit" that matches the radius of the smallest feature of interest in the membrane. In this manner, the noise is averaged and removed from the normal vectors.

In order to register cER-PM distances, the denoised normal vectors emanating from each triangle centroid in the PM surface extend towards the cER until they intersect a triangle in its surface. The Euclidean lengths of these vectors were recorded as cER-PM distance (Figure 8B). The collection of measurements across different tomograms of the same strain yielded a distance distribution characteristic of each strain.

A similar approach was used to measure the thickness of cER. In this case, denoised normal vectors emanating from cER surface triangles must cross the luminal volume until they intersect with another cER triangle, registering the Euclidian length of this path as the cER thickness (Figure 8B).

Our results show that in Ist2-only cells the cER appeared very similar to that of WT cells, a combination of sheets and tubules. Although the cER-PM distance in this strain was slightly smaller than in WT (21 ± 4 nm, mean ± STD, N = 5 cER-PM MCS; $p < 0.05$ by unpaired t test; Figure 13A) the morphological similarities between both strains suggest that Ist2 has an important role in shaping the cER.

By contrast, Scs2/22-only cells had a radically different cER morphology, the most common topology being long, thin sheets whereas tubules were an infrequent find. The cER-PM cleft spanned a broader range of distances than in WT (26 ± 7 nm, mean ± STD, N = 5 cER-PM MCS; Figure 13A) which indicated a poor performance of Scs2/22 at controlling inter-organelle distance. In addition, the thickness of the cER sheets was significantly smaller than in WT (18 ± 6 nm, mean ± STD; $p < 0.01$ by unpaired t test; Figure 13B), sometimes down to a thickness of just 4 nm. This opens the question as to whether these extremely thin sheets have different properties compared to normal ER.

Tcb3-only cells displayed a cER morphologically opposite to Scs2/22-only cells, comprising mostly small tubules and short sheets. Shorter cER-PM distances were more abundant in this strain (20 ± 5 nm, mean ± STD; N = 9 cER-PM MCS; $p < 0.001$ by unpaired t test; Figure 13A) when compared to WT (23 ± 5 nm, mean ± STD) while the thickness, though more broadly distributed, was more comparable to that of WT and Ist2-only strains. However, the most remarkable feature of this strain was the abundance of high curvature peaks in the contact side of the cER (Figure 12D, inset).

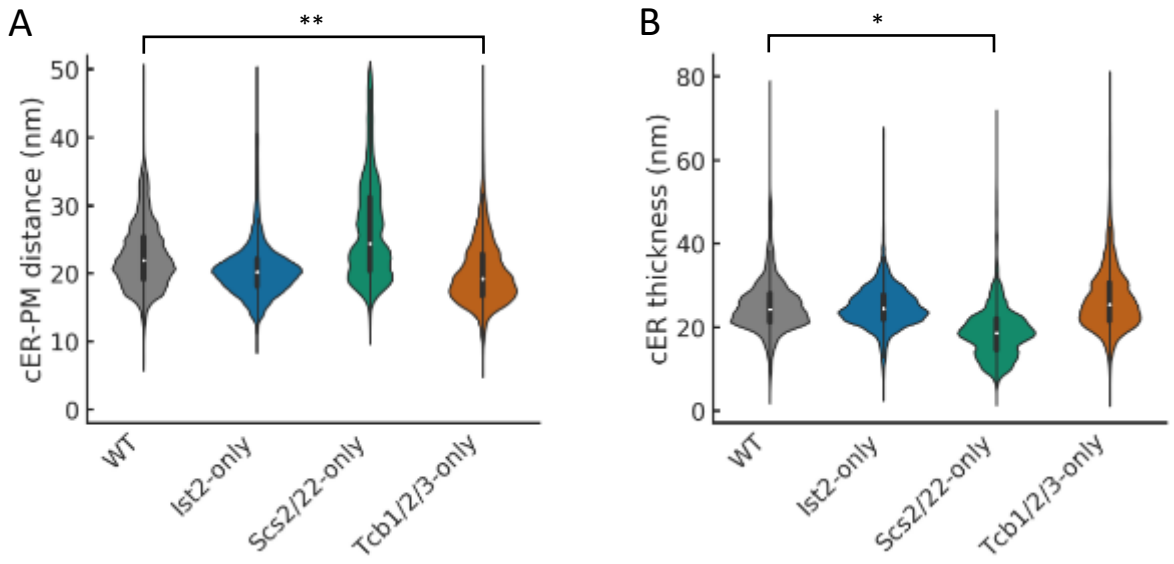

Figure 13. cER-PM intermembrane distance and cER thickness across strains.

(A) Distribution of cER-PM distances. A white dot represents the median, a black slab the interquartile range, and a black line 1.5 times the interquartile range.

(B) Distribution of cER thicknesses. A white dot represents the median, a black slab the interquartile range, and a black line 1.5 times the interquartile range.

*, **, and *** indicate, respectively, $p < 0.05$, $p < 0.01$ and $p < 0.01$ by unpaired t test. N = 6 (WT), 5 (Ist2-only), 5 (Scs2/22-only), 9 (Tcb1/2/3-only) cER-PM MCS.

In our tomograms, both leaflets of the lipid bilayer can be discerned at the peaks, indicating that they are part of the cER membrane. On average, these peaks had a conical shape with a radius of 10 nm (Figure 14A) and a height of 7 nm (Figure 14A). The separation distance between their tips and the PM is 8 nm (Figure 14A).

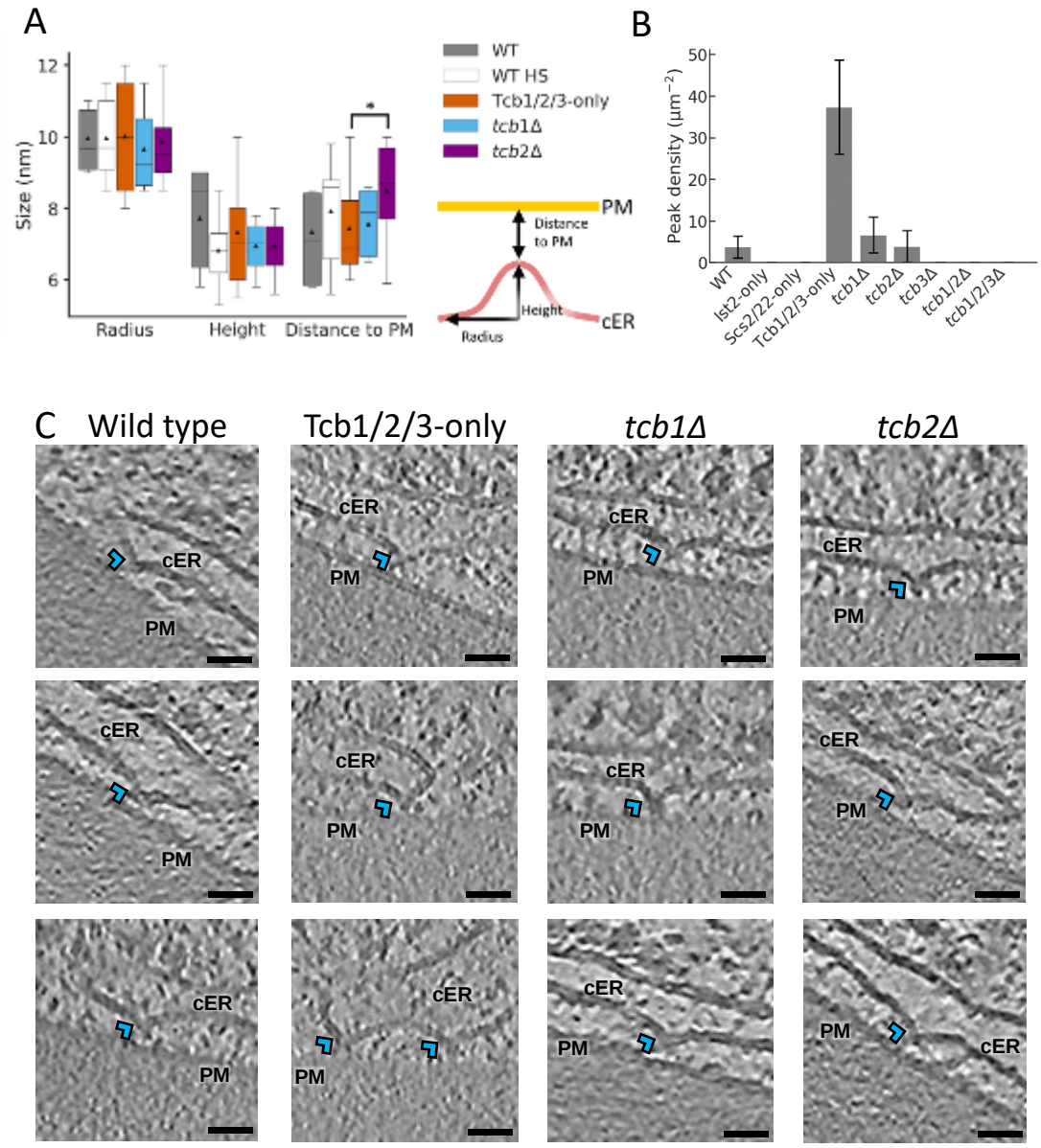

Figure 14. cER peak morphology and distribution.

(A) Quantification of cER peak morphology in terms of radius, height and distance of the tip to the PM. All strains in which cER peaks were found are displayed except *tcb3Δ* + Tcb3-GFP. Boxes represent all peak measurements per strain: 6 (WT), 21 (WT HS), 24 (Tcb1/2/3-only), 7 (*tcb1Δ*) and 15 (*tcb2Δ*) cER peaks. The horizontal lines of each box represent 75% (top), 50% (middle) and 25% (bottom) of the values, whiskers 95% (top) and 5% (bottom), and a black triangle the average value. N = 6 (WT), 7 (WT HS), 16 (Tcb1/2/3-only), 5 (*tcb1Δ*) and 10 (*tcb2Δ*) cER-PM MCS (cER peak morphology was analyzed in 7 additional Tcb1/2/3-only and 5 tcb2Δ tomograms that were not used for other quantifications). * indicates $p < 0.05$ by unpaired t-test.

(B) Quantification of cER peak density per µm2 of cER membrane area showing average values (gray bars) and SE (error bars). HS: heat shock (42C for 10 min). *, **, and *** indicate $p < 0.05$, $p < 0.01$ and $p < 0.01$ by Mann-Whitney U test. N = 6 (WT), 5 (Ist2-only), 5(Scs2/22-only), 9 (Tcb1/2/3-only), 5 (tcb1Δ), 5 (tcb2Δ), 5 (tcb3Δ), 5 (tcb1/2Δ), 5 (tcb1/2/3Δ) cER-PM MCS.

(C) 1.4 nm-thick tomographic slices of cER peaks in different strains (blue arrowheads). cER: cortical ER; PM: plasma membrane.

Scale bars: 25 nm.

Upon careful examination these peaks were also found, albeit less abundantly, in WT cells. They were however completely missing in Ist2-only and Scs2-22-only cells (Figure 14B), strains that lacked tricalbins. The WT peaks are morphologically identical to those found in Tcb1/2/3-only strain (Figure 14A, 14C), suggesting tricalbins are required for the formation of these structures. Another indicator of this was the absence of peaks in *tcb1/2/3*Δ cells (N=5 cER-PM MCS; Figure 14B).

4.2.2 cER curvature is affected by the tethers

Organelles rely on specific, characteristic morphologies to serve their function, such as the cristae of mitochondria or thylakoid stacks in chloroplasts (Shibata et al. 2009). The ER itself has morphologically distinct domains, with each subcompartment specializing in a specific role and the ability to shift morphologies in response to cell signaling (Hu et al. 2011; Schwarz and Blower 2016).

Membrane curvature is an important component of morphology, and it is far from being a passive feature of organelles. There are several molecular mechanisms with the purpose of generating and maintaining membrane curvature (McMahon and Gallop 2005; Martens and McMahon 2008; Shibata et al. 2009). Many cellular processes depend on membrane curvature to function such as exocytosis, and mitochondrial or vacuolar fusion. For this reason and the perceived differences in curvature between different strains, we quantitatively measured the cER curvature across strains.

The process of calculating cER curvature starts with the triangular surface mesh of the cER membrane. We used the denoised normal vectors in each triangle's geodesic neighborhood to obtain the principal directions and the maximal (k1) and minimal (k2) curvatures. These curvatures were then combined in a single scalar value, which was stored as a property of each triangle (Salfer et al. 2020). These values can later be visualized as a color-coded 3D rendering of the cER (Figure 15).

The overall curvature of cER in Ist2-only cells was similar to that of WT, albeit slightly less curved (Figure 15A, 15B, 15E). Scs2/22-only cells showed significantly less curved cER than WT cells ($p < 0.01$ by unpaired t test; Figure 15C, 15E), as it consisted of mostly sheets. By contrast, Tcb1/2/3-only cells had a higher overall cER curvature than all other strains including WT ($p < 0.001$ by unpaired t test; Figure 15D, 15E) due to their tubular morphology. In addition, the algorithm also detected the peaks of extreme curvature in Tcb1/2/3-only and WT strains (Figure 15A, 15D, insets).

There are many molecular mechanisms able to induce curvature. The lipid composition of a membrane can influence the relation between the monolayers and create curvature. Protein scaffolding and cytoskeleton interactions are just a few of the methods by which membranes can be curved (McMahon and Gallop 2005; Frolov et al. 2011; Stachowiak et al. 2013; Hirama et al. 2017). In the same manner, tricalbins have domains capable of inducing or sensing curvature by insertion in the outer monolayer like a wedge (hairpin and C2 domains) which suggests that tricalbins may induce curvature themselves at these peaks.

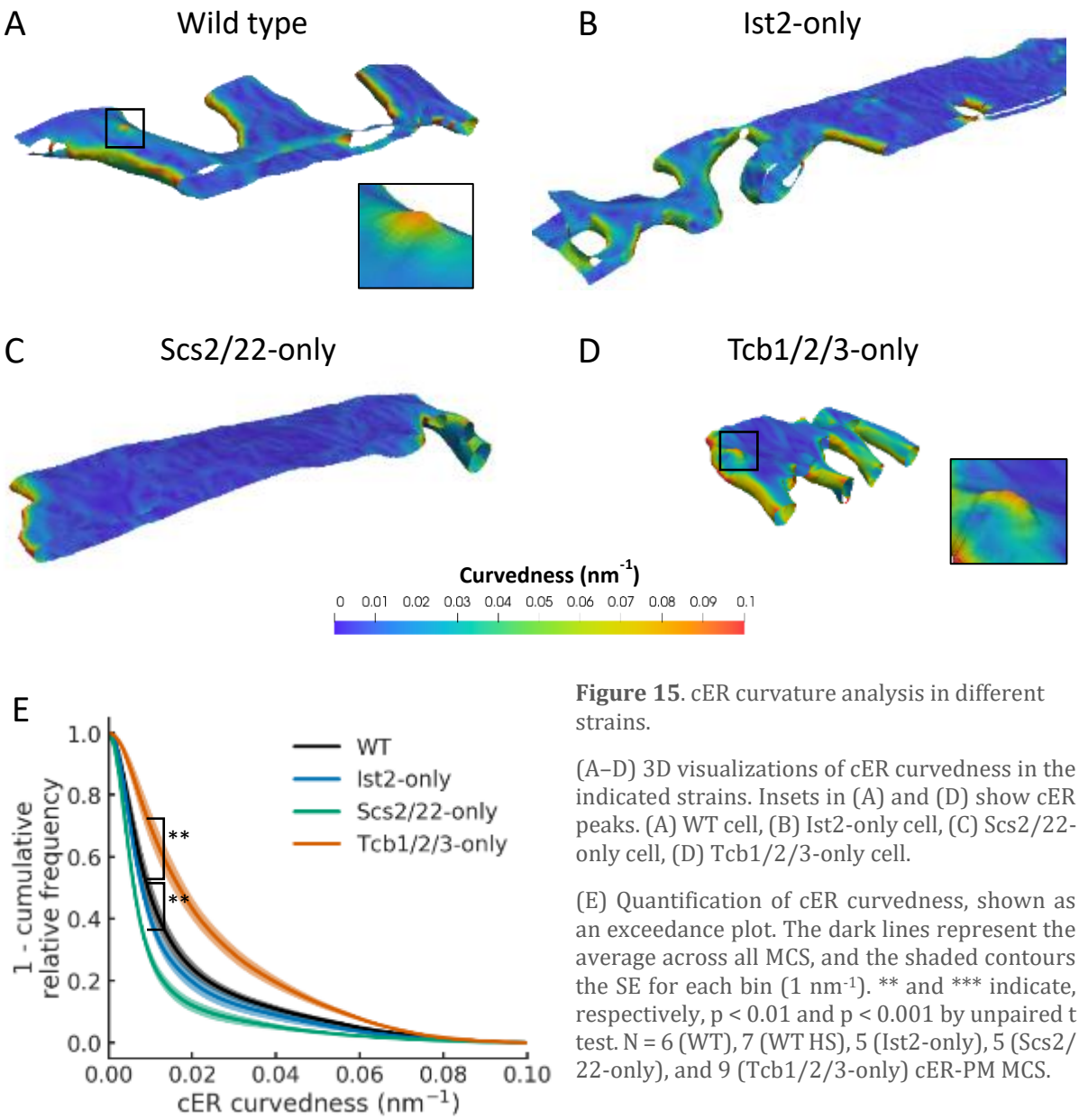

Figure 15. cER curvature analysis in different strains.

(A–D) 3D visualizations of cER curvedness in the indicated strains. Insets in (A) and (D) show cER peaks. (A) WT cell, (B) Ist2-only cell, (C) Scs2/22-only cell, (D) Tcb1/2/3-only cell.

(E) Quantification of cER curvedness, shown as an exceedance plot. The dark lines represent the average across all MCS, and the shaded contours the SE for each bin (1 nm^{-1}). ** and *** indicate, respectively, $p < 0.01$ and $p < 0.001$ by unpaired t test. N = 6 (WT), 7 (WT HS), 5 (Ist2-only), 5 (Scs2/22-only), and 9 (Tcb1/2/3-only) cER-PM MCS.

4.3 Tcb3 is necessary, but not sufficient for efficient peak formation

Operating under the hypothesis that tricalbins form high curvature peaks in the cER, we tested which tricalbins had to be present for peaks to form. To this end we used four strains that expressed different combinations of the three tricalbin proteins, such as only Tcb3 (*tcb1Δ tcb2Δ*), Tcb1/2 (*tcb3Δ*), Tcb1/3 (*tcb2Δ*), and Tcb2/3 (*tcb1Δ*), in the presence of Ist2 and Scs2/22. We proceeded to take tomograms of the cER in these strains and searched for the presence of peaks.

Our results showed that strains with a deletion of Tcb1 (N = 5 cER-PM MCS) or Tcb2 (N = 5 cER-PM MCS) formed peaks in quantities comparable to WT (N = 6 cER-PM MCS; $p > 0.5$ by Mann-Whitney-U test; Figure 14B, Figure 16A, 16B), suggesting that their functions are redundant and the expression of either of these tricalbins can compensate the absence of the other. The peaks in all peak-forming strains were morphologically indistinguishable (Figure 14A, 14C), which indicates that Tcb1 and Tcb2 have the same contribution to peak formation.

On the other hand, deletion of Tcb3 resulted in a peak-less phenotype (N = 5 cER-PM MCS; Figure 14B, Figure 16C) comparable to *tcb1/2/3Δ* (*tcb1Δ tcb2Δ tcb3Δ*) (N = 5 cER-PM MCS; Figure 14B, figure 16E), identifying it as an essential element for the formation of peaks. Strikingly, Tcb3 was not sufficient for the efficient formation of peaks in the absence of Tcb1/2 in our strain (N = 5 cER-PM MCS; Figure 14B, Figure 16D).

This supports the idea that tricalbins are not just able to heterodimerize like E-Syts (Creutz et al. 2004; Schulz and Creutz 2004; Giordano et al. 2013), but that this heterodimerization, between Tcb3 and either Tcb1 or Tcb2, is needed for peak formation.

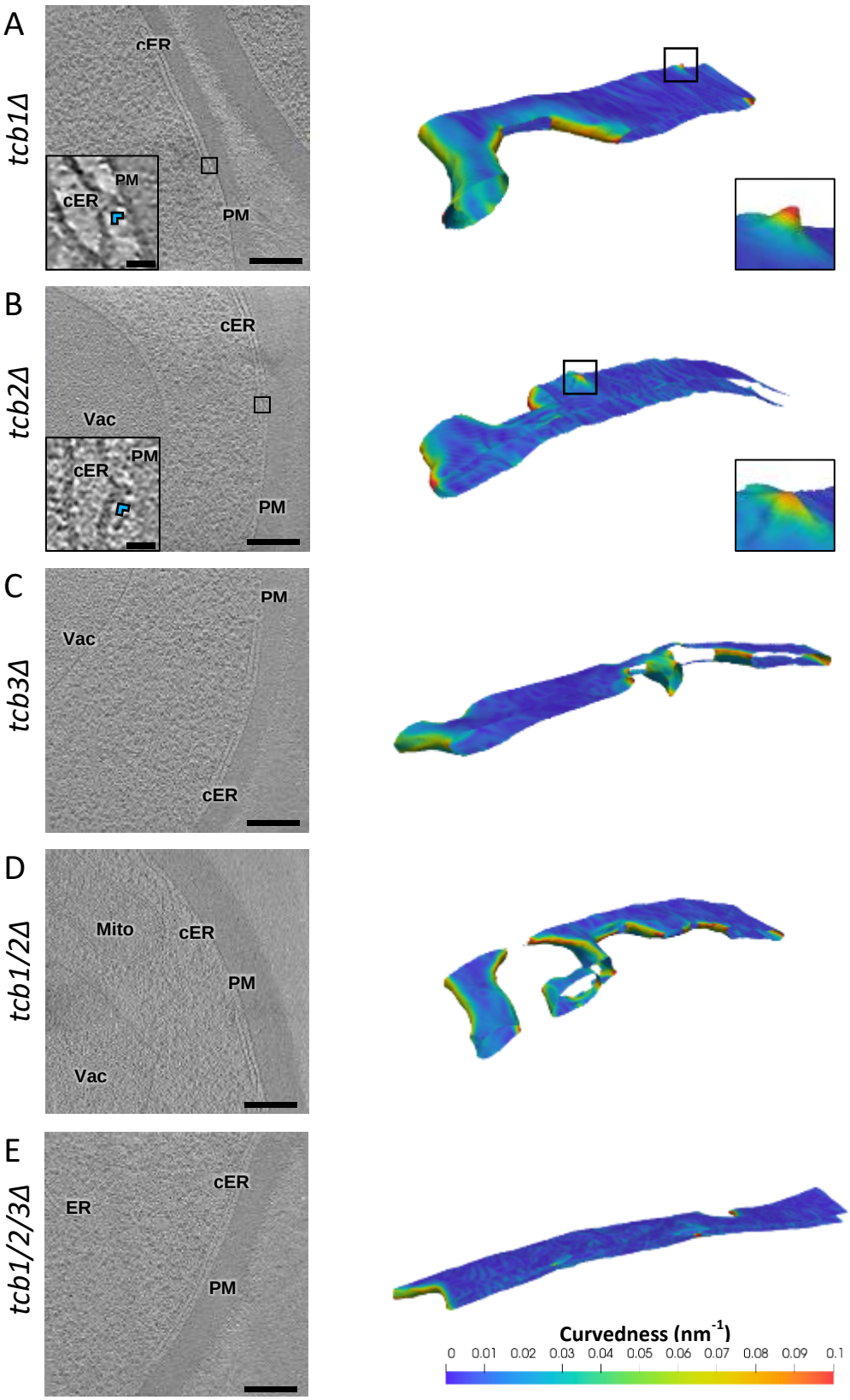

Figure 16. cER peak presence across different strains.

(A-E) 3D visualizations of cER curvature (right). (A) tcb1Δ, (B) tcb2Δ, (C) tcb3Δ, (D) tcb1/2Δ, (E) tcb1/2/3Δ cell. cER: cortical ER; Mito: mitochondrion; PM: plasma membrane; Vac: vacuole. Insets in (A) and (B) show cER peaks (blue arrowheads).

Scale bars: 300 nm (main panels); 25 nm (insets).

4.4 Tricalbins repair the PM under heat stress

The cER is essential for the maintenance of PM integrity, as well as for transducing signals related to membrane homeostasis in stress conditions such as heat shock (Omnus et al. 2016). During heat stress, the energy introduced in the system by quickly rising the temperature destabilizes the PM lipid bilayer and permeabilizes the cell, which can be lethal if left uncorrected. The ER is a hub in which most lipids required by the PM are synthesized, and the cER is an important gateway that could directly and efficiently transport these lipids to the PM. It is reasonable that lipid transport from the cER to the PM would become more essential to cell survival when the PM has undergone damage and needs these lipids to be repaired.

The same experimental approach detailed in Omnus et al. was used to determine the individual contributions of the ER-PM tethers to the maintenance of PM integrity under stress, specifically heat stress. This approach consisted on applying the fluorescent, cell impermeable dye propidium iodide to heat shocked cells expressing different combinations of ER-PM tethers. Cells with a compromised PM are significantly more permeable to propidium iodide than those with an intact one, and strains with a defect in PM repair are therefore more likely to take in the dye and give a fluorescent signal.

Our results show that Ist2 has virtually no contribution to PM integrity maintenance under heat shock, despite being a good tether capable of maintaining high amounts of cER in the absence of the other five tethers (Figure 17A). By contrast, Scs2/22 and Tcb1/2/3 have equal contributions to the PM lipid homeostasis under heat shock, and the sum of their contributions amounts to the total rescue of PM integrity defect phenotype of the Δtether phenotype (Figure 17A). This is particularly striking considering the small number of ER-PM contacts in Tcb1/2/3-only strain and suggests PM repair is not dependent just on the amount of cER, and that Scs2/22 and Tcb1/2/3 might contribute to PM integrity in other ways.

Additionally, we employed the same assay on the strains lacking one or two tricalbins to address the contribution of each one of them to PM repair. Independent deletion of Tcb1 or Tcb2 in a background containing the other five tethers had no influence on PM homeostasis, but cells lacking both of them exhibited a milder form of the compromised PM integrity phenotype of *tcb1/2/3Δ* cells (Figure 17B). By contrast, deletion of Tcb3 was sufficient to cause the compromised PM phenotype, albeit not as pronounced as the triple deletion (Figure 17B). The results show that the tricalbins needed to maintain PM integrity are the same that are necessary

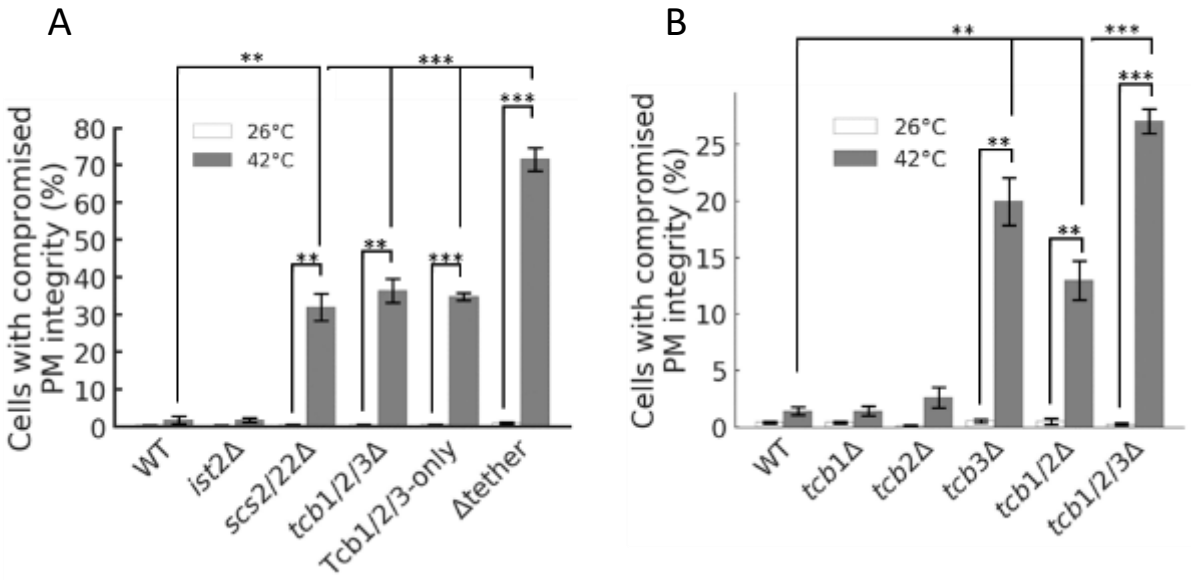

Figure 17. PM integrity under heat shock.

(A-B) Entry of propidium iodide in cells upon 10-minute incubation at 42°C measured by flow cytometry. The plots show average values (white/grey bars) for each condition ± SE (error bars). *, ** and *** respectively indicate $p < 0.05$, $p < 0.01$ and $p < 0.001$ by Mann-Whitney-U test (for WT 42°C and tcb1Δ 26°C data, which were not normally distributed) or unpaired t test (for all other conditions). N =4 independent biological repeats for all conditions.

to form high curvature peaks, suggesting that the ability of tricalbins to repair the PM is related to the formation of these peaks.

Despite the correlation between the formation of high curvature cER peaks and PM integrity, peaks are seldom seen in WT under normal conditions. Considering the WT peak abundance of ~4 peaks/μm^2 (Figure 14B) and approximating the peak geometry to a spherical dome with a radius of 9 nm and a height of 7 nm (Figure 14A), we estimate that peaks represent only 0.15% of the cER membrane forming the cER-PM contact. If these structures were important for maintaining the PM integrity under stress conditions, it would be reasonable to expect an increase in the number of peaks during heat shock.

To test this hypothesis, WT and *tcb1/2/3Δ* cells were heat shocked and plunge-frozen immediately after. Tomograms taken on these cells showed evident signs of heat shock, such as nuclear, cytoplasmic, and mitochondrial amorphous aggregates (Milleret al. 2015). In agreement with our prediction, heat shock triggered an increase in the number of cER peaks in WT cells (Figure 18A, 18B), while *tcb1/2/3Δ* cells remained peakless (Figure 18A, 18C). These results suggest that peak formation responds to damage to the PM through an unknown mechanism.

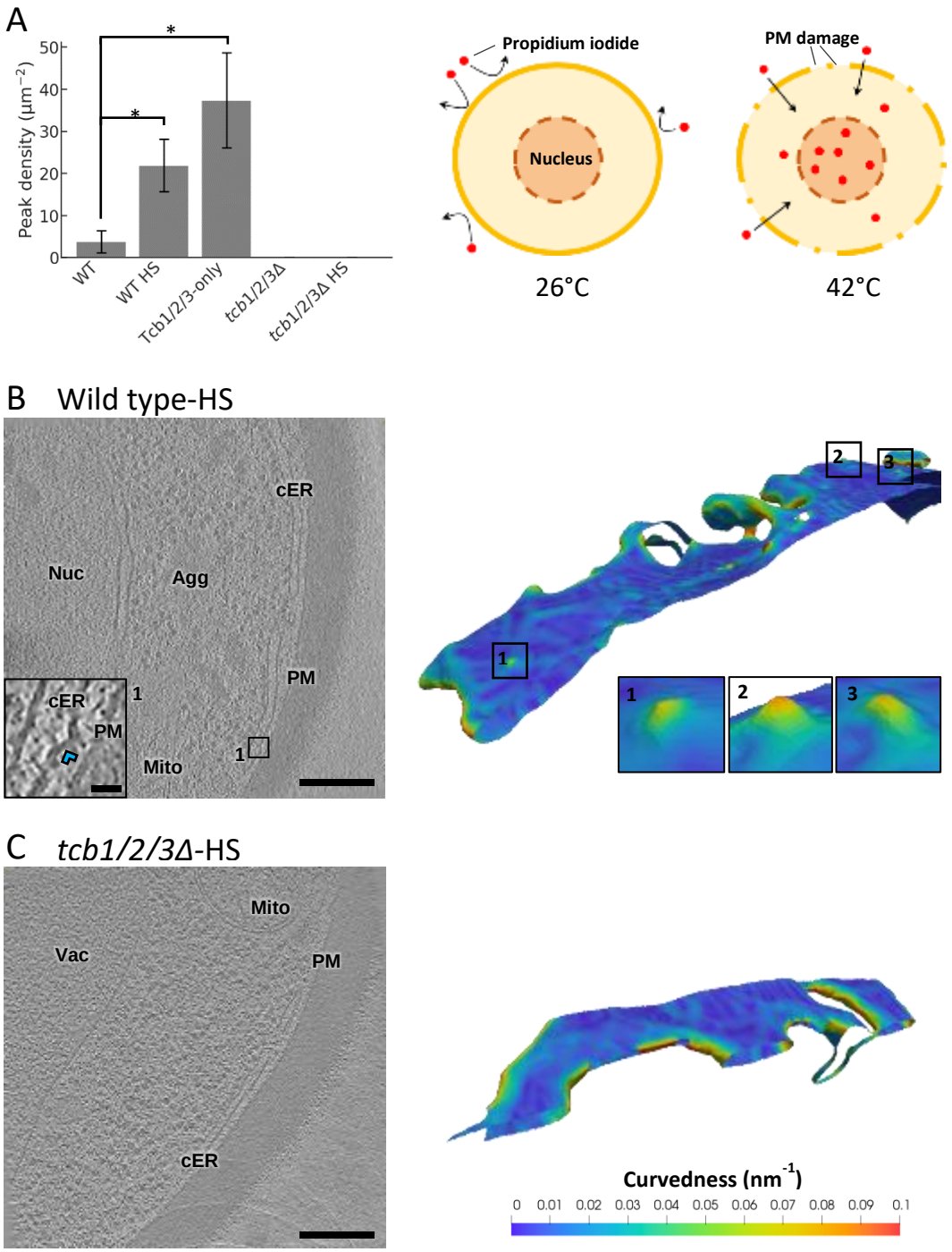

Figure 18. Heat shock effect on peak abundance.

(A) Peak density measurements of different strains at 26°C and after 10-minute incubation at 42°C. The plot shows average values (gray bars) for each condition ± SE (error bars). (left) and schematic of the propidium iodide assay to assess PM integrity (right). * indicates $p < 0.05$ by Mann-Whitney U test. N = 6 (WT), 7 (WT HS), 9 (Tcb1/2/3-only), 5 (*tcb1/2/3* Δ), and 5 (*tcb1/2/3Δ*-HS) cER-PM MCS.

(B-C) 1.4 nm-thick tomographic slices of cER in the indicated strains (left) and 3D visualizations of cER curvature (right). Agg: aggregate; cER: cortical ER; Mito: mitochondrion; Nuc: nucleus; PM: plasma membrane; Vac: vacuole. Insets show cER peaks (blue arrowhead).

Scale bars: 300 nm (main panels), 25 nm (inset).

4.5 High curvature peaks may facilitate lipid shuttling to PM

One of the ways in which tricalbins could contribute to PM homeostasis is through lipid transport between the cER and the PM. This is further supported by the ability of E-Syts to shuttle lipids between membranes in vivo (Saheki et al. 2016). Tricalbins share the same basic structure, including having a lipid binding SMP domain. Therefore, lipid transport could be a shared function of these proteins.

We speculated that the mechanism responsible for the importance of peaks to lipid transfer could be a direct consequence of their high curvature. Due to the cylindrical geometry of phospholipids, a highly curved membrane has a less ordered bilayer. A decrease in order in the bilayer could in turn facilitate the insertion of a lipid binding module such as SMP while at the same time reducing the energy cost of lipid extraction. As an added benefit, the peaks get closer to the PM than the rest of the cER, effectively reducing the travel distance of the lipid to the target membrane. However, without a sufficient number of peaks, lipid transfer from the peaks would still be minor compared to the lipid transport taking place at the rest of the surface of the ER, and their impact would be negligible.

Collaborator Dr. Felix Campelo at the ICFO employed a semi-quantitative model (Campelo and Kozlov 2014) to determine whether membrane geometry at the peaks could influence lipid transport. This model uses two components to describe the amount of free energy required for lipid extraction by a LTP. The first one comprises the collection of essential interactions at the membrane, such as hydrophobic and electrostatic interactions, and hydrogen bonds. This energy is independent of the geometry of the membrane. The second component is the elastic energy and it depends on the shape of the membrane prior to protein insertion in the outer monolayer. The elastic energy is affected by the spontaneous curvature (ζ_s) of the lipids at the membrane, which can be conical like PE and DAG (ζ_s= -1 nm^{-1}), cylindrical like PC (ζ_s= 0 nm^{-1}), or inverted conical like PIPs (ζ_s = 1 nm^{-1}) (Figure 19A). Therefore, spontaneous curvature influences the extraction energy ($\Delta\varepsilon_{ext}$) for a given lipid (Figure 19C), with conical lipids having the highest extraction energy.

The geometry of tricalbin-induced peaks was comparable across strains (Figure 14A), which could mean that these specific peak dimensions are important for tricalbin function. The model shows that for a curvature (J) corresponding to our peaks (J = 0.2 nm^{-1}) the only circumstances in which lipid extraction is not thermodynamically favorable are when the curvature sensing of the protein (α_j) is low, the lipid is highly conical, and many lipids are being extracted simultaneously (Figure 19B). In summary, under physiological conditions it is more efficient for a LTP to insert into and extract a lipid from a highly curved membrane (Figure 19C).

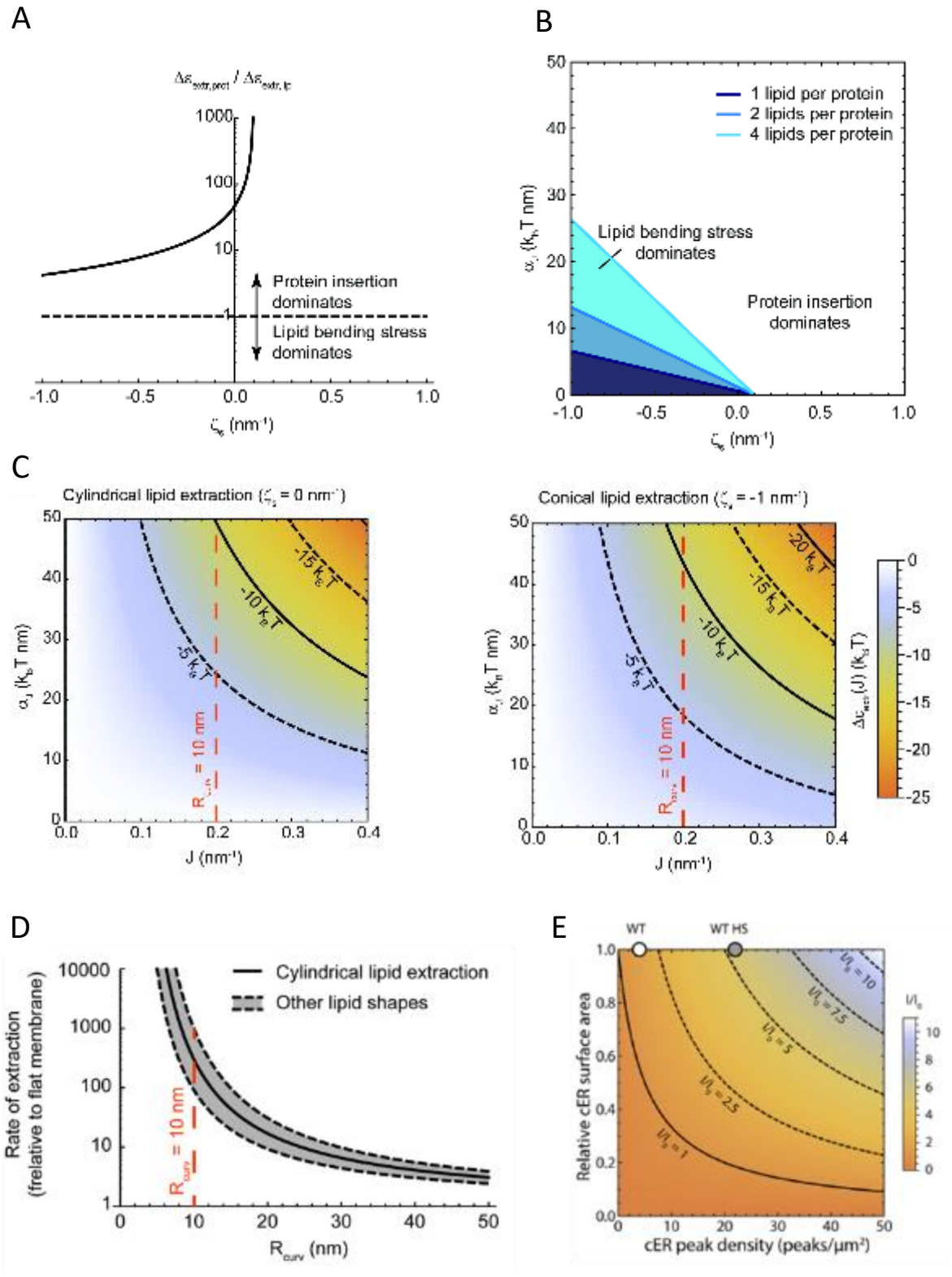

Figure 19. Membrane geometry and lipid spontaneous curvature effects on lipid transport.

(A) Ratio of protein insertion energy ($\Delta\varepsilon_{ext.prot}$) to elastic relaxation energy ($\Delta\varepsilon_{ext.lip}$) of the membrane for different values of lipid spontaneous curvature (ζ_s). Ratios higher than 1 indicate a dominance of protein insertion energy in the system, while values lower than 1 indicate a dominance of the lipid relaxation energy.

(B) Protein insertion domination (white region) and lipid relaxation domination (blue regions) regimes for different values of spontaneous curvature of the extracted lipid (ζ_s) and protein curvature sensitivity (α_j). The different shades of blue in the lipid relaxation domination regime correspond to the extraction of different number of lipids by a single protein (see legend).

(C) Extraction energy as a function of membrane curvature (J) and protein curvature sensitivity (αj) for a cylindrical lipid ($\zeta s = 0\ nm^{-1}$) (Left) and a highly conical lipid ($\zeta s = -1\ nm^{-1}$) (right). A dashed red line marks the curvature value observed for cER peaks. Isoenergy lines are drawn as solid and dashed black lines. k_BT the product of the Boltzmann constant and the absolute system temperature.

(D) Rate of lipid extraction by membrane curvature according to the Campelo and Kozlov model. The plot shows the rate of extraction for a standard cylindrical lipid (black line) as well as for lipids of other shapes, such as conical or inverted conical lipids (gray-shaded area between the dashed black lines). The radius of curvature of the experimentally observed cER peaks is highlighted by the dashed red line. $1/R_{curv}$ is equivalent to the curvedness for $k_1=k_2$.

(E) The plot shows I/I_0, where I_0 is the lipid extraction current (number of lipids extracted from the whole cER as a function of time) for a totally flat membrane and I is the sum of lipid extraction currents from the cER peaks and flat parts of the membrane. Our calculations were performed according to our prediction of a ~500-fold increase (Figure 19D) in lipid extraction rate at the peaks modelled as cones with a ~10 nm base radius and ~7 nm high (Figure 14A). Relative cER area in the Y axis was calculated respective to WT, where WT cER area = 1. cER peak density in the X axis was determined experimentally from our tomograms. In WT cells lipid flow from the peaks is comparable to the flow in the rest of the cER ($I/I_0 \approx 1.8$; white circle), but in heat shocked WT cells (WT-HS) the ~6-fold increase in peak density translates to a dominating contribution from cER peaks ($I/I_0 \approx 5.4$; grey circle).

Our results show that for a structure with a mean membrane curvature radius of 10 nm the energy barrier for lipid extraction is decreased by ~$6k_BT$, which would translate into a 500-fold increase in lipid transport for cylindrical lipids. It is worth noting that this value varies for lipid species with effective spontaneous curvatures, which can either follow the peak curvature (inverted conical lipids) or go against it (conical lipids) (Figure 19D). We estimated peaks to amount to only ~0.15% of WT cER contact surface under normal conditions, but taking the model's predictions of a 500-fold increase into account, the lipid transfer rate from the peaks matches the lipid transfer from the rest of the cER at the contact (Figure 19E). In addition, from our Cryo-ET data we estimated the number of peaks to increase ~6 times in WT during heat shock, potentially increasing lipid transfer at the peaks ~5 fold and making them the primary gateway for lipid transport in ER-PM contacts during stress (Figure 19E).

Another beneficial effect of the disparity in transfer rates between a lipid transported from the cER to PM compared to a lipid transported in the opposite direction is the strong directionality of this process. It becomes more energetically favorable to bind and transport lipids from the cER peak than to extract them back from the flat PM, which would prevent the backflow of lipids.

4.6 Tcb3 SMP and C2 domains are necessary for efficient peak formation

Our results pointed to Tcb3 as the key component in the maintenance of PM integrity during heat shock stress, possibly by enabling fast lipid shuttling through the formation of highly curved cER membrane peaks at the contact site with the PM. Tcb3 was also necessary for peak formation in the cER membrane. The structure of Tcb3 is comparable to Tcb1/2, therefore the question arises as to which part of Tcb3's structure makes it functionally different from its counterparts.

The modular nature of tricalbins allowed us to create deletion mutants for the domains of Tcb3 and discover how they affect its ability to contribute to the formation of peaks, and how this would translate to PM integrity.

We employed three GFP-tagged constructs to complement the tcb3Δ strain. One contained full-length Tcb3 (Tcb3-GFP) and was expected to rescue the heat shock sensitivity phenotype of *tcb3Δ* cells. The second construct lacked the SMP domain (Tcb3 SMPΔ-GFP) and the third one lacked C2 domains (Tcb3 C2Δ-GFP).

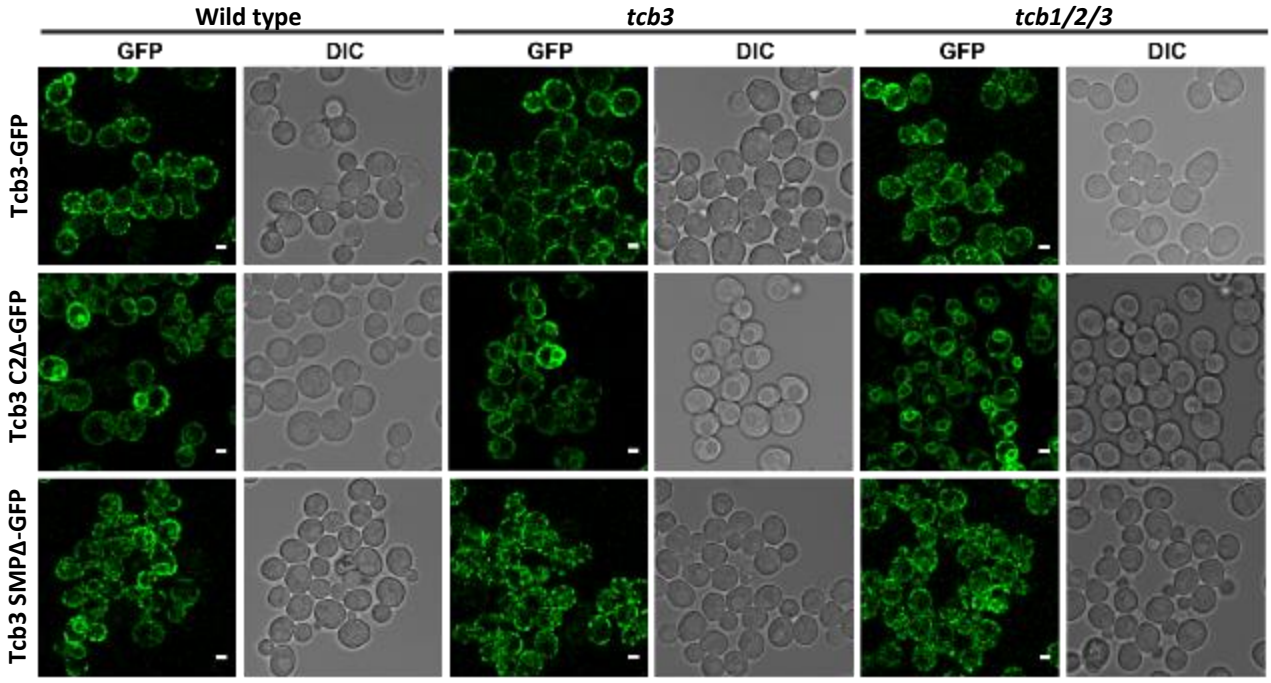

Figure 20. Cellular localization of Tcb3 constructs.

Light microscopy imaging of GFP fluorescence (mid-section plane confocal images; left) and DIC (right) of WT, *tcb3Δ* and *tcb1/2/3Δ* cells expressing full length Tcb3-GFP, Tcb3 C2Δ-GFP, or Tcb3 SMPΔ-GFP.

Scale bars: 2 μm.

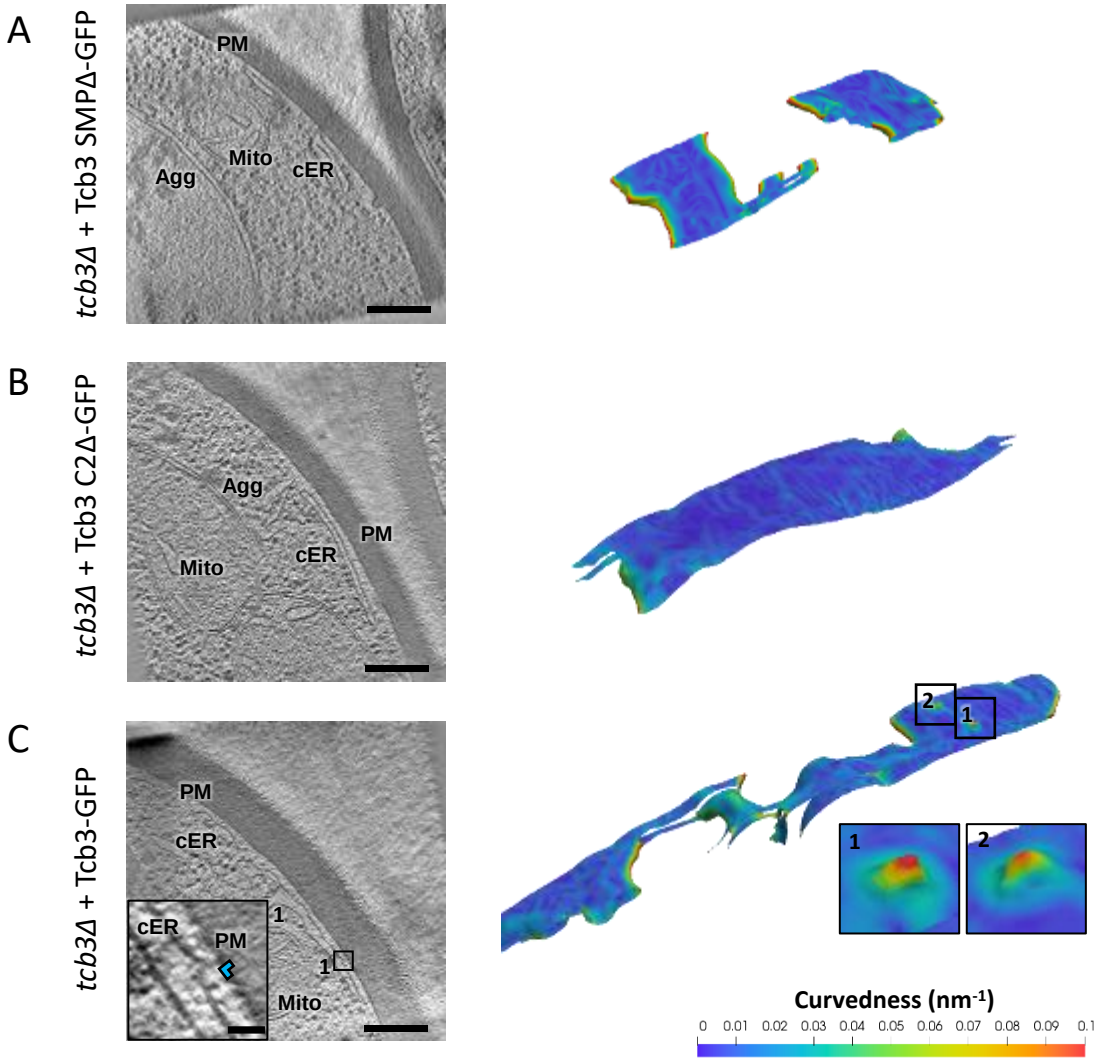
A
tcb3Δ + Tcb3 SMPΔ-GFP
PM
Agg
Mito
cER
B
tcb3Δ + Tcb3 C2Δ-GFP
Agg
PM
Mito
cER
C
tcb3Δ + Tcb3-GFP
PM
cER
cER
PM
Mito
1
2
Curvedness (nm-1)
0 0.01 0.02 0.03 0.04 0.05 0.06 0.07 0.08 0.09 0.1

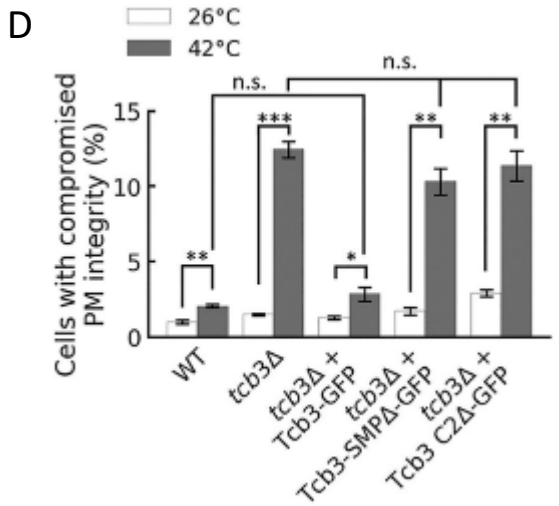
D
26°C
42°C
Cells with compromised PM integrity (%)
n.s.
n.s.
***
**
**
**
*
WT
tcb3Δ
tcb3Δ + Tcb3-GFP
tcb3Δ + Tcb3-SMPΔ-GFP
tcb3Δ + Tcb3 C2Δ-GFP

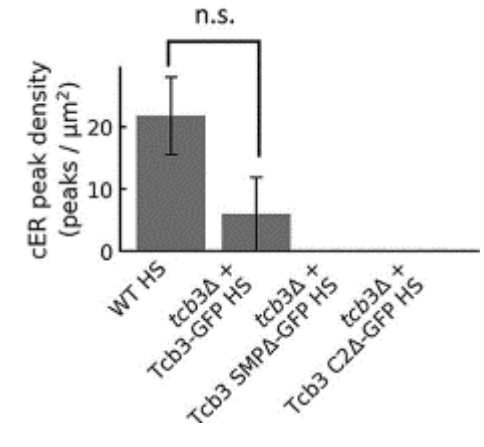
E
n.s.
cER peak density (peaks / µm2)
WT HS
tcb3Δ + Tcb3-GFP HS
tcb3Δ + Tcb3 SMPΔ-GFP HS
tcb3Δ + Tcb3 C2Δ-GFP HS

Figure 21. cER peaks and PM integrity in *tcb3Δ* strain complemented with truncated Tcb3 constructs.

(A–C) 1.4 nm-thick tomographic slices of cER in different strains (left) and 3D visualizations of cER curvature (right). Agg: aggregate; cER: cortical ER; Mito: mitochondrion; Nuc: nucleus; PM: plasma membrane. (A) *tcb3Δ* + Tcb3-GFP HS, (B) tcb3Δ + Tcb3 SMPΔ- GFP HS, (C) *tcb3Δ* + Tcb3 C2Δ-GFP HS. Insets show cER peaks (blue arrowhead in the tomographic slice inset).

Scale bars: 300 nm (main panels); 25 nm (insets). The contrast of the tomographic slices in (A), (B), and (C) was enhanced using a deconvolution filter.

(D) PM integrity assay of *tcb3Δ* cells complemented with Tcb3 truncation constructs upon 10-minute incubation at 42°C. The plot shows average values (white/gray bars) for each condition ± SE (error bars). n.s., *, **, and ***, respectively, indicate $p > 0.05$, $p < 0.05$, $p < 0.01$, and $p < 0.001$ by unpaired t test. N = 4 independent biological repeats for all conditions.

(E) cER peak density per μm2 of cER membrane area at the contact showing average values (gray bars) ± SE (error bars). N = 7 (WT HS), 3 (*tcb3Δ* + Tcb3-GFP HS), 3 (*tcb3Δ* + Tcb3 SMPΔ-GFP HS), and 3 (*tcb3Δ* + Tcb3 C2Δ-GFP HS) ER-PM MCS. n.s. indicates $p > 0.05$ by Mann-Whitney U test.

Confocal florescent microscopy confirmed that all three constructs targeted the cER (Figure 20), although both SMP and C2 truncated versions showed a slightly higher signal at the cytoplasmic ER and the nuclear envelope than the full-length construct, indicating a partial localization defect. As we expected, the construct with full-length Tcb3 rescued the PM integrity defect to levels similar to WT (Figure 21D), while the constructs lacking SMP or C2 failed to achieve even a partial rescue.

Previously, we found strong evidence to suggest a correlation between PM integrity and the ability to form cER peaks. For this reason, we heat shocked cells expressing the three Tcb3 constructs and imaged them with Cryo-ET (Figure 21E). Out of the three constructs we employed only Tcb3-GFP rescued the peakless phenotype of *tcb3Δ* (Figure 21E, 21C, insets) while no peaks were found in the other two strains (Figure 21A, 21B). The PM integrity assay revealed that in *Δtcb3* cells the expression of Tcb3-GFP was sufficient to confer resistance to heat shock comparable to wild type. On the other hand, expression of the two truncated Tcb3 constructs lacking the SMP or C2 domains failed to rescue the phenotype, and showed a permeability comparable to *Δtcb3* cells (Figure 21D). Thus, our results again associated PM integrity during heat stress with the presence of peaks in the cER.

These results show that both SMP and C2 domains of Tcb3 are necessary for efficient peak formation, and at least partially for proper localization.

5 Discussion

5.1 ER-PM tethers shape the ER

Our data suggests ER-PM tethers contribute to the morphology of the cER in addition to regulating the total contact surface.

Out of the six proteins studied, Ist2 performs the best as a tether, maintaining a significant amount of cER in the absence of the other five. The morphology of the cER in Ist2-only cells is reminiscent of WT cER, and the ER-PM distance is even more tightly controlled at around 21 nm. Despite being a very effective tether, it lacked any effect on PM integrity maintenance during heat stress. This reinforces the notion that specialized mechanisms are involved in PM repair and contact surface is not a defining factor.

The main incognita regarding Ist2 is how its elongated structure translates to an ER-PM distance of 21 nm. The unstructured linker portion of Ist2 between the last transmembrane helix and the CSS domain contains approximately 340 aa. Fully extended, this linker could span a 120 nm distance between membranes, which does not correlate with the observed measurements. One possible explanation lies in indications that this linker region is not just structural, but provides a binding point for proteins like Osh6/7. Binding to Ist2 is necessary for their localization to ER-PM contacts and PS transport to the PM (D'Ambrosio et al. 2020). This protein-protein interaction could limit the maximum extension of the linker region, making a 21 nm contact distance more likely to happen.

By contrast, Scs2/22 did not seem to effectively control ER-PM distance, with the highest distance variability being found in the strain that only expresses these two tethers. One possible explanation lies in the indirect nature of Scs2 mediated tethering. Osh2/3 are the most likely candidates to bridge the gap by connecting Scs2/22 to the PM. In the case of Osh3, the unstructured region between the FFAT domain and PH domain can potentially span 37 nm (Tong et al. 2013) justifying the distances observed. The question remains as to whether this distance would be compatible with lipid transport by Osh proteins.

Another remarkable feature of Scs2/22-only cER was the low thickness and great length of its sheets. It seems unlikely that the TM tails of Scs2/22 interact with some luminal factors to bind both ER membranes due to their short length. It is therefore more likely that other unknown factors are at play, such as changes in the lipid composition of the cER. It is worth mentioning that

reticulons appeared in an interactome screening of Scs2 (Manford et al. 2012), so it is possible they are involved in causing this unusual morphology.

The most striking morphological effect was found in the Tcb1/2/3-only strain. The curved phenotype of Tcb1/2/3-only cER is likely the result of several factors as opposed to the effect of a single domain of tricalbins. Compared to their partners Scs2/22 and Ist2, tricalbins have been confirmed to be poor tethers. This reduction in effective anchor points would result in a more scattered cER, which in turn would contribute to the presence of short sheets and even tubes as opposed to the longer sheets that better tethers could maintain. This is the reason why the infrequent cER in *Δtether* cells also tends to be composed of short sheets. In addition, tricalbins localize to the highly curved edges of the cER (Hoffmann et al. 2019) thanks to their hairpin TM domain. These domains could stabilize the curvature at curved regions, contributing to the highly curved phenotype.

To reemphasize, and as mentioned before, the dysregulation of other cellular factors may contribute to the morphology of cER in strains lacking one or more tethers, but nonetheless the evidence suggests that the tethers directly affect cER morphology.

5.2 Tricalbins maintain PM integrity through peak formation

Peaks of extreme curvature were seen in the cER membrane facing the PM in cells expressing tricalbins. They were most abundant in the strain expressing only Tcb1/2/3, but they could also be spotted in WT tomograms. Under stress conditions, heat stress specifically, the number of peaks considerably increased in WT cells. Peaks were absent from strains lacking tricalbins, both under normal and stress conditions, indicating tricalbins form these peaks. Additionally, in all strains where peaks were present they were found to be morphologically indistinguishable. The presence of peaks in the Tcb1/2/3-only strain also confirmed they are formed without the need of Ist2 or Scs2/22.

There are many indicators that the function of these peaks is to facilitate lipid transport. Firstly, there is a clear structural and likely functional similarity of tricalbins with mammalian E-Syts and plant synaptotagmins, which are lipid transporters also localized at ER-PM contact sites (Schapire et al. 2008; Saheki and de Camilli 2017a). Moreover, the ER is the main producer and regulator of lipids in the cell. The enzymes that reside within it are responsible for the synthesis of PC, PE and PIs, as well as having a role in sterol synthesis. For this motive, membrane contacts with the ER fulfill a major lipid-transport role (Lahiri et al. 2015), and it is possible that membrane structures like highly curved peaks could serve this purpose.

This is made more evident when considering the effect of extreme membrane curvature on lipid transport. As described in our model, cER peak-induced stress could improve lipid transport by decreasing the energy required to extract a lipid from the membrane, while at the same time facilitating the insertion of lipid binding domains in the more disordered lipidic membrane at the peak. Despite comprising a small area of the cER, our model predicts that lipid transport at the peaks in a WT cell could be as high as in the rest of the cER, and even more so during heat stress due to the increase in peak formation. Facilitating lipid transport through peak formation would also add directionality to the transport, preventing the backflow of lipids from the PM to the cER at the peak site, further increasing transport efficiency.

In this work we hypothesize that this improvement in lipid transport could be a way to accelerate the repair of the PM under stress conditions. This would explain why strains that fail to form peaks show a higher PM permeability under heat stress than those that do, and how this has detrimental effects for the cell. Heat shocked cells would experience rising lipid transport demands to repair the PM, and this would cause an increase in peak formation to accommodate that demand.

There is evidence that plant synaptotagmins have this role of PM repair through lipid transport (Schapire et al. 2008), and indirect data that hints at a similar role for tricalbins in yeast, especially Tcb3 (Aguilar et al. 2007). However, and taking all these points into account, it is surprising that while tricalbins and E-Syts should have an important function in the cell, neither the removal of tricalbins in yeast (Manford et al. 2012) nor E-Syts in mice (Sclip et al. 2016) appear to have the expected catastrophic effect. It is likely that under normal conditions the lipid transporting roles of tricalbins and E-Syts can be replaced by other mechanisms, while they become more relevant under stress conditions.

We propose that cER peak formation is a stress-induced response to PM damage to facilitate rapid lipid transport, and hypothesize that this response might be similarly conserved across different organisms.

5.3 SMP and C2 domains are necessary for peak formation

Our results show how Tcb3 is necessary but not sufficient for efficient peak formation at normal expression levels. However, Tcb3 seems to be sufficient to induce peaks when overexpressed (Hoffmann et al. 2019).

We believe the reason for this behavior hinges on the preferred cellular localization of each tricalbin. It is possible that Tcb1/2 localize preferentially to the cER, while Tcb3 has a more

distributed presence across all the ER. We hypothesize that dimerization of Tcb3 with Tcb1/2 helps to efficiently recruit Tcb3 to the ER-PM contacts under normal expression levels. However, in the absence of Tcb1/2 and in sufficient numbers, enough Tcb3 could reach the cER where it homodimerizes and forms peaks.

Dimerization is done through the SMP domains of tricalbins, and removing the SMP domain of Tcb3 affects its localization to the cER (Figure 20), further indicating that dimerization with Tcb1/2 is necessary for localization. Moreover, Tcb3 proteins lacking the SMP domain do not induce peak formation, suggesting a relation between dimerization and peak formation. This indicates that curvature induction is a property of the tricalbin dimer, rather than any individual tricalbin. It is currently unknown whether tricalbins have preferred dimerization partners, but the SMP sequences provide no evidence to suggest they do. Using the SMP dimerization interface for E-Syt2 (Schauder et al. 2014) as a reference, the alignment of the tricalbins revealed a high similarity between the aminoacids at the dimerization site. Furthermore, aminoacids with a high degree of conservation among tricalbins were often conserved in E-Syt2 as well (Figure 22). This information supports that at least on an SMP sequence level tricalbins do not have preferred dimerization partners. Moreover, it begs the question of whether there might be a certain universality to E-Syt SMP dimerization mechanics.

In addition to the SMP domain, Tcb3 requires its C2 domains for localization (Figure 20) and to induce curvature. Despite having the SMP domain, the lack of C2 domains affects the localization of Tcb3 to the cER. This is likely caused by the absence of at least one C2 domain that interacts with the $PI(4,5)P_2$ at the PM. More importantly, the absence of Tcb3 C2 domains results in an absence of peaks even when full-length Tcb1/2 are present. Due to the high number of C2 domains involved and the lack of information regarding their structure, we hypothesize that there must be a fundamental difference between the C2 domains of Tcb3 and those of Tcb1/2 that allows a tricalbin dimer to induce curvature.

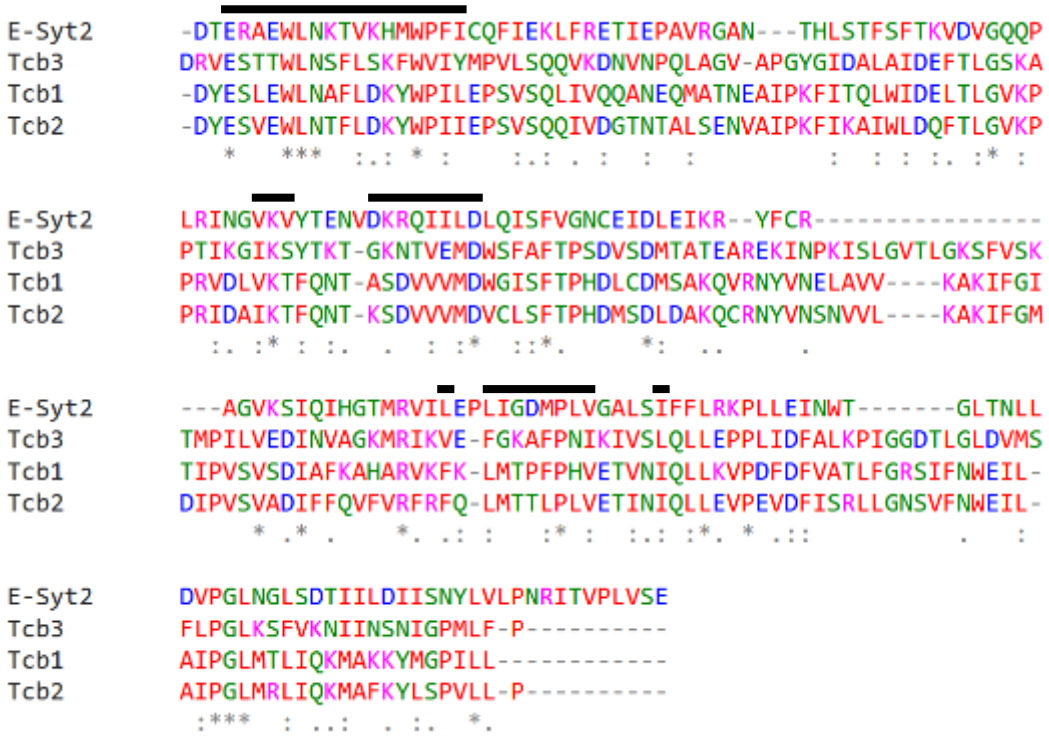

Figure 22. SMP sequence comparison.

Multiple sequence alignment of the SMP sequences of human E-Syt2 and yeast Tcb1, Tcb2, and Tcb3 using Clustal Omega (Sievers et al. 2011). Bold black lines indicate regions at the dimer interface (Schauder et al. 2014). Aminoacid similarity between sequences is categorized as same aminoacid (*), conserved substitution (:), and semi-conserved substitution(.). Aminoacid coloring is determined by aminoacid type; red: small side chain including tyrosine; blue: acidic; magenta: basic excluding histidine; green: hydroxyl, sulfhydryl, and amino side chains including glycine.

5.4 Curvature induction mechanism

Despite the evidence that tricalbins, and possibly E-Syts, are involved in a conserved response to damage in the PM by facilitated lipid transport through curvature induction, the question still remains as to the mechanism by which this is accomplished.

One of the best initial candidates for the role of curvature induction moiety in tricalbins was the hairpin shaped N-terminus. However, this domain seems to affect only the localization of tricalbins to high curvature regions on the ER surface, such as tubules and sheet edges (Hoffmann et al. 2019), where at most it contributes to curvature stabilization. It is possible that this domain assists tricalbins in localizing to the high curvature peaks and prevent their diffusion away from them.

C2 domains are then left as the most likely cause of curvature induction by tricalbins. However, assigning individual functions to each of the different C2 domains in tricalbins can be challenging. For example, the presence of a basic residue cluster on the surface of a C2 domain (Giordano et al. 2013) might indicate a role in PM binding by electrostatic interactions with acidic phospholipids. At the same time, the lack of positive charges could instead indicate a binding preference for the ER membrane, where C2 domain insertion could induce curvature (Martens et al. 2007). In addition to this, the presence or absence of calcium binding sites adds another layer of depth to the problem and makes it more difficult to determine the behavior of these domains. To complicate matters even more, the presence of calcium binding residues in C2 domains is not always a guarantee of calcium or lipid binding, and it can even act as an inhibitor (Jeyasimman and Saheki 2020). The number and complexity of C2 domains in tricalbins also make it challenging to determine the function of each one, since their interactions with each other can hardly be determined by theoretical work. It is however possible to use homology modelling to simulate the structure of tricalbin C2 domains and make educated guesses about their activity (sections 5.4.1-5.4.3).

Taking all this into account, we reach the conclusion that more structural and biochemical information are needed in order to determine the exact roles of each C2 domain. It is however possible with our current knowledge to propose a model, that although highly hypothetical, could prove useful in guiding further experiments and provide context for future observations. For this we would assume that E-Syts, despite not having been proven to form peaks, use a similar mechanism to facilitate lipid transport. Also, even though a domain-by-domain identity cannot be established between tricalbins and E-Syts, their general architecture is very similar and can be used to assign roles to the C2 domains of tricalbins (Figure 23).

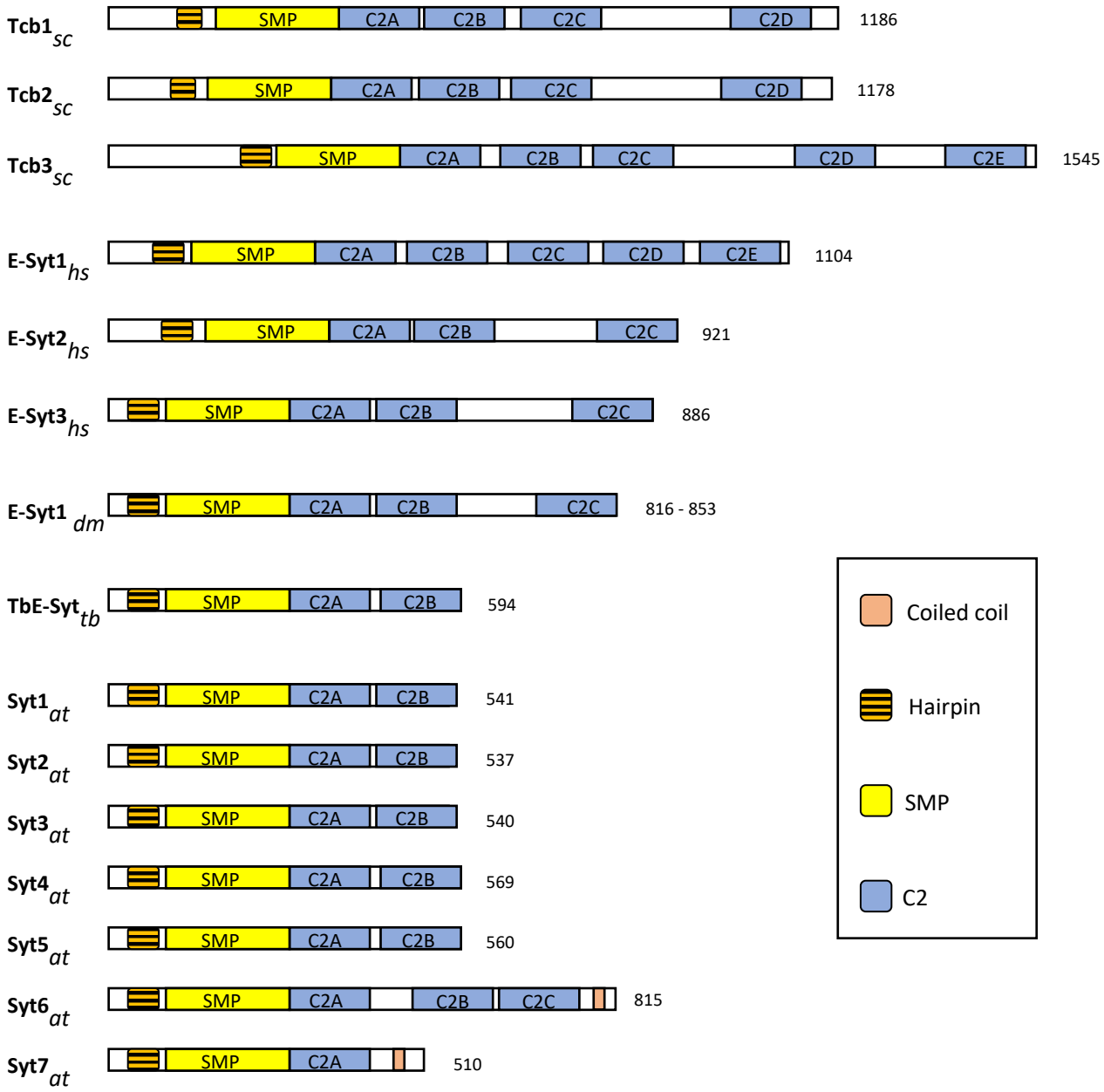

Figure 23. Extended synaptotagmins.

General architectures of extended synaptotagmins orthologs across a variety of different organisms (Kikuma et al. 2017; Saheki and de Camilli 2017b; Ishikawa et al. 2020; Stepinac et al. 2021). Protein length is displayed on the right of each diagram. The subscript on the protein name indicates the organism. *sc*: *Saccharomyces cerevisiae*; *hs*: *Homo sapiens*; *dm*: *Drosophila melanogaster*; *tb*: *Trypanosoma brucei*; *at*: *Arabidopsis thaliana*.

The first point that needs to be addressed is the existence of three E-Syts and three tricalbins, as multiple protein interactions have the potential to complicate our model beyond coherency. As previously mentioned, Tcb3 requires one of the other two tricalbins to efficiently form peaks at normal expression levels in WT. Fortunately, overexpressing Tcb3 appears to

circumvent this need (Hoffmann et al. 2019). This means Tcb3 contains all the elements required for peak formation, while Tcb1/2 likely have a support role in it. This however does not dismiss the possibility that Tcb1/2 dimers may have other functions beyond the scope of this study.

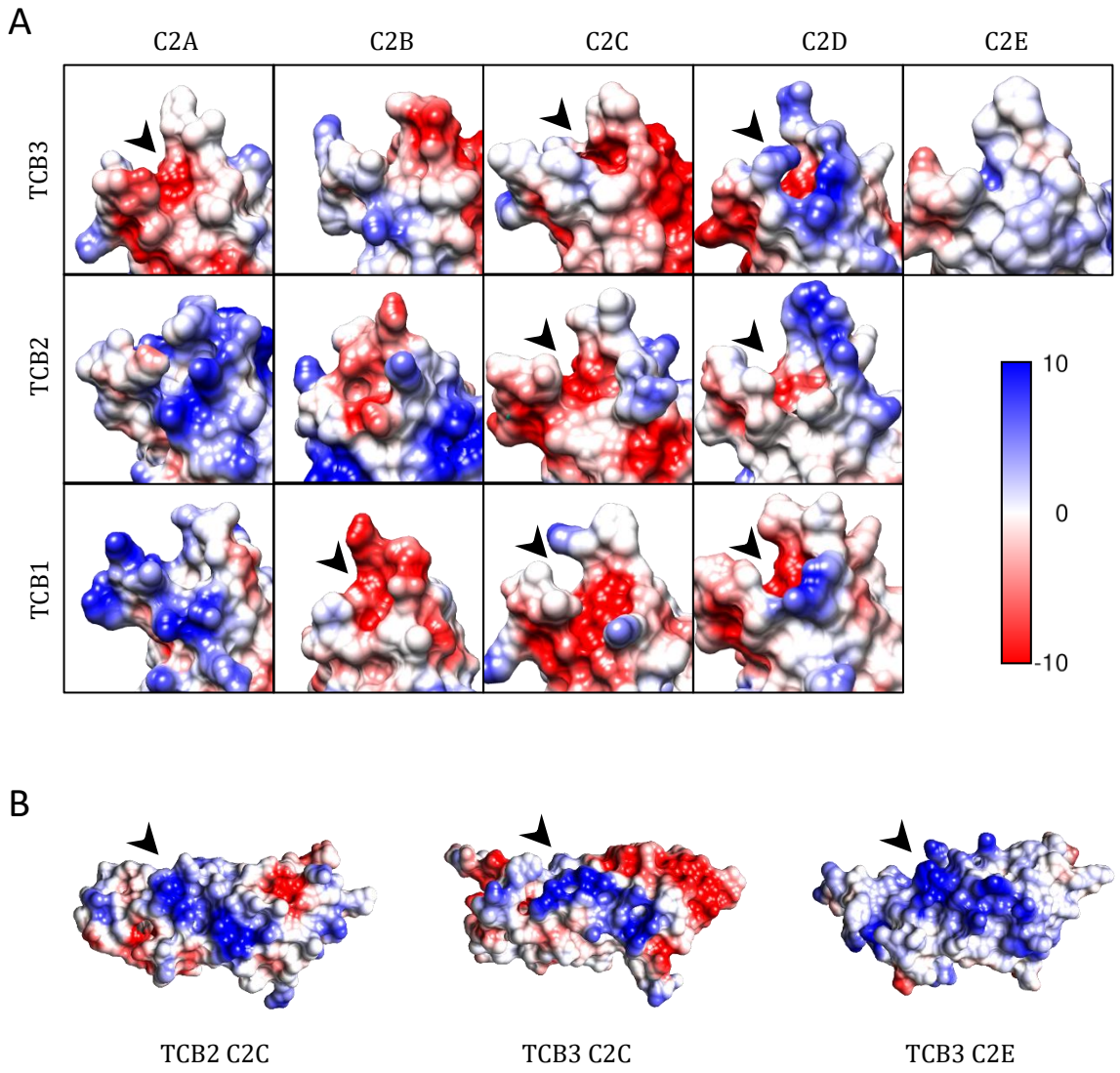

Figure 24. C2 domain homology modelling.

(A) Putative C2 domain calcium-binding pockets. Black arrowheads indicate predicted negatively charged pockets that could bind calcium. Comparative modelling done with Modeller (Webb and Sali 2016), electrostatic potential coloring done with Chimera (Pettersen et al. 2004).

(B) Side views of C2 domains containing a basic surface patch (colored blue, indicated by black arrowheads). Comparative modelling done with Modeller (Webb and Sali 2016), electrostatic potential coloring done with Chimera (Pettersen et al. 2004).

Scale bar: ± 10 kcal/mol·e^{-}.

5.4.1 TCB1/2

The role of the supporting tricalbins in peak formation is likely a facilitating one, in which by dimerizing with Tcb3 they help recruit it from the cytoplasmic ER to the cER, similar to what E-Syts do (Giordano et al. 2013). The hairpin domain could in this case concentrate all tricalbins in highly curved domains of the cER, such as tubules and sheet edges, increasing the chances of tricalbins finding each other.

The C2 domains of Tcb1/2 follow the same structure, a C2A domain connected to the SMP domain by a short aminoacid chain, a C2BC tandem, and a C-terminal C2D tandem. Preliminary homology modelling revealed that both Tcb1/2 C2A domains lack calcium binding pockets (Figure 24A). By contrast, both their C2BC tandems have a calcium-binding pocket in their C2C, and also in the C2B of Tcb1 (Figure 24A). Their C2D domains are also very similar between them, with both presenting a calcium-binding pocket and no basic patch.

Esyt2/3 have a more simplified architecture with one fewer C2 domain, consisting on a SMP proximal C2AB tandem and a C-terminal C2C (Schauder et al. 2014). The isolated C2AB tandem of E-Syt2 binds to lipids bilayers in response to calcium binding to C2A, and does not have a preference for any organelle (Schauder et al. 2014; Xu et al. 2014) By contrast, C2C binds constitutively and preferentially to the PM through a basic surface patch (Giordano et al. 2013; Idevall-Hagren et al. 2015).

If a similarity between the architectures of Tcb1/2 and Esyt1/2 is to be assumed, an indirect comparison between their C2 domains is possible. Tcb1/2 C2D and Esyt2/3 C2C likely share a PM-binding function. Furthermore, the C2A of Tcb1/2 possibly binds a lipid bilayer different from the PM, the cER being the main candidate. The insertion of C2A in the cER membrane may induce curvature. This is known to be the case for similar proteins like mammalian synaptotagmin 1 (SYT1) which creates positive curvature by inserting two closely tethered C2 domains in the lipid membrane (Martens et al. 2007). Interestingly, Tcb1/2 C2BC tandems appear to have no apparent functional relation to the C2BC domains of Esyt2/3. The ability to bind calcium could indicate these domains also bind the PM in a cooperative manner with C2D, and that the tethering functions of the Tcb1/2 C2BCD cluster are found condensed in the Esyt2/3 C2C domains. It is nevertheless possible that Tcb1/2 C2BC binds the cER instead of the PM, and further study is required to discern these tandems' lipid binding affinity.

Regarding the comparison of the C2 domains of Tcb1 against those of Tcb2, their similarities point to a common function. To qualify this interpretation, the presence of a predicted basic patch in Tcb2 C2C and their complete absence in Tcb1, paired with the presence of a strong predicted calcium-binding pocket in Tcb1 C2B may indicate subtle differences in their operation.

5.4.2 TCB3

Tcb3 and E-Syt1 have a different C2 domain distribution compared to their counterparts. Both E-Syt1 and Tcb3 have five C2 domains, but whereas the C2 domains in E-Syt1 are positioned close to each other in a compact distribution, Tcb3 has relatively long unstructured chains flanking the C-terminal C2E.

In E-Syt1, the C2AB domain tandem behaves similarly to its counterparts in E-Syt2/3, where C2A binds to a lipid bilayer in a calcium-dependent manner. It has also been reported that calcium binding to C2A releases the autoinhibitory effect this domain has on PM lipid binding (Bian et al. 2018). In the C2CD tandem, C2C binds the acidic phospholipids at the PM in response to calcium and is in part responsible for the localization of E-Syt1 at the ER-PM contact (Chang et al. 2013; Idevall-Hagren et al. 2015).

In E-Syt1, the C-terminal C2 domain C2E constitutively binds to the PM through a basic patch like the C2C of E-Syt2/3. The calcium-binding properties of E-Syt1 C2C are also responsible for releasing its inhibitory effects on C2E and allowing it to bind the $PI(4,5)P_2$ at the PM . In this manner, the E-Syt1 C2C and C2DE work cooperatively to strongly bind the PM in response to calcium (Bian et al. 2018). It is worth mentioning that in vitro studies indicate E-Syt1 C2AB could also potentially bind the PM with low energy under specific conditions (Ge et al. 2022).

Homology modelling supports the notion that tethering to the PM is done by the Tcb3 C2CDE domains. Tcb3 C2E has an evident predicted basic patch (Figure 24B) that likely mediates a constitutive PM binding through interactions with negatively charged phospholipids. Tcb3 C2C might also bind the PM through its very own basic patch, and this union may be enhanced for both C2C and C2D when bound to calcium. Tcb3 C2B, as is the case for the C2B domains of Tcb1/2, is in close proximity to their respective C2C domains and both likely act as a tandem. The remaining Tcb3 C2A is the most intriguing of them. The presence of a calcium-binding pocket (Figure 24A) likely unrelated to lipid transport suggests another function, and it is appealing to hypothesize this domain is responsible for high curvature peak formation.

5.4.3 Proposed mechanistic model

Taking all this information into account, the following model starts to emerge:

Tcb3 is recruited to the ER-PM through its C2E at normal calcium levels. Its somewhat broad distribution in the ER network when expressed alone supports the idea that dimerization with Tcb1/2 through their SMP domains greatly enhances localization to the cER.

At normal calcium levels the SMP pair of the tricalbin dimer would be capable of lipid transport independently of C2 domains. At the same time, the C2A domains could bind the cER (Figure 25), inducing positive curvature that would result in the shaping of the cER into short sheets and tubules. It is also possible that this morphology is stabilized by the N-terminal hairpin domain and serves to recruit more tricalbins through the preference of these domains for curved bilayers.

Upon damage to the PM, extracellular calcium enters the cell and binds any C2 domains possessing a calcium-binding pocket (Figure 25). The C2C and C2D domains bind the negatively charged phospholipids of the PM, likely restricting the freedom of movement of the SMP dimer and enhancing lipid transport.

The pulling forces would cause the formation of a peak in the cER that could be stabilized by the curvature-inducing C2 domains close to the SMP and the N-terminal hairpins (Figure 25). The SMP domain would then transport a variety of lipids to the PM, while likely bringing byproducts of PM stress back to the ER, such as DAG (Saheki and de Camilli 2017b).

One of the most attractive implications of this model is that tricalbins would act as both sensors of PM integrity, and first responders to membrane damage, with peaks forming wherever the PM has been breached.

In response to membrane stress, cells adjust their lipid composition to adapt to new conditions. These large modifications, as well as most of the lipid transport, are carried out through vesicular transport. However, it is appealing to imagine the cER as the first line of defense against fast damage to the membrane. The highly dynamic cER would constantly scan the PM for damage (Omnus et al. 2016) and directly react to it before more significant changes to the lipidome have been made. Small unicellular organisms lack the buffer systems against membrane that most multicellular organisms enjoy, and would therefore rely heavily on this cER-mediated first line of defense. This is supported by the high amounts of cER in other unicellular organisms (Ng et al. 2018; Suzuki et al. 2018).

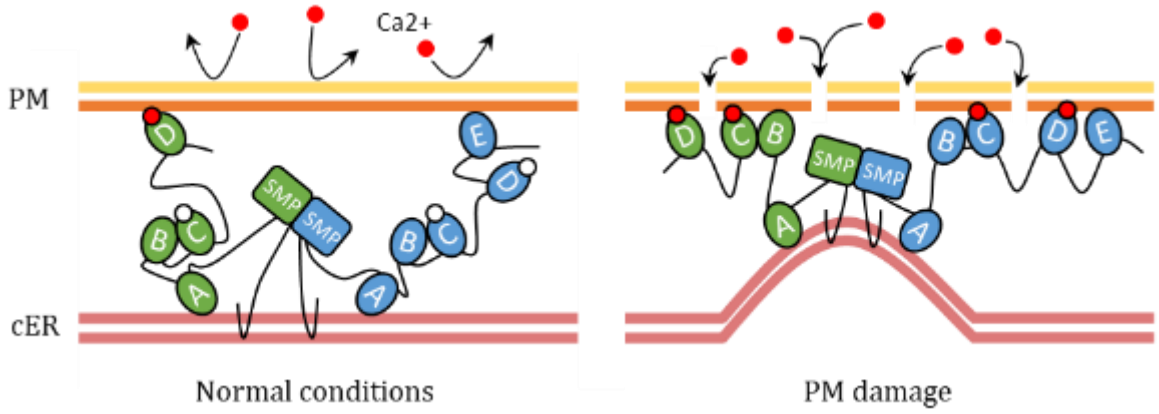

Figure 25. Hypothetical model of tricalbin-induced peak formation.

6 Outlook

With the information available at this point, a model cannot be constructed that explains the necessity of Tcb3 for peak formation. At the same time, the necessity for heterodimerization and the function of Tcb1 and Tcb2 remain a mystery, and direct evidence of a connection between high curvature and lipid transport is still missing.

Elucidating the peak formation mechanism will require the characterization of the properties of each C2 domain. An immediate approach to this problem will involve generating a battery of Tcb3 C2 domain deletion mutants in different combinations and screening them for PM integrity defects. Combined with Cryo-ET, this approach will allow for the identification of C2 domains required for peak formation and lipid transport and how both events are connected. Further down the line, directed mutagenesis of the calcium-binding pocket of important C2 domains will be the first step to finding the role of calcium in these processes.

Experiments on liposomes will also be performed to study tricalbin-mediated lipid transport. Using Cryo-ET on this *in vitro* system could also yield interesting results regarding peak formation if these structures can be recreated on liposomes, and could lead to high resolution structural information and a deeper understanding of tricalbin-mediated curvature induction.

At a later stage, lipidomic studies should be conducted on tricalbins. Finding whether tricalbins preferentially bind some lipid species and identifying these lipids could offer important insights into the PM repair mechanism.

Lastly, studies on tricalbins are ultimately a way to understand the functions of the broader E-Syt family. Complementation experiments to replace Tcb3 with other E-Syts and their truncated variants hold promise to find a possible conserved mechanism.

7 Acknowledgements

I thank Professor Fernández-Busnadiego for his support and direction in this project, as well as Professor Baumeister for his support during my stay at the Max Planck Institute of Biochemistry. I recognize the outstanding contribution of Maria Salfer to the development of the computational methods that made this work possible. Especial appreciation is given to Felix Campelo for his work in mathematical modelling, and Clelia Bourgoint for her contribution to molecular cloning and light microscopy. I want to also emphasize the importance of the work of Ffion Thomas and Professor Stefan regarding flow cytometry and scientific discussion.

I thank Philipp Erdmann, Günter Pfeifer, Jürgen Plitzko, and Miroslava Schaffer for electron microscopy support, and the Imaging Facility of the Max Planck Institute of biochemistry for light microscopy support. I am thankful to Professor Scott Emr for strains used in this study, and Eri Sakata, Vladan Lucic, and Victoria Trinkaus for helpful discussions. I want to express my gratefulness to Patrick C. Hoffmann and Professor Kukulski for their willingness to share unpublished results and their encouragement to carry out my work in a timely manner. I also thank Anna Siegert for providing her translation services.

Especial mention is due to the Graduate School of Quantitative Biosciences Munich, the European Comission (FP7 GA ERC-2012-SyG_318987–ToPAG), and the Deutsche Forschungsgemeinschaft (DFG) (Germany's Excellence Strategy -EXC 2067/1- 390729940 and SFB1190/P22) for their funding.

8 Literature

Aguilar PS, Engel A, Walter P. (2007). The plasma membrane proteins Prm1 and Fig1 ascertain fidelity of membrane fusion during yeast mating. Molecular Biology of the Cell. 18:547–556.

Ahrens J, Geveci B, Law C. (2005). ParaView: An end-user tool for large-data visualization. In: Visualization Handbook.

Al-Amoudi A, Chang JJ, Leforestier A, McDowall A, Salamin LM, Norlén LPO, Richter K, Blanc NS, Studer D, Dubochet J. (2004). Cryo-electron microscopy of vitreous sections. EMBO Journal. 23(18):3583–3588.

Arnold J, Mahamid J, Lucic V, de Marco A, Fernandez JJ, Laugks T, Mayer T, Hyman AA, Baumeister W, Plitzko JM. (2016). Site-Specific Cryo-focused Ion Beam Sample Preparation Guided by 3D Correlative Microscopy. Biophysical Journal. 110(4):860–869.

Baker LA, Rubinstein JL. (2010). Radiation damage in electron cryomicroscopy. In: Methods in Enzymology. Vol. 481.

Balla T. (2013). Phosphoinositides: Tiny lipids with giant impact on cell regulation. Physiol Rev. 93(3):1019–1137.

Benavente JL, Siliqi D, Infantes L, Lagartera L, Mills A, Gago F, Ruiz-López N, Botella MA, Sánchez-Barrena MJ, Albert A. (2021). The structure and flexibility analysis of the Arabidopsis synaptotagmin 1 reveal the basis of its regulation at membrane contact sites. Life Science Alliance. 4(10).

Bepler T, Kelley K, Noble AJ, Berger B. (2020). Topaz-Denoise: general deep denoising models for cryoEM and cryoET Nature Communications 11(5208).

Bian X, Saheki Y, de Camilli P. (2018). Ca 2+ releases E-Syt1 autoinhibition to couple ER -plasma membrane tethering with lipid transport. The EMBO Journal. 37(2):219–234.

Buchholz TO, Krull A, Shahidi R, Pigino G, Jékely G, Jug F. (2019). Content-aware image restoration for electron microscopy. Methods in Cell Biology. 152:277–289.

Burgoyne T, Patel S, Eden ER. (2014). Calcium signaling at ER membrane contact sites. Biochimica et Biophysica Acta - Molecular Cell Research. 1853(9):2012–2017.

Campelo F, Kozlov MM. (2014). Sensing Membrane Stresses by Protein Insertions. PLoS Computational Biology. 10(4).

Carrasco S, Meyer T. (2011). STIM proteins and the endoplasmic reticulum-plasma membrane junctions. Annual Review of Biochemistry. 80:973–1000.

Casares D, Escribá P v., Rosselló CA. (2019). Membrane lipid composition: Effect on membrane and organelle structure, function and compartmentalization and therapeutic avenues. International Journal of Molecular Sciences. 20(9):2167.

Castro IG, Schuldiner M, Zalckvar E. (2018). Mind the Organelle Gap – Peroxisome Contact Sites in Disease. Trends in Biochemical Sciences. 43(3):199-210.

Chang CL, Chen YJ, Liou J. (2017). ER-plasma membrane junctions: Why and how do we study them? Biochimica et Biophysica Acta - Molecular Cell Research. 1864:1494–1506.

Chang CL, Hsieh TS, Yang TT, Rothberg KG, Azizoglu DB, Volk E, Liao JC, Liou J. (2013). Feedback regulation of receptor-induced ca2+ signaling mediated by e-syt1 and nir2 at endoplasmic reticulum-plasma membrane junctions. Cell Reports. 5(3):813–825.

Chung WY, Jha A, Ahuja M, Muallem S. (2017). Cell Calcium Ca 2 + influx at the ER / PM junctions. 63:29–32.

Collado J, Fernández-Busnadiego R. (2017). Deciphering the molecular architecture of membrane contact sites by cryo-electron tomography. Biochimica et Biophysica Acta - Molecular Cell Research. 1864(9): 1507–1512.

Collins SR, Meyer T. (2011). Evolutionary origins of STIM1 and STIM2 within ancient Ca2+ signaling systems. Trends in Cell Biology. 21(4):202-11.

Contreras FX, Ernst AM, Wieland F, Brügger B. (2011). Specificity of intramembrane protein-lipid interactions. Cold Spring Harbor Perspectives in Biology. 3(6).

Creutz CE, Snyder SL, Schulz TA. (2004). Characterization of the yeast tricalbins: Membrane-bound multi-C2-domain proteins that form complexes involved in membrane trafficking. Cellular and Molecular Life Sciences. 61(10):1208–1220.

Crowther RA, Derosier DJ, Klug A. (1970). Reconstruction of a three-dimensional structure from projection and its application to electron microscopy. Proceedings of the Royal Society of London. Series A, Mathematical and Physical Sciences. 317(1530):319-340.

D'Ambrosio JM, Albanese V, Lipp NF, Fleuriot L, Debayle D, Drin G, Copic A. (2020). Osh6 requires Ist2 for localization to ER-PM contacts and efficient phosphatidylserine transport in budding yeast. Journal of Cell Science. 133(11).

Dubochet J, Adrian M, Chang J-J, Homo J-C, Lepault J, McDowall WA, Schultz P. (1988). Cryo-electron microscopy of vitrified specimens. Quarterly Reviews of Biophysics. 21(2):129-228.

Dubochet J, Sartori Blanc N. (2001). The cell in absence of aggregation artifacts. Micron. 32(1). 32(1):91-9.

Egerton RF. (2016). Physical Principles of Electron Microscopy.

Ejsing CS, Sampaio JL, Surendranath V, Duchoslav E, Ekroos K, Klemm RW, Simons K, Shevchenko A. (2009). Global analysis of the yeast lipidome by quantitative shotgun mass spectrometry. Proc Natl Acad Sci U S A. 106(7):2136-41.

Encinar del Dedo J, Idrissi FZ, Fernandez-Golbano IM, Garcia P, Rebollo E, Krzyzanowski MK, Grötsch H, Geli MI. (2017). ORP-Mediated ER Contact with Endocytic Sites Facilitates Actin Polymerization. Developmental Cell. 43(5):588-602.

Entian KD, Schuster T, Hegemann JH, Becher D, Feldmann H, Güldener U, Götz R, Hansen M, Hollenberg CP, Jansen G, et al. (1999). Functional analysis of 150 deletion mutants in Saccharomyces cerevisiae by a systematic approach. Molecular and General Genetics. 62:683-702.

Fernández-Busnadiego R, Saheki Y, De Camilli P. (2015). Three-dimensional architecture of extended synaptotagmin-mediated endoplasmic reticulum-plasma membrane contact sites. Proceedings of the National Academy of Sciences of the United States of America. 112(16):E2004–E2013.

Fernández JJ, Li S. (2003). An improved algorithm for anisotropic nonlinear diffusion for denoising cryo-tomograms. Journal of Structural Biology. 144:52–161

Fernández JJ, Li S, Crowther RA. (2006). CTF determination and correction in electron cryotomography. Ultramicroscopy. 106(7):587-96.

Fischer MA, Temmerman K, Ercan E, Nickel W, Seedorf M. 2009. Binding of plasma membrane lipids recruits the yeast integral membrane protein Ist2 to the cortical ER. Traffic. 10:1084–1097

Frank J. (2006). Electron tomography: Methods for three-dimensional visualization of structures in the cell.

Frank J. (2010). Three-Dimensional Electron Microscopy of Macromolecular Assemblies: Visualization of Biological Molecules in Their Native State.

Frolov VA, Shnyrova A v., Zimmerberg J. (2011). Lipid polymorphisms and membrane shape. Cold Spring Harbor Perspectives in Biology. 3(11).

Gatta AT, Levine TP. (2017). Piecing Together the Patchwork of Contact Sites. Trends in Cell Biology. 27(3):214–229.

Ge J, Bian X, Ma L, Cai Y, Li Y, Yang J, Karatekin E, de Camilli P, Zhang Y. (2022). Stepwise membrane binding of extended synaptotagmins revealed by optical tweezers. Nature Chemical Biology. 18(3):313-320.

Gibson DG, Young L, Chuang RY, Venter JC, Hutchison CA, Smith HO. (2009). Enzymatic assembly of DNA molecules up to several hundred kilobases. Nature Methods. 6:343–345.

Giordano F, Saheki Y, Idevall-Hagren O, Colombo SF, Pirruccello M, Milosevic I, Gracheva EO, Bagriantsev SN, Borgese N, de Camilli P. (2013). PI(4,5)P_2-Dependent and Ca2+-Regulated ER-PM interactions mediated by the extended synaptotagmins. Cell. 153(7):1494–1509.

Hagen WJH, Wan W, Briggs JAG. (2017). Implementation of a cryo-electron tomography tilt-scheme optimized for high resolution subtomogram averaging. Journal of Structural Biology. 197(2):191–198.

Hammond GR, Burke JE. (2020) Novel roles of phosphoinositides in signaling, lipid transport, and disease. Curr Opin Cell Biol. 63:57-67.

Harayama T, Riezman H. (2018). Understanding the diversity of membrane lipid composition. Nature Reviews Molecular Cell Biology. 19(5):281–296.

Hartzell HC, Yu K, Xiao Q, Chien LT, Qu Z. (2009). Anoctamin/TMEM16 family members are Ca2+-activated Cl- channels. Journal of Physiology. 587(10):2127–2139.

Helle SCJ, Kanfer G, Kolar K, Lang A, Michel AH, Kornmann B. (2013). Organization and function of membrane contact sites. Biochimica et Biophysica Acta - Molecular Cell Research. 1833(11):2526–2541.

Hirama T, Lu SM, Kay JG, Maekawa M, Kozlov MM, Grinstein S, Fairn GD. (2017). Membrane curvature induced by proximity of anionic phospholipids can initiate endocytosis. Nature Communications. 8(1):1393.

Hoffmann PC, Bharat TAM, Wozny MR, Boulanger J, Miller EA, Kukulski W. (2019). Tricalbins Contribute to Cellular Lipid Flux and Form Curved ER-PM Contacts that Are Bridged by Rod-Shaped Structures. Developmental Cell. 51(4):488-502.

Hu J, Prinz WA, Rapoport TA. (2011). Weaving the web of ER tubules. Cell. 147(6):1226-1231

Idevall-Hagren O, Lü A, Xie B, de Camilli P. (2015). Triggered Ca 2+ influx is required for extended synaptotagmin 1-induced ER -plasma membrane tethering. The EMBO Journal. 34(17):2291–2305.

Ingólfsson HI, Melo MN, van Eerden FJ, Arnarez C, Lopez CA, Wassenaar TA, Periole X, de Vries AH, Tieleman DP, Marrink SJ. (2014). Lipid organization of the plasma membrane. J Am Chem Soc. 136(41):14554–14559.

Ishikawa K, Tamura K, Fukao Y, Shimada T. (2020). Structural and functional relationships between plasmodesmata and plant endoplasmic reticulum–plasma membrane contact sites consisting of three synaptotagmins. New Phytologist. 226(3):798-808.

Jeyasimman D, Saheki Y. (2020). SMP domain proteins in membrane lipid dynamics. Biochimica et Biophysica Acta - Molecular and Cell Biology of Lipids. 1865(1).

Jumper J, Evans R, Pritzel A, Green T, Figurnov M, Ronneberger O, Tunyasuvunakool K, Bates R, Žídek A, Potapenko A. (2021). Highly accurate protein structure prediction with AlphaFold. Nature. 596:583-589.

Kagiwada S, Hashimoto M. (2007). The yeast VAP homolog Scs2p has a phosphoinositide-binding ability that is correlated with its activity. Biochemical and Biophysical Research Communications. 364: 870–876.

Kagiwada S, Hosaka K, Murata M, Nikawa JI, Takatsuki A. (1998). The Saccharomyces cerevisiae SCS2 gene product, a homolog of a synaptobrevin-associated protein, is an integral membrane protein of the endoplasmic reticulum and is required for inositol metabolism. Journal of Bacteriology. 180(7):1700–1708.

Kagiwada S, Zen R. (2003). Role of the yeast VAP homolog, Scs2p, in INO1 expression and phospholipid metabolism. Journal of Biochemistry. 133(4):515-22.

Kaiser SE, Brickner JH, Reilein AR, Fenn TD, Walter P, Brunger AT. (2005). Structural basis of FFAT motif-mediated ER targeting. Structure. 13(7):1035–1045.

Kelley K, Jaroenlak P, Raczkowski A, Eng E, Bhabha G, Potter C, Carragher B, Noble A. (2021). Waffle Method for optimizing cryo-FIB-milling. Microscopy and Microanalysis. 27(S1).

Kikuma K, Li X, Kim D, Sutter D, Dickman DK. (2017). Extended synaptotagmin localizes to presynaptic ER and promotes neurotransmission and synaptic growth in drosophila. Genetics. 207(3):993-1006.

Kim Y, Chattopadhyay S, Locke S, Pearce DA. (2005). Interaction among Btn1p, Btn2p, and Ist2p reveals potential interplay among the vacuole, amino acid levels, and ion homeostasis in the yeast Saccharomyces cerevisiae. Eukaryotic Cell. 4(2):281-288

Klose C, Surma MA, Gerl MJ, Meyenhofer F, Shevchenko A, Simons K. (2012). Flexibility of a eukaryotic lipidome - insights from yeast lipidomics. PLoS ONE. 7(4).

Klug L, Daum G. (2014). Yeast lipid metabolism at a glance. FEMS Yeast Research. 14(3):369-88.

Koenderink JJ, van Doorn AJ. (1992). Surface shape and curvature scales. Image and Vision Computing. 10(8): 557-564.

Kopec KO, Alva V, Lupas AN. (2010). Homology of SMP domains to the TULIP superfamily of lipid-binding proteins provides a structural basis for lipid exchange between ER and mitochondria. Bioinformatics. 26(16):1927–1931.

Kopec KO, Alva V, Lupas AN. (2011). Bioinformatics of the TULIP domain superfamily. Biochemical Society Transactions. 39(4):1033–1038.

Kralt A, Carretta M, Mari M, Reggiori F, Steen A, Poolman B, Veenhoff LM. (2015). Intrinsically Disordered Linker and Plasma Membrane-Binding Motif Sort Ist2 and Ssy1 to Junctions. Traffic. 16(2):135-47.

Kremer JR, Mastronarde DN, McIntosh JR. (1996). Computer visualization of three-dimensional image data using IMOD. Journal of Structural Biology. 116(1):71-76.

Lahiri S, Toulmay A, Prinz WA. (2015). Membrane contact sites, gateways for lipid homeostasis. Current Opinion in Cell Biology. 33:82–87.

Lanner JT, Georgiou DK, Joshi AD, Hamilton SL. (2010). Ryanodine Receptors: Structure, Expression, Molecular Details, and Function in Calcium Release. Cold Spring Harb Perspect Biol. 2(11).

Lebiedzinska M, Szabadkai G, Jones AWE, Duszynski J, Wieckowski MR. (2009). Interactions between the endoplasmic reticulum, mitochondria, plasma membrane and other subcellular organelles. International Journal of Biochemistry and Cell Biology. 41(10):1805–1816.

Lee I, Hong W. (2006). Diverse membrane-associated proteins contain a novel SMP domain. FASEB Journal. 20(2):202–206.

Levine T, Loewen C. (2006). Inter-organelle membrane contact sites: through a glass, darkly. Current Opinion in Cell Biology. 18(4):371–378.

Lev S. (2010). Non-vesicular lipid transport by lipid-transfer proteins and beyond. Nature Reviews Molecular Cell Biology. 11(10):739–750.

Lev S, Halevy D Ben, Peretti D, Dahan N. (2008). The VAP protein family: from cellular functions to motor neuron disease. Trends in Cell Biology. 18(6):282–290.

Liu Y-T, Zhang H, Wang H, Tao C-L, Bi G-Q, Hong Zhou Z. Isotropic Reconstruction of Electron Tomograms with Deep Learning. BioRxiv.

Li X, Mooney P, Zheng S, Booth CR, Braunfeld MB, Gubbens S, Agard DA, Cheng Y. (2013). Electron counting and beam-induced motion correction enable near-atomic-resolution single-particle cryo-EM. Nature Methods. 10(6):584–590.

Loewen CJR, Levine TP. (2005). A highly conserved binding site in vesicle-associated membrane protein-associated protein (VAP) for the FFAT motif of lipid-binding proteins. Journal of Biological Chemistry. 280(14):14097-14104.

Loewen CJR, Roy A, Levine TP. (2003). A conserved ER targeting motif in three families of lipid binding proteins and in Opi1p binds VAP. EMBO Journal. 22(9):2025–2035.

Loewen CJR, Young BP, Tavassoli S, Levine TP. (2007). Inheritance of cortical ER in yeast is required for normal septin organization. Journal of Cell Biology. 179(3):467–483.

Lučić V, Förster F, Baumeister W. (2005). Structural studies by electron tomography: From cells to molecules. Annual Review of Biochemistry. 74:833-65.

Manford AG, Stefan CJ, Yuan HL, MacGurn JA, Emr SD. (2012). ER-to-Plasma Membrane Tethering Proteins Regulate Cell Signaling and ER Morphology. Developmental Cell. 23(6):1129-40.

Martens S, Kozlov MM, McMahon HT. (2007). How synaptotagmin promotes membrane fusion. Science. 316(5828):1205-1208.

Martens S, McMahon HT. (2008). Mechanisms of membrane fusion: Disparate players and common principles. Nature Reviews Molecular Cell Biology. 9(7):543–556.

Martinez-Sanchez A, Garcia I, Asano S, Lucic V, Fernandez JJ. (2014). Robust membrane detection based on tensor voting for electron tomography. Journal of Structural Biology. 186(1):49-61.

Mastronarde DN. (1997). Dual-axis tomography: An approach with alignment methods that preserve resolution. In: Journal of Structural Biology. 120(3):343-52.

Mastronarde DN. (2005). Automated electron microscope tomography using robust prediction of specimen movements. Journal of Structural Biology. 152(1):36-51.

Mastronarde DN. (2006). Fiducial marker and hybrid alignment methods for single- and double-axis tomography. In: Electron Tomography: Methods for Three-Dimensional Visualization of Structures in the Cell.

McMahon HT, Gallop JL. (2005). Membrane curvature and mechanisms of dynamic cell membrane remodelling. Nature. 438(7068):590-6.

Mesmin B, Bigay J, Moser Von Filseck J, Lacas-Gervais S, Drin G, Antonny B. (2013). A four-step cycle driven by PI(4)P hydrolysis directs sterol/PI(4)P exchange by the ER-Golgi Tether OSBP. Cell. 155(4):830-843.

Miller SBM, Mogk A, Bukau B. (2015). Spatially organized aggregation of misfolded proteins as cellular stress defense strategy. Journal of Molecular Biology. 427(7):1564-1574.

Mindell JA, Grigorieff N. (2003). Accurate determination of local defocus and specimen tilt in electron microscopy. Journal of Structural Biology. 142(3):334-47.

Min SW, Chang WP, Südhof TC. (2007). E-Syts, a family of membranous Ca2+-sensor proteins with multiple C2 domains. Proceedings of the National Academy of Sciences of the United States of America. 104(10):3823–3828.

Nath VR, Mishra S, Basak B, Trivedi D, Raghu P. (2020). Extended synaptotagmin regulates membrane contact site structure and lipid transfer function in vivo. EMBO Rep. 21(9).

Newman TS, Yi H. (2006). A survey of the marching cubes algorithm. Computers and Graphics. 30: 854–879.

Ng AYE, Ng AQE, Zhang D. (2018). ER-PM Contacts Restrict Exocytic Sites for Polarized Morphogenesis. Current Biology. 28(1):146-153.

Nickell S, Förster F, Linaroudis A, del Net W, Beck F, Hegerl R, Baumeister W, Plitzko JM. (2005). TOM software toolbox: Acquisition and analysis for electron tomography. Journal of Structural Biology. 149(3):227-234.

Nishimura AL, Mitne-Neto M, Silva HCA, Richieri-Costa A, Middleton S, Cascio D, Kok F, Oliveira JRM, Gillingwater T, Webb J, et al. (2004). A mutation in the vesicle-trafficking protein VAPB causes late-onset spinal muscular atrophy and amyotrophic lateral sclerosis. American Journal of Human Genetics. 75(5):822–831.

Nziengui H, Schoefs B. (2009). Functions of reticulons in plants: What we can learn from animals and yeasts. Cellular and Molecular Life Sciences. 66(4):584–595.

Oertle T, Klinger M, Stuemer CAO, Schwab ME. (2003). A reticular rhapsody: phylogenic evolution and nomenclature of the RTN/Nogo gene family. The FASEB Journal. 17(10):1238-1247.

Oh U, Jung J. (2016). Cellular functions of TMEM16/anoctamin. Pflugers Archiv European Journal of Physiology. 468(3):443–453.

Omnus DJ, Manford AG, Bader JM, Emr SD, Stefan CJ. (2016). Phosphoinositide kinase signaling controls ER-PM cross-talk. Molecular Biology of the Cell. 27(7):1170-1180.

Orlova E v., Saibil HR. (2011). Structural analysis of macromolecular assemblies by electron microscopy. Chemical Reviews. 111(12):7710-48.

Paillusson S, Stoica R, Gomez-Suaga P, Lau DHW, Mueller S, Miller T, Miller CCJ. (2016). There's Something Wrong with my MAM; the ER-Mitochondria Axis and Neurodegenerative Diseases. Trends in Neurosciences. 39(3):146-157.

Paradies G, Paradies V, Ruggiero FM, Petrosillo G. (2019). Role of Cardiolipin in Mitochondrial Function and Dynamics in Health and Disease: Molecular and Pharmacological Aspects. Cells. 8(7):728.

Pedemonte N, Galietta LJV. (2014). Structure and function of tmem16 proteins (anoctamins). Physiological Reviews. 94(2):419–459.

Pérez-Sancho J, Tilsner J, Samuels AL, Botella MA, Bayer EM, Rosado A. 2016. Stitching Organelles: Organization and Function of Specialized Membrane Contact Sites in Plants. Trends in Cell Biology. 26(9):705-717.

Pérez-Sancho J, Vanneste S, Lee E, McFarlane HE, del Valle AE, Valpuesta V, Friml J, Botella MA, Rosado A. (2015). The arabidopsis synaptotagmin1 is enriched in endoplasmic reticulum-plasma membrane contact sites and confers cellular resistance to mechanical stresses. Plant Physiology. 168(1):132-43.

Petkovic M, Oses-Prieto J, Burlingame A, Jan LY, Jan YN. (2020). TMEM16K is an interorganelle regulator of endosomal sorting. Nature Communications. 11(1):3298.

Pettersen EF, Goddard TD, Huang CC, Couch GS, Greenblatt DM, Meng EC, Ferrin TE. (2004). UCSF Chimera - A visualization system for exploratory research and analysis. Journal of Computational Chemistry. 25(13):1605-12.

Pichler H, Gaigg B, Hrastnik C, Achleitner G, Kohlwein SD, Zellnig G, Perktold A, Daum G. (2001). A subfraction of the yeast endoplasmic reticulum associates with the plasma membrane and has a high capacity to synthesize lipids. European Journal of Biochemistry. 268(8):2351–2361.

Porter KR, Palade GE. (1957). Studies on the endoplasmic reticulum. III. Its form and distribution in striated muscle cells. J Biophys Biochem Cytol. 3(2):269-300.

Prinz WA. (2014). Bridging the gap: Membrane contact sites in signaling, metabolism, and organelle dynamics. Journal of Cell Biology. 205(6):759–769.

Quon E, Sere YY, Chauhan N, Johansen J, Sullivan DP, Dittman JS, Rice WJ, Chan RB, Di Paolo G, Beh CT, et al. (2018). Endoplasmic reticulum-plasma membrane contact sites integrate sterol and phospholipid regulation. PLOS Biology. 16(5).

Radermacher M. (2006). Weighted back-projection methods. In: Electron Tomography: Methods for Three-Dimensional Visualization of Structures in the Cell.

Reimer L, Kohl H. (2008). Transmission Electron Microscopy Physics of Image Formation.

Reinisch KM, De Camilli P. (2016). SMP-domain proteins at membrane contact sites: Structure and function. Biochimica et Biophysica Acta - Molecular and Cell Biology of Lipids. 1861(8):924–927.

Rigort A, Villa E, Bäuerlein FJB, Engel BD, Plitzko JM. (2012). Integrative Approaches for Cellular Cryo-electron Tomography: Correlative Imaging and Focused Ion Beam Micromachining. In: Methods in Cell Biology. Vol. 111.

Rizo J, Sudhof TC. (1998). C2-domains, structure and function of a universal Ca2+-binding domain. Journal of Biological Chemistry. 273(26):15879-15882.

Ruiz-Lopez N, Pérez-Sancho J, del Valle AE, Haslam RP, Vanneste S, Catalá R, Perea-Resa C, van Damme D, García-Hernández S, Albert A. (2021). Synaptotagmins at the endoplasmic reticulum–plasma membrane contact sites maintain diacylglycerol homeostasis during abiotic stress. Plant Cell. 33(7):2431-2453.

Ruskin RS, Yu Z, Grigorieff N. (2013). Quantitative characterization of electron detectors for transmission electron microscopy. Journal of Structural Biology. 184(3):385-93.

Saheki Y, Bian X, Schauder CM, Sawaki Y, Surma MA, Klose C, Pincet F, Reinisch KM, de Camilli P. (2016). Control of plasma membrane lipid homeostasis by the extended synaptotagmins. Nature Cell Biology. 18(5):504-15.

Saheki Y, de Camilli P. (2017a). The Extended-Synaptotagmins. Biochimica et Biophysica Acta - Molecular Cell Research. 1864(9):1490–1493

Saheki Y, de Camilli P. (2017b). Endoplasmic Reticulum–Plasma Membrane Contact Sites. Annual Review of Biochemistry. 86:659-684.

Salfer M, Collado JF, Baumeister W, Fernández-Busnadiego R, Martínez-Sánchez A. (2020). Reliable estimation of membrane curvature for cryo-electron tomography. PLoS Computational Biology. 16(8).

Schaffer M, Mahamid J, Engel BD, Laugks T, Baumeister W, Plitzko JM. (2017). Optimized cryo-focused ion beam sample preparation aimed at in situ structural studies of membrane proteins. Journal of Structural Biology. 197(2):73-82.

Schaffer M, Pfeffer S, Mahamid J, Kleindiek S, Laugks T, Albert S, Engel BD, Rummel A, Smith AJ, Baumeister W, et al. (2019). A cryo-FIB lift-out technique enables molecular-resolution cryo-ET within native Caenorhabditis elegans tissue. Nature Methods. 16(8):757-762.

Schapire AL, Voigt B, Jasik J, Rosado A, Lopez-Cobollo R, Menzel D, Salinas J, Mancuso S, Valpuesta V, Baluska F, et al. (2008). Arabidopsis synaptotagmin 1 is required for the maintenance of plasma membrane integrity and cell viability. Plant Cell. 20(12):3374-3388.

Schauder CM, Wu X, Saheki Y, Narayanaswamy P, Torta F, Wenk MR, de Camilli P, Reinisch KM. (2014). Structure of a lipid-bound extended synaptotagmin indicates a role in lipid transfer. Nature. 510(7506):552-555.

Schulz TA, Choi MG, Raychaudhuri S, Mears JA, Ghirlando R, Hinshaw JE, Prinz WA. (2009). Lipid-regulated sterol transfer between closely apposed membranes by oxysterol-binding protein homologues. Journal of Cell Biology. 187(6):889–903.

Schulz TA, Creutz CE. (2004). The Tricalbin C2 Domains: Lipid-Binding Properties of a Novel, Synaptotagmin-Like Yeast Protein Family. Biochemistry. 43(13):3987–3995.

Schwarz DS, Blower MD. (2016). The endoplasmic reticulum: Structure, function and response to cellular signaling. Cellular and Molecular Life Sciences. 73(1):79-94.

Sclip A, Bacaj T, Giam LR, Südhof TC. (2016). Extended Synaptotagmin (ESyt) triple knock-out mice are viable and fertile without obvious endoplasmic reticulum dysfunction. PLoS ONE. 11(6):1–17.

Shibata Y, Hu J, Kozlov MM, Rapoport TA. (2009). Mechanisms Shaping the Membranes of Cellular Organelles. Annual Review of Cell and Developmental Biology. 25:329-354.

Sievers F, Wilm A, Dineen D, Gibson TJ, Karplus K, Li W, Lopez R, McWilliam H, Remmert M, Söding J, et al. (2011). Fast, scalable generation of high-quality protein multiple sequence alignments using Clustal Omega. Molecular Systems Biology. 11(7):539.

Stachowiak JC, Brodsky FM, Miller EA. (2013). A cost-benefit analysis of the physical mechanisms of membrane curvature. Nature Cell Biology. 15(9):1019-27.

Stefan CJ. (2018). Building ER-PM contacts: keeping calm and ready on alarm. Current Opinion in Cell Biology. 53:1-8

Stefan CJ, Manford AG, Baird D, Yamada-Hanff J, Mao Y, Emr SD. (2011). Osh proteins regulate phosphoinositide metabolism at ER-plasma membrane contact sites. Cell. 144(3):389–401.

Steffen J, Koehler CM. (2018). ER-mitochondria contacts: Actin dynamics at the ER control mitochondrial fission via calcium release. Journal of Cell Biology. 217(1):15-17.

Stepinac E, Landrein N, Skwarzyńska D, Wójcik P, Lesigang J, Lučić I, He CY, Bonhivers M, Robinson DR, Dong G. (2021). Structural studies of the shortest extended synaptotagmin with only two C2 domains from Trypanosoma brucei. iScience. 24(5).

Studer D, Humbel BM, Chiquet M. (2008). Electron microscopy of high pressure frozen samples: Bridging the gap between cellular ultrastructure and atomic resolution. Histochemistry and Cell Biology. 130(5):877-89.

Sutton RB, Davletov BA, Berghuis AM, Sudhof TC, Sprang SR. (1995). Structure of the first C2 domain of synaptotagmin I: A novel Ca2+/phospholipid-binding fold. Cell. 80(6):929-938.

Suzuki J, Fujii T, Imao T, Ishihara K, Kuba H, Nagata S. (2013). Calcium-dependent phospholipid scramblase activity of TMEM 16 protein family members. Journal of Biological Chemistry. 288(19):13305–13316.

Suzuki R, Nishii I, Okada S, Noguchi T. (2018). 3D reconstruction of endoplasmic reticulum in a hydrocarbon-secreting green alga, Botryococcus braunii (Race B). Planta. 247(3):663-677.

Tatsuta T, Scharwey M, Langer T. (2014). Mitochondrial lipid trafficking. Trends in Cell Biology. 24(1):44-52.

Tavassoli S, Chao JT, Young BP, Cox RC, Prinz WA, De Kroon AIPM, Loewen CJR. (2013). Plasma membrane - Endoplasmic reticulum contact sites regulate phosphatidylcholine synthesis. EMBO Reports. 14(5):434-440.

Tegunov D, Cramer P. (2020). Real-time cryo-EM data pre-processing with Warp Europe PMC Funders Group. Nature Methods. 16(11):1146-1152.

Thompson RF, Walker M, Siebert CA, Muench SP, Ranson NA. (2016). An introduction to sample preparation and imaging by cryo-electron microscopy for structural biology. Methods. 100:3-15.

Tong J, Yang Huiseon, Yang Hongyuan, Eom SH, Im YJ. (2013). Structure of Osh3 reveals a conserved mode of phosphoinositide binding in oxysterol-binding proteins. Structure. 21(7):1203-1213.

Toulmay A, Prinz WA. (2011). Lipid transfer and signaling at organelle contact sites: The tip of the iceberg. Current Opinion in Cell Biology. 23(4):458–463.

Toulmay A, Prinz WA. (2012). A conserved membrane-binding domain targets protein to organelle contact sites. Journal of Cell Science. 125(1):49–58.

Tsuji T, Cheng J, Tatematsu T, Ebata A, Kamikawa H, Fujita A, Gyobu S, Segawa K, Arai H, Taguchi T, et al. (2019). Predominant localization of phosphatidylserine at the cytoplasmic leaflet of the ER, and its TMEM16K-dependent redistribution. Proc Natl Acad Sci U S A. 116(27):13368-13373.

Voeltz GK, Prinz WA, Shibata Y, Rist JM, Rapoport TA. (2006). A class of membrane proteins shaping the tubular endoplasmic reticulum. Cell. 124(3):573–586.

Watson ML. (1958). Staining of tissue sections for electron microscopy with heavy metals. Journal of Cell Biology. 4(4):475-8.

Webb B, Sali A. (2016). Comparative protein structure modeling using MODELLER. Current Protocols in Bioinformatics. 20(54).

Weber-Boyvat M, Kentala H, Peränen J, Olkkonen VM. (2015). Ligand-dependent localization and function of ORP-VAP complexes at membrane contact sites. Cellular and Molecular Life Sciences. 72(10):1967–1987.

Wietrzynski W, Schaffer M, Tegunov D, Albert S, Kanazawa A, Plitzko JM, Baumeister W, Engel BD. (2020). Charting the native architecture of chlamydomonas thylakoid membranes with single-molecule precision. Elife. 16(9).

Williams DB, Carter CB. (2009). Transmission electron microscopy: A textbook for materials science.

Wolf W, Kilic A, Schrul B, Lorenz H, Schwappach B, Seedorf M. (2012). Yeast Ist2 recruits the endoplasmic reticulum to the plasma membrane and creates a ribosome-free membrane microcompartment. PLoS ONE. 7(7).

Wong AKO, Young BP, Loewen CJR. (2021). Ist2 recruits the lipid transporters Osh6/7 to ER–PM contacts to maintain phospholipid metabolism. Journal of Cell Biology. 220(9).

Xu J, Bacaj T, Zhou A, Tomchick DR, Südhof TC, Rizo J. (2014). Structure and Ca2+-binding properties of the tandem C 2 Domains of E-Syt2. Structure. 22(2):269–280.

Yan R, Edwards TJ, Pankratz LM, Kuhn RJ, Lanman JK, Liu J, Jiang W. (2015). Simultaneous determination of sample thickness, tilt, and electron mean free path using tomographic tilt images based on Beer-Lambert law. Journal of Structural Biology. 192(2):287-96.

Zheng SQ, Palovcak E, Armache JP, Verba KA, Cheng Y, Agard DA. (2017). MotionCor2: Anisotropic correction of beam-induced motion for improved cryo-electron microscopy. Nature Methods. 14(4):331-332.